Computational model of intraluminal thrombus growth in abdominal aortic aneurysms with fibrin generation

A dissertation as part of the requirements for completion of a Masters in Mechanical Engineering (M.Sc Eng) at the University of Cape Town by Mark Robin Taylor.
Student number: TYLMAR015

Supervisor: Dr Malebogo Ngoepe

Contact email: Markrobintaylor@gmail.com

Abstract

Abdominal aortic aneurysms affect 0.2% of the population and are closely associated with intraluminal thromboses (ILTs) that develop in the sac. Advanced imaging and treatment techniques are available, however there is room for improvement in the methods used to predict the outcome or necessity of surgical intervention. For a computational model to be useful in this clinical setting, it would need to incorporate relevant patient-specific data and prioritise simplicity and speed over exhaustive detail. This paper presents the details of such a model, for abdominal aortic aneurysms, particularly in the simplification of the coagulation biochemistry. Explicit modelling of the coagulation cascade is replaced with a patient-specific thrombin generation curve. This curve is defined by three values obtained from a blood test. Another key feature is the thrombosis growth model, which incorporates conversion of fibrinogen to fibrin, variation between clot core and shell, and mechanical lysis. The model generates ILTs with morphologies visually similar to those typically found in the body, however more work is required to refine and validate the model.

Table of Contents

Abstract ... i
Acknowledgements ... iv
Plagiarism declaration ... iv
Table of Figures ... iv
1 Literature review ... 1
  1.1 Clinical context ... 1
    1.1.1 What is an Aneurysm? ... 1
    1.1.2 Risk Factors ... 1
    1.1.3 Diagnosis and Risk Metrics ... 2
    1.1.4 Treatment Options and Success Rates ... 3
  1.2 Biological Context ... 5
    1.2.1 Blood Vessels ... 5
    1.2.2 What is Blood? ... 8
  1.3 Theories of Thrombogenesis ... 9
  1.4 Platelet Activation and Adhesion ... 9
  1.5 The Coagulation Cascade ... 11
    1.5.1 Initiation ... 12
    1.5.2 Amplification and Propagation ... 12
    1.5.3 Decay ... 13
  1.6 Fibrin Generation, Morphology and Properties ... 14
  1.7 Thrombus Growth and Cessation ... 18
  1.8 Thrombus Composition ... 20
  1.9 Computational Models ... 21
    1.9.1 Modelling of Blood ... 21
    1.9.2 Modelling of Coagulation Reactions ... 22
    1.9.3 The Calibrated Automated Thrombogram ... 24
    1.9.4 Modelling of Thrombus ... 25
    1.9.5 Vessel Size and Environment ... 29
    1.9.6 Boundary Conditions ... 31
2 Methodology ... 34
  2.1 Mathematical Model ... 34
  2.2 Fluid Boundary Conditions ... 35
  2.3 Chemical Boundary Conditions ... 39
    2.3.1 Fibrinogen ... 39

2.3.2 Fibrin 40
2.3.3 Thrombin 40
2.4 Software 44
2.5 Meshing 44
2.6 Solver Parameters 46
2.7 Grid Independence Study 47
2.8 CFL Condition and Time Step Size 51
2.9 Model for Thrombosis 55
2.10 Summary of Computational Strategy 58
2.11 Summary of Fluid Values 59
3 Results 61
3.1 Strategy A 61
3.2 Strategy B 65
3.2.1 Point 1: Flow time = 20.8 seconds 67
3.2.2 Point 2: Flow time = 20.9 seconds 68
3.2.3 Point 3: Flow time = 21.25 seconds 71
3.3 Vortical Structures and Thrombin Distribution 72
3.3.1 Point 4: Flow time = 25.5 s 73
3.3.2 Point 5: Flow time = 25.64 s 75
3.3.3 Point 6: Flow time = 26.11s 77
3.3.4 Point 7: Flow time = 30.0 seconds 79
4 Discussion 81
5 References 83
6 Appendix 91

Acknowledgements

To my supervisor, Malebogo, thank you for making this all possible by taking me on as your student. I thoroughly enjoyed our discussions about the work and about everything else, especially on the trip to Johannesburg. To Andrew Gill and Charles Crosby at the CHPC, thank you for your willingness to help and enthusiasm in sharing your knowledge. To Chris, Liam, Qudus and Raymond, thank you for the collaboration and camaraderie in the lab. To my family and friends, thanks for the support and stabilising influence.

Plagiarism declaration

I know the meaning of plagiarism and declare that all the work in the document, save for that which is properly acknowledged, is my own. This thesis/dissertation has been submitted to the Turnitin module (or equivalent similarity and originality checking software) and I confirm that my supervisor has seen my report and any concerns revealed by such have been resolved with my supervisor.

Signed by: Mark Taylor   Date: 9 February 2020

Signed by candidate

Table of Figures

Figure 1- Restructured geometry of an AAA (white) containing an ILT (red and green) reconstructed from CT scan imagery [6]........ 1
Figure 2 - Treatment decision tree for AAA prior to rupture [8] 3
Figure 3- Diagram of open surgical repair of AAA[20] 4
Figure 4- Diagram of endovascular repair for AAA[20] 5
Figure 5- Structure of the aorta wall [23] 6
Figure 6 - Axial CT scan of 8cm AAA with lumen indicated [28] 7
Figure 7 - Schematic of the coagulation cascade [55] 11
Figure 8 - Propagation of thrombin in blood plasma based on TF stimulation [32]........ 13
Figure 9- Effect of shear rate on fibrin morphology. Dark dots represent pores in membrane [41]........ 15
Figure 10 - Effect of thrombin flux on fibrin morphology. Dark dots represent pores in membrane [41]........ 15
Figure 11 - Effect of thrombin concentration on fibrin morphology [65]........ 16
Figure 12 - Fibrin deposition and thrombin generation as a function of shear rate and tissue factor (TF) concentration [50]........ 16
Figure 13 - Effect of shear rate on fibrin diameter, orientation and height [50]........ 17
Figure 14 - Plots of haemodynamic variables and ILT growth rate for patients with significant thrombus deposition [69]........ 19
Figure 15 - Diagram of Michaelis-Menten reaction kinetics [79] 23

Figure 16 - Diagram of typical core and shell morphology in ILTs (left). Confocal fluorescent microscopy image of markers for core (blue) and shell (red) [89] 26
Figure 17 - Permeability of thrombus based on platelet and fibrin volume fraction [90] 28
Figure 18 - Mechanical properties of thromboses grown in various blood and plasma types [92].. 29
Figure 19 - Initiation and movement of vortical structures during one heartbeat pulse......... 31
Figure 20 - Effect of vorticity (Lambda 2) on distribution of thrombin (IIa)............................ 31
Figure 21 - Aortic flow waveform based on [94] used by [76] 32
Figure 22 –Velocity profiles for sinusoidal waveform with varying Womersley number [99]. 33
Figure 23 - Flow profiles at peak systole (2.9 sec) 35
Figure 24 - Flow profiles at late systole (3.13 sec) 36
Figure 25 - Flow profiles at early diastole (3.34 sec) 36
Figure 26 - Flow rate in the aorta during one heartbeat [102]... 37
Figure 27 - Inlet flow waveforms based on experimental work and optimised functions 39
Figure 28 - Thrombin concentration curve based on equation 2.11 and parameters from Bloemen 2018.. 42
Figure 29 - Detailed view of mesh at aneurysm wall 45
Figure 30 - Response of key haemodynamic variables to mesh refinement........................ 48
Figure 31 - Overall view of mesh with 64 000 cells.. 48
Figure 32 - Close up view of mesh at aneurysm neck 49
Figure 33 - Histogram of cell orthogonality in final mesh 49
Figure 34 - Histogram of cell aspect ratio in final mesh 50
Figure 35 - Histogram of cell skewness in final mesh 50
Figure 36 - Histogram of overall cell quality in final mesh... 51
Figure 35 - Variable time step size during heartbeat and indication of representative points 1,2 & 3 54
Figure 38 - Courant numbers at point 1: Peak systole.. 54
Figure 39 - Courant numbers at point 2: Early diastole.. 55
Figure 40 - Courant numbers at point 3: late diastole 55
Figure 39 - Failed attempt to implement variable porosity in growing thrombus simulation.. 57
Figure 40 - Modelling strategy for conversion from fluid blood to multi-zone thrombus........ 58
Figure 41 – ILT with velocity vectors for over-diffusive, high thrombin concentration environment using strategy A... 61
Figure 42 - Thrombin distribution for over-diffusive, high thrombin concentration environment using strategy A 62
Figure 43 - Fibrin distribution for over-diffusive, high thrombin concentration environment using strategy A... 62
Figure 44 - ILT growth for strategy A.. 63
Figure 47 - Final ILT and velocity vectors for strategy A with TG curve boundary condition 63
Figure 46 - Growth rate and flow velocity for strategy A with TG boundary 64
Figure 47 - ILT size and TG curve for strategy B.. 65
Figure 48 - ILT growth rate for strategy B... 66
Figure 49 - Growth rate and velocity for strategy B between 20.7 and 22 seconds 67
Figure 50 - ILT region and velocity vectors for strategy B at 20.8 sec 67
Figure 51 - Shear stress at ILT boundary in ‘Detail 0’ area at 20.8 seconds........................ 68
Figure 52 - ILT region and velocity vectors for strategy B at 20.9 sec 68
Figure 55 - Shear stress at ILT boundary in ‘Detail 1’ area at 20.9 seconds........................ 69
Figure 56 - Shear stress at ILT boundary in ‘Detail 2’ area at 20.9 seconds........................ 69
Figure 55 - Fibrin concentration and velocity vectors in 'Detail 2' region at 20.9 seconds.... 70

Figure 58 - Moving boundary of ILT in 'Detail2' region.. 70
Figure 59 - Fibrin concentration and velocity vectors in 'Detail 2' region at 21.25 seconds.. 71
Figure 60 - ILT region and velocity vectors at 21.25 seconds. Region of rapid proximal growth indicated. 72
Figure 59 - Growth rate and velocity for strategy B between 25.2 and 26.7 seconds 72
Figure 62 - ILT region and velocity vectors for strategy B at 25.5 sec 73
Figure 63 - Vorticity magnitude for strategy B at 25.5 sec 73
Figure 64 – High shear stress caused by vortex ‘x’ leading to localised lysis 74
Figure 65 - Contours of thrombin concentration at 25.5 seconds 74
Figure 64 - Contours of fibrin concentration at 25.5 seconds.. 75
Figure 67 - ILT region and velocity vectors for strategy B at 25.64 seconds........................ 75
Figure 68 - Vorticity magnitude for strategy B at 25.64 seconds.. 76
Figure 69 - Contours of thrombin concentration at 25.64 seconds 76
Figure 70 - Contours of fibrin concentration at 25.64 seconds.. 77
Figure 71 - ILT region and velocity vectors for strategy B at 26.11 seconds........................ 77
Figure 72 - Vorticity magnitude for strategy B at 26.11 seconds.. 78
Figure 73 - Contours of thrombin concentration at 26.11 seconds 78
Figure 74 - Contours of fibrin concentration at 26.11 seconds.. 79
Figure 73 - ILT region and velocity vectors for strategy B at 30 seconds............................ 80
Figure 76 - Shear stress at ILT boundary causing widespread lysis at 30 seconds............. 80

1 Literature review

1.1 Clinical context

1.1.1 What is an Aneurysm?

An aneurysm is a localised and permanent dilation of a blood vessel. An abdominal aortic aneurysm (AAA) is a particularly prevalent type of aneurysm located in the descending aorta between the diaphragm and the kidneys. The criterion for classification as an AAA is a diameter over 150% of the normal vessel size, or an absolute diameter greater than 3cm [1], [2]. Most AAAs are spindle shaped, however, some can form asymmetric bulges on one side of the vessel – these are called fusiform and saccular aneurysms respectively [3]. Over 75% of aneurysms will also contain layers of clotted blood attached to the vascular endothelium known as intra-Luminal thromboses (ILTs) [4]. When one speaks of an aneurysm, the combination of the thrombosis and dilated blood vessel is implied, as the two components affect one another and can both lead to various pathologies [5]. Figure 1 shows the aneurysm vessel wall in grey and the thrombus in red and green.

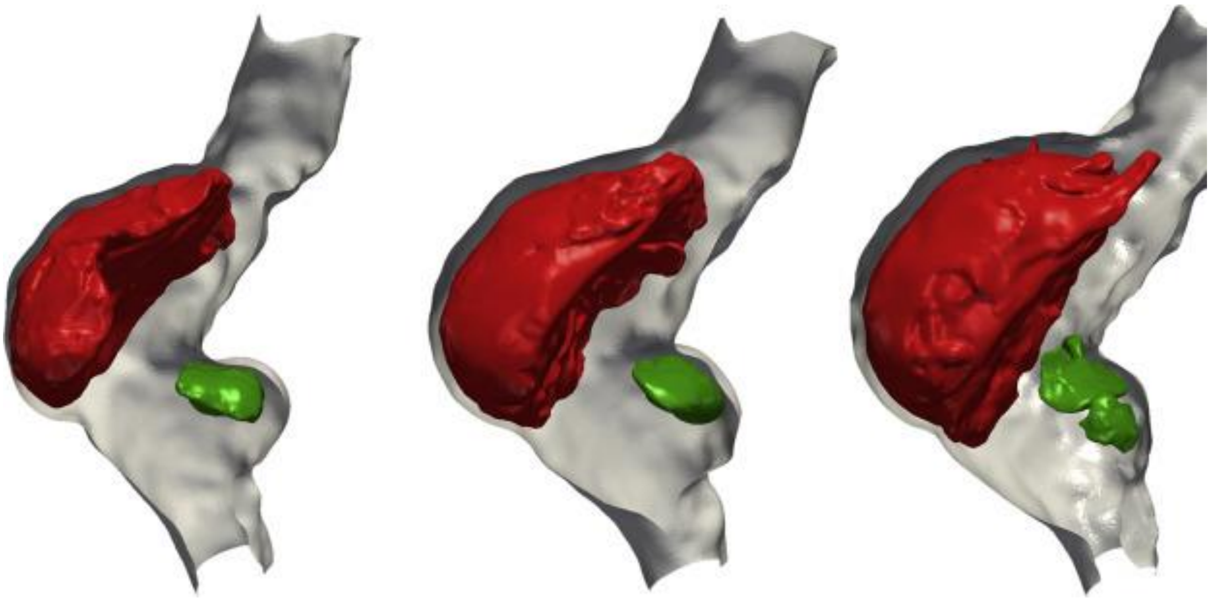

Figure 1- Restructured geometry of an AAA (white) containing an ILT (red and green) reconstructed from CT scan imagery [6]

1.1.2 Risk Factors

In Southern Africa the prevalence of AAAs was estimated to be 0.2% of the total population in 2010, a slight increase from the years earlier at 0.19%. Australasia showed the highest prevalence at 0.31% [1]. These fairly low prevalence numbers hide the fact that thrombosis and aneurysm related pathologies are one of the leading causes of immediate death globally, disproportionately affecting the elderly and male population [2]. To illustrate the magnitude of this variation, the global prevalence of aneurysms in individuals above the age of 80 is 3% [1], and 5 times more prevalent in males than females [7]. Nevertheless, the risk of rupture can be four times higher for women than for men [8], so mortality rates are roughly equal for both genders. Quantity and duration of cigarette smoking showed significant correlation with risk of AAA, whereas regular consumption of fruits, vegetables, nuts and fish was correlated with slightly lower risk. Family history of aneurysms was also identified as a significant predictor of risk, as was high blood pressure and obesity to a lesser extent [7]. Atherosclerosis has been thought to lead to thrombosis and aneurysms, however, this idea has recently been challenged by observations that AAA can develop in blood vessels free of plaque [3].

1.1.3 Diagnosis and Risk Metrics

Most aneurysms will gradually grow while causing no noticeable symptoms or effects until such time as they suddenly rupture [2]. If rupture occurs away from a hospital, the mortality rate is up to 90% [1], and just less than 50% if it occurs in a hospital [7]. Early diagnosis and treatment are vital to curb mortality and morbidity rates associated with unexpected rupture. Fortunately AAAs can be identified non-invasively with high accuracy and fairly low cost by means of ultrasound imaging [7]. Size is often used as a rule of thumb by clinicians, with 5 or 5.5 cm diameter typically the threshold above which surgical intervention is deemed absolutely necessary [9]. This approach is unreliable though, as small aneurysms have been known to rupture and large ones to remain asymptomatic for years [5], [9]. This has led clinicians to seek better metrics to inform the decision to intervene or not.

Aneurysm growth rate is one such metric, as there is empirical evidence that a faster growth rate correlates with a higher risk of rupture [10]. However, identifying growth rate is only possible in cases where a patient can be closely monitored, which typically involves an ultrasound or CT scan every 3 to 6 months [11]. This is not possible if the aneurysm is already at high risk of rupture when it is identified, nor is it feasible if the patient lacks access to qualified diagnosticians for practical or financial reasons [9]. Nevertheless, if it is possible, it has been shown that regular monitoring of stable AAAs smaller than 5.5cm diameter is safe and preferable to premature surgery [8].

A promising biochemical indicator for risk of rupture is the level of serum MMP-9 in the blood [8]. This substance is involved in the degradation of the aortic wall, so some studies suggest that elevated levels not only indicate the presence of an AAA, but the quantity of MMP-9 can be correlated with the size and expansion rate of these aneurysms [12], [13]. Subsequent studies have found no correlation between AAAs and MMP-9 and have called into question their diagnostic use [14].

A more accurate and certain method for risk analysis would clearly be beneficial. To this end, many studies have sought to tackle the problem explicitly by simulating the relevant physiological features by means of computational modelling. The fundamental assumption is that rupture occurs when the tensile stresses in the vessel wall exceed the strength of the tissue. This approach is not as simple as it sounds though, as wall strength can vary significantly between patients and within the aneurysm itself [3], [15]. The wall stress is also subject to spatio-temporal variation due to blood pressure, flow structures and the shielding effect of the thrombus on the wall [4], [5], [16]. Nevertheless, where simulations have attempted to quantify wall stress, a strong correlation has been found between risk of rupture and peak wall stress [11], [17].

Despite the potential accuracy of wall stress simulations for prediction of rupture risk, the complexity and computational requirements of this method makes it impractical as a diagnostic tool at present. The majority of clinicians continue to use maximal diameter, growth rate, and various other empirical or related diagnostic markers to build up a composite risk profile [8]. The decision tree currently in use by clinicians can be represented as follows:

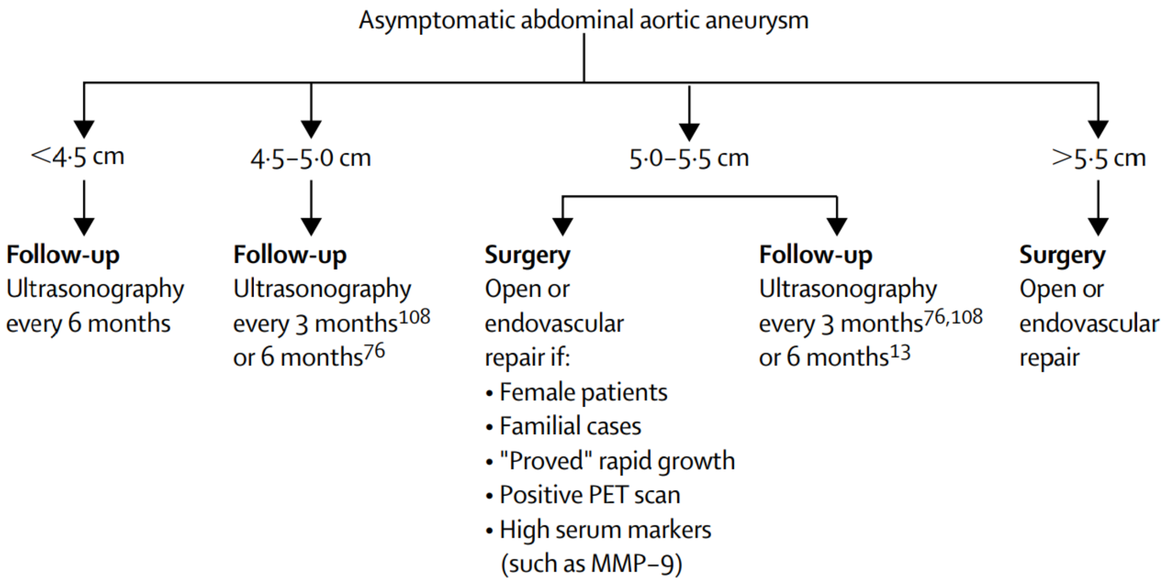

Figure 2 - Treatment decision tree for AAA prior to rupture [8]

1.1.4 Treatment Options and Success Rates

The only effective means of preventing aneurysm rupture at present is invasive surgery [2]. Given that patients are usually of advanced age and potentially in poor health, this surgery does carry some risks. Post-operative complications can include renal failure, paralysis and cardiac or pulmonary ischemia [18]. Non-invasive treatments such as statins or doxycycline have shown potential for preventing aneurysm growth but these are still in research phase [8]. Surgical procedures fall into two categories: open surgery or endovascular repair (EVAR).

Open surgery requires the patient to be under general anaesthetic, and usually involves a midline laparotomy and cross-clamping of the aorta [19]. As illustrated in Figure 3, A synthetic textile vascular graft is placed within the diseased section of the aorta and sutured in place. The vessel is then closed around the graft with the intention that the graft will relieve pressure on the vessel wall [8].

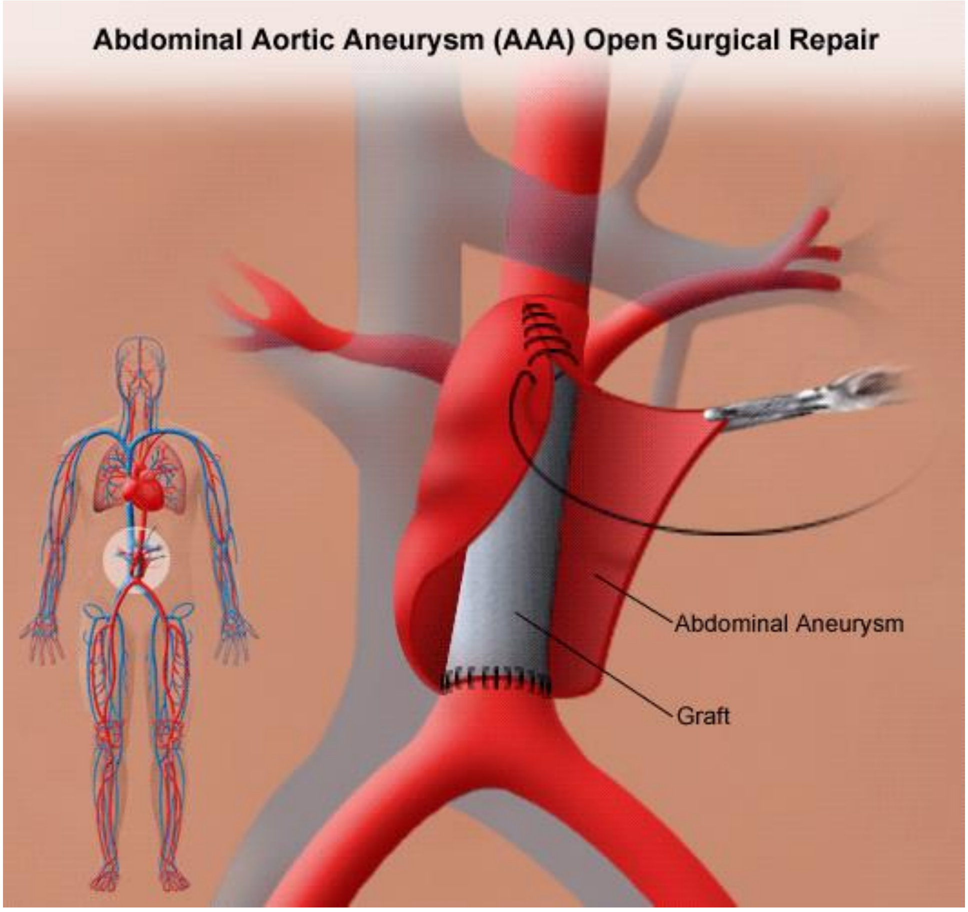

Figure 3- Diagram of open surgical repair of AAA[20]

EVAR is significantly less invasive and better tolerated than open surgery so it has been gaining popularity since it was introduced in the early 1990s [18]. Small incisions are made in the groin and an endograft or stent along with its placement mechanism is pushed upstream through the arteries until it reaches the correct position in the aorta. The graft or stent is expanded to fix it in place and the introducer mechanism is removed. Only 40% - 80% of AAAs are amenable to EVAR, with difficulty usually arising from insufficient attachment region proximal to the aneurysm sac [8], [18]. The appearance of the stent is illustrated in Figure 4.

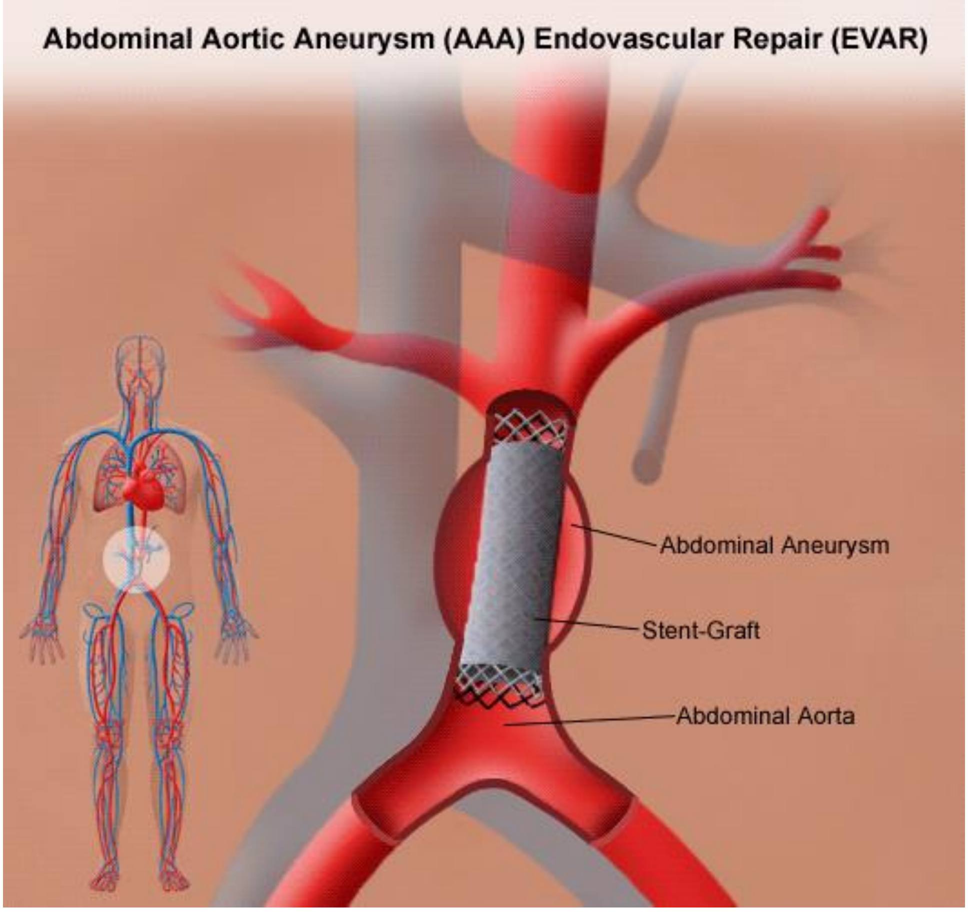

Figure 4- Diagram of endovascular repair for AAA[20]

Various studies have been conducted on the comparative effectiveness and risks of open surgery vs EVAR. EVAR typically has significantly lower 30-day mortality rates than open surgery. Two large European studies have found 1.7% [19] and 1.8% [8] mortality for EVAR compared to 4.7% [19] and 2.7% [8] for open surgery. However, long term success of EVAR is worse than open surgery, with at least 25% of patients requiring subsequent interventions or open surgery to rectify complications [19]. Various European studies have shown that the failure rate for endovascular repair is 3% per year (1% by rupture and 2% by a required conversion to open repair) versus a failure rate of 0.3% for open repair. Two years after endovascular repair, 6.1% of patients with large AAAs died from aneurysm-related causes and 8.2% needed conversion to open repair [8].

While these percentages are revealing about the performance of surgical interventions, they are based on European figures. In the South African context, high rates of HIV and Tuberculosis can lead to a higher proportion of ‘high risk’ cases. In a recent study at Groote Schuur hospital in Cape Town the 30-day mortality rate after all elective AAA repair was 5.1% [18].

1.2 Biological Context

1.2.1 Blood Vessels

Blood vessels are complex structures which must respond and adapt constantly in order to facilitate the healthy distribution of blood in the body. Blood vessels will dilate or constrict quickly in response to changes in temperature or injury, and on a longer timescale they can become thicker or thinner in response to stresses caused by blood pressure [21]. The large arteries have an additional function of assisting the work of the heart by expanding elastically during systole - thus reducing the peak pressure seen by downstream vasculature and organs - then recoiling during diastole to maintain arterial pressure while the heart is refilling [22].

The blood vessels are able to perform these functions because of the structure of the vessel wall. Arteries are typically more thick, muscular and elastic than veins and do not contain valves. The vessel wall of a large artery is made up of three layers as shown in Figure 5, the tunica intima or interna, tunica media and tunica adventitia or externa. The intimal layer is made up of a single layer of endothelial cells surrounded by a thin membrane of elastic connective tissue. The medial layer contains smooth muscle cells and bundles of elastin and collagen fibres. The external layer consists of another elastic membrane and a network of nerves and blood vessels which serve and supply the medial layer [3].

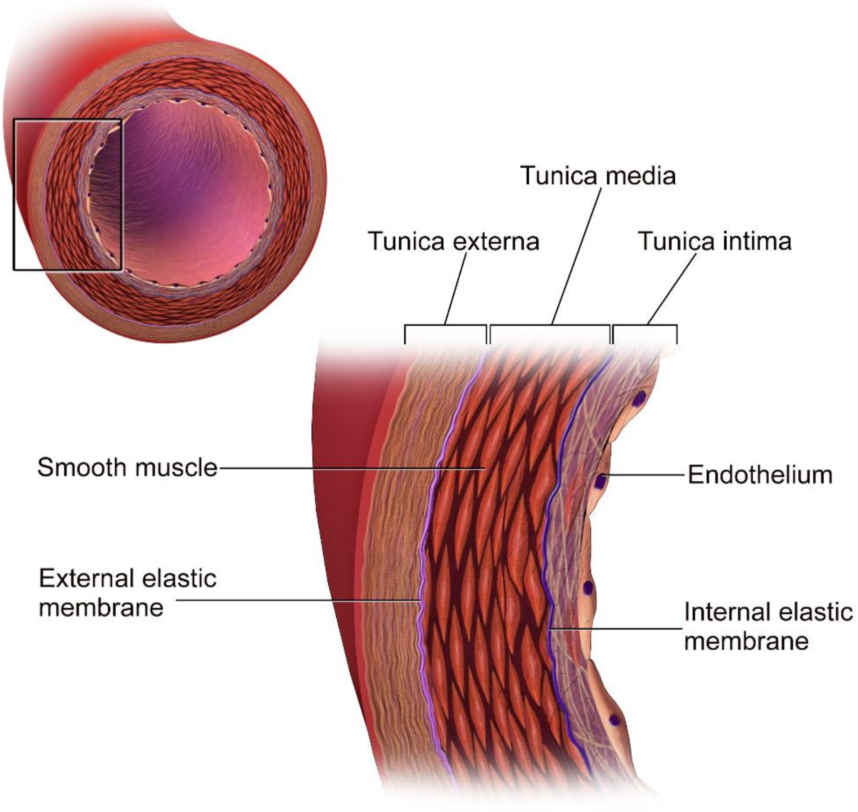

Figure 5- Structure of the aorta wall [23]

If the artery wall stiffens or loses its elasticity, either as a result of atherosclerotic plaque or a degradation of the elastic fibres, the pressure pulses from the heart will propagate faster and have higher peak values [3], [21]. Studies have shown that the medial layers of aortic aneurysms contain less collagen and elastin than the neighbouring healthy aorta, resulting in a decrease in extensibility [9], [24]. It is not clear whether this degradation is the cause or effect of the aneurysm distention.

The Aorta exits the left ventricle of the heart vertically and is known as the ascending aorta until it turns downward at the aortic arch. The descending aorta travels down through the torso until it splits near the pelvis to become the left and right iliac arteries. Within the descending aorta the length above the diaphragm is known as the thoracic aorta, and the section between the diaphragm and the split to iliac arteries is called the abdominal aorta (AA). The AA is one of the most common sites for aneurysms, the reason for this is still the subject of research. Wills et al. [25] suggested that the AA below the renal arteries (known as the infrarenal aorta) is especially prone to aneurysms because the vessel tapers and becomes less elastic. This change in the structure of the aorta is thought to create higher pressure peaks which then damage the vessel wall. Taylor & Draney [21] suggested that the multiple bends, bulges and branches of the AA create complex and recirculating flow as well as reflected pressure waves which travel up towards the heart and interfere with those travelling downwards.

In many AAAs, the flowing blood is not in direct contact with the aorta wall due to the presence of intra-luminal thromboses (ILTs). Typically, these ILTs will form in the bulge created by the aneurysm, gradually filling all the additional space but not encroaching far into the mainstream of blood flow. It is common to observe an ILT surrounding an area of free-flowing blood which is a similar diameter and shape to the original blood vessel. This region of free flow is called the lumen [2], [4] and can be seen as a white circle surrounded by grey thrombus in Figure 6. The effect of ILT on AAA growth, wall stress and rupture is not well understood, however the ILT is thought to have a significant biochemical and haemodynamic effect on the relationship between the blood and the vessel wall. It has been shown that ILT destroys endothelial and medial cells by means of hypoxia, leading to further degradation of the vessel wall and blocked transfer of vasoconstrictors and vasodilators [3], [5], [26]. ILT could also alter the stress distribution on the vessel wall, potentially shielding it from peak direct and shear stresses [27].

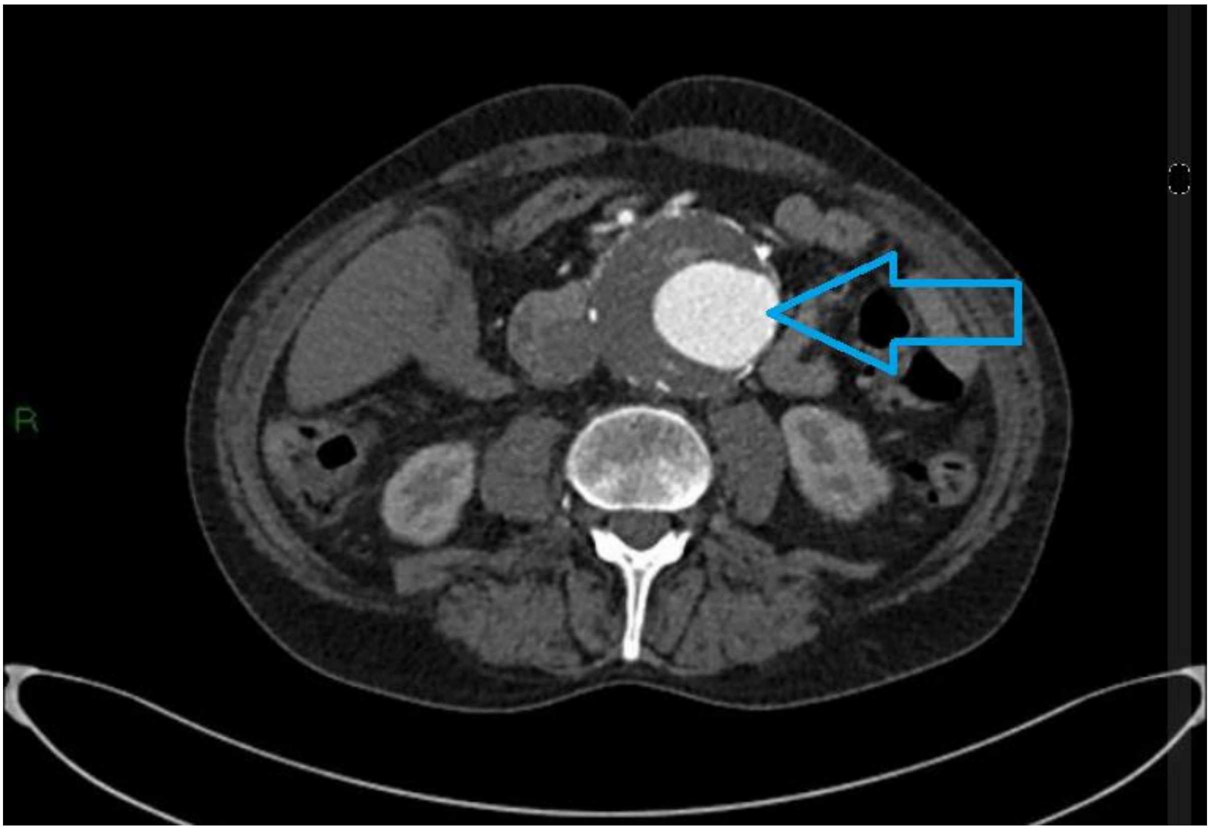

Figure 6 - Axial CT scan of 8cm AAA with lumen indicated [28]

1.2.2 What is Blood?

Blood is a combination of various constituents, all with their own specific behaviours and influences on the whole. These constituents are most commonly described as plasma, white blood cells, red blood cells, and platelets. While these four account for the majority of the blood volume, there is a fifth category which plays a major role in the study of thrombosis. This is the microscopic enzymes and proteins which permeate the entire circulatory system, albeit in tiny concentrations. When all of these constituents are in place, the fluid is called whole blood, that is, the substance which fills the vessels of any healthy person. To simplify research questions, some of these constituents are removed, isolated or changed.

1.2.2.1 Plasma

Blood plasma can be isolated to form a clear yellowish fluid containing the proteins and enzymes. This is useful for investigating coagulation effects without the influence of the larger blood cells, and allows the use of particle image velocimetry (PIV) - a method for accurately measuring the velocity of a clear fluid using suspended micro-particles and rapid photography [29]. When plasma is used in experiments without the reintroduction of platelets or other blood cells, it is called platelet free plasma (PFP) or platelet poor plasma (PPP). If platelets are reintroduced to the plasma, it becomes platelet-rich plasma (PRP). This substance is useful for in-vitro coagulation experiments, as the interaction of flow, platelets and enzymes is sufficient to generate thromboses [29].

1.2.2.2 White Blood Cells

White blood cells play a minor role in the physical and chemical mechanisms of thrombosis. Typically, passing cells will be caught in the fibrin mesh or gel and thus form some of the bulk of the clot. While their presence is vital for preventing infection when there has been injury to the vessel and exposure to an external environment, they may be unwelcome in aneurysm ILTs where the vascular wall is weakened but still intact. Some studies claim that these white blood cells create inflammatory enzymes which will lead to further degradation of the vascular wall, thus increasing the volume of the aneurysm bulge or even leading to rupture [3], [30].

1.2.2.3 Coagulation Enzymes

Blood enzymes can be isolated from plasma in order to investigate their effects individually, however, this is technically challenging. Pure samples of relevant coagulation enzymes are difficult to obtain, therefore the more common approach in experimental work is to inactivate certain enzymes. Corn trypsin inhibitor is used to inactivate coagulation factor XII [31], and snake venom is used to prevent the formation of fibrin [32].

1.2.2.4 Red Blood Cells

Red blood cells (RBCs) or erythrocytes are large biconcave cells which are responsible for the colour and opacity of blood. They play a passive yet significant role in coagulation. Firstly, they have phospholipid membranes which provide a surface upon which many of the coagulation reactions can take place [33], [34]. Secondly, the proportion of red blood cells (known as haematocrit) in the whole blood has been shown to affect the size and shape of the final thrombus [35]. This could be due to RBCs increasing blood viscosity, hence altering the haemodynamic environment. Higher viscosity would lead to longer residence time for thrombotic agents and promote faster clotting [33]. An alternate explanation is that passing

RBCs are often trapped by the clot and incorporated into its mass, thus more RBCs moving past the clot would lead to more entrapment. Finally, the RBCs exhibit visco-elastic behaviour, so their presence in the thrombus could have an effect on its mechanical properties. Densely packed and compressed RBCs in ILTs have been linked to greater resistance to thrombolysis [34].

1.2.2.5 Platelets

Platelets are small blood cells which play a vital role in coagulation. They are created in the bone marrow by the fragmentation of larger cells called megakaryocytes and typically last in the blood for 8-10 days [36]. They are typically $6\mu m^3$ in size and occupy about 3% of blood by volume [37], [38].

Platelets are usually in an inactive state in which they are flat and largely inadhesive; this allows them to circulate freely in the blood without causing undue coagulation. However, under certain conditions platelets are stimulated to activate. Once this happens, the cells change their shape and membrane properties in order to adhere better to each other and the damaged cell wall. This results in the aggregation of platelets which form the bulk of the thrombus volume [37]. Platelets also play an important role in the biochemical reactions which regulate haemostasis by providing a surface on which reactions can occur [39].

1.3 Theories of Thrombogenesis

What causes a healthy blood vessel to enlarge into an aneurysm is still unknown. While it is possible to observe the mechanisms associated with enlargement, it is still unknown what initiates this pathology. The same could be said of the intraluminal thrombus. The growth and maturation of the thrombus is better understood than the causes of its initiation. In the case of trauma leading to vascular dissection, the initiating cause is obvious, for example a cut from a knife which breaks the vascular wall. In that case the sudden interaction of flowing blood with subendothelial substances such as tissue factor (TF), von Willebrand factor (vWF) and collagen initiates coagulation through mechanisms common to thrombosis and haemostasis. In the case of ILT in AAA, the blood vessel is merely distorted not dissected. Flowing blood should have no contact with subendothelial substances and yet clotting still occurs. Some studies have shown that the endothelium and blood cells do generate TF [40], [41], though the relative significance of these two sources is still the subject of research.

The expression of von Willebrand factor at the endothelium is another potential contributor to thrombogenesis in AAA, however, murine experiments showed that ILTs can still develop - albeit at a reduced rate - in the absence of vWF [36]. What is clear is that vascular tissue in an aneurysm becomes more prone to platelet adhesion and thrombogenesis than surrounding healthy aortic tissue [42].

1.4 Platelet Activation and Adhesion

As mentioned earlier, platelets are continuously present in healthy human blood. Their role is to remain in solution in the flowing blood until such time as they are recruited to form a clot, then to play various important roles in the clotting process. In the case of vessel dissection, the first role of platelets is to form a ‘platelet plug’ at the site of haemorrhage in order to slow down and block escaping blood flow. In the case of ILTs, the ‘plug’ metaphor is not applicable to this mechanism; rather, the first stage is called ‘adhesion’ where platelets stick to the endothelium.

Initial adhesion occurs as a result of vWF molecules bonding to collagen in the vessel wall and receptors on the platelet membrane. The most significant initial bond is between vWF and a glycoprotein called GP1b in the platelet membrane. This glycoprotein is receptive to vWF bonding even when platelets are inactive, so as passing platelets bump into a thrombogenic section of blood vessel, they can be slowed, arrested and held in place [36], [42], [43]. Von Willebrand factor will also cause cross-linking between platelets by bonding GP1b and various other membrane-based glycoproteins together [44], [45]. These bonds between inactive platelets and the vessel wall are considered weak, and are likely to be broken in the high shear environment of the abdominal aorta [43].

This implies that reduced wall shear stress is a necessary precursor to ILT formation, thus creating a tantalising link between the haemodynamic environment created by the unusual aneurysm geometry and the propensity for localised intraluminal thrombosis. Many studies have sought to demonstrate a connection between thrombosis growth and haemodynamic conditions [2], [4], [46]–[50]. Unfortunately, the results are often contradictory, validation samples small, and modelling assumptions diverse. Studies also vary in how they define shear stress. Some calculate maximal systolic wall shear stress, others time-averaged wall shear stress over multiple heart beats, and yet others use oscillatory shear index, a measure of the changes in shear direction. Nevertheless, the research points towards a spatial correlation between low shear stress at the vessel wall and higher likelihood of ILT growth. Some studies even proposed a maximal threshold or bounded range of shear within which conditions are just right for thrombosis [2], [47].

It would be a mistake, however, to simply associate low shear stress to high thrombotic potential. The reality is that high shear stress in the blood can have a pro-thrombotic effect by means of platelet activation. Shear stress is sufficient to activate platelets even in the absence of chemical agonists [51]. The activation appears to correspond with cumulative damage to the platelet membrane as a result of dynamic and oscillatory shear stresses. This is of particular importance where the geometry of implanted medical devices such as stents or valves creates regions of ultra-high stress leading to increased thrombosis risk at the site of the implant [52].

A potent biochemical activator of platelets is thrombin. Thrombin is generated by a series of chemical reactions described later, but given that these reactions are initiated at a thrombogenic surface, thrombin is primarily present near the site of thrombosis. When thrombin comes into contact with protease-activated receptors (PARs) on the membrane of the platelet, it activates the platelet. Other dissolved substances such as adenosine diphosphate (ADP) and Thromboxane A2 (TxA2) are weak platelet activators [51], [53].

When platelets are activated, more glycoprotein receptors on the cellular membrane become receptive to bonding, most notably the GPIIb receptor. This receptor, once activated, will readily bond with vWF and fibrinogen [42]. Fibrinogen is a dipolar molecule which is plentiful in the blood. When each pole of fibrinogen attaches to the GPIIb receptor on neighbouring platelets, a strong and permanent bond is created [54]. This leads to two effects - firstly, platelets which were initially trapped by weak vWF-GPIb bonds will consolidate to form a stronger network as platelets become activated; and secondly, passing platelets are more likely to adhere to the fledgling clot if they are already activated. The result is that activation of platelets at the vessel wall or in the blood represents a powerful mechanism to increase the strength and growth rate of the clot after the initial adhesion. The phase wherein platelets are activated and form permanent bonds together is called aggregation [45].

The observation that platelets are prone to activation in regions of high shear but more likely to adhere to the vessel wall in regions of low shear, has led researchers to suggest that platelets play a large role in the site and shape of thrombus growth. The theory is that the irregular geometry of the proximal (upstream) end of the aneurysm creates turbulent flow in which shear stresses on fluid particles are elevated and platelets are activated. Once platelets are activated, they are either carried away with the bloodstream or become attached to the aneurysmal endothelium in areas of low shear [3]. Given that activation by shear is not instantaneous, one would expect to see greater aggregation of platelets in the distal part of the AAA, and indeed clinical observations do show this [47].

1.5 The Coagulation Cascade

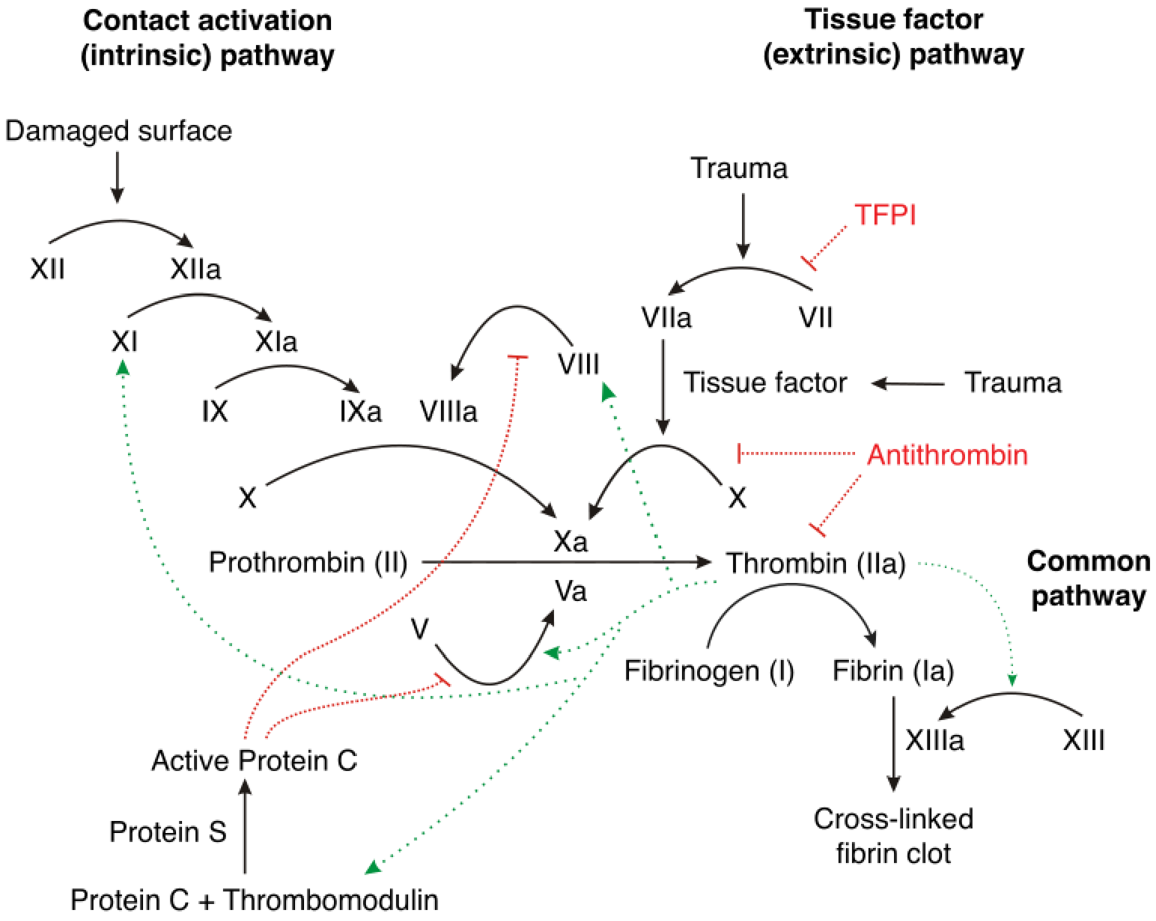

Figure 7 - Schematic of the coagulation cascade [55]

The coagulation cascade is a series of chemical reactions which ultimately produce thrombin. Thrombin has the capacity to activate platelets as mentioned before, but in addition to that, it catalyses the formation of fibrin from fibrinogen and interacts with other pro- and anticoagulant enzymes to modulate the thrombotic response. Given that slow or insufficient coagulant response would lead to haemorrhage, and overactive response could lead to vessel occlusion, it is vital that the coagulation system be tightly controlled. This goes some way to explain why the coagulation cascade is such a complex system of inter-related reactions. Another important feature of the coagulation cascade is gearing or amplification. This means that initiation by a small quantity of one enzyme can catalyse the creation of a larger quantity of the next enzyme which in turn catalyses a yet larger quantity of the next enzyme. The result is that a small initiating stimulus can lead to a rapid increase in thrombin. This process is typically broken down into three stages: initiation, amplification, propagation [56], [57]

1.5.1 Initiation

The initiation of the coagulation cascade starts with tissue factor. Tissue factor is present in the medial and adventitial layers of the blood vessel and has been shown to exist in blood cells and microparticles too. This so-called blood borne tissue factor may contribute to the initiation of ILT, however, at this stage it is not known to what degree [39], [40]. In the case of aneurysms, the endothelium is compromised to the point that vascular TF comes into contact with the blood. Tissue factor combines with activated factor VII in the blood to create the TF-VIIa complex. This complex reacts with other proteins to produce thrombin. This process is known as the extrinsic pathway and is described in more detail by Mackman et al. [40]. The extrinsic pathway is important for creating the first expression of thrombin, however, this thrombin in turn activates the intrinsic pathway which gradually takes over during the amplification phase.

1.5.2 Amplification and Propagation

As more platelets become activated the rate of thrombin generation and the quantity of thrombin increase rapidly [58]. This is due to a positive feedback loop where thrombin activates enzymes V and VIII which, in turn, promote the production of more thrombin. Over 95% of total thrombin production occurs due to the intrinsic pathway [56], however, there is still interaction both ways between the two processes [37]. Enzymes such as antithrombin and tissue factor pathway inhibitor (TFPI) will act to suppress the amplification of thrombin production, and the myriad of reactions between the many agonists and antagonists creates a dynamic and complex system which will not be described exhaustively.

An interesting feature of this system is that the region of peak thrombin generation begins at the vessel wall, but can move towards the centre of the blood vessel by means of a process called propagation. This is not to be confused with the natural advection and diffusion of a chemical species away from its source of origin - rather, the blood has been likened to an excitable medium, where catalysing enzymes will cause the blood in the bulk fluid domain (as opposed to the platelet plug region) to generate thrombin. This region of excitation can be thought of as a wave, which starts at the endothelium and moves into the fluid with an amplitude and speed dependent on the biomechanical and biochemical environment [32], [41], [59].

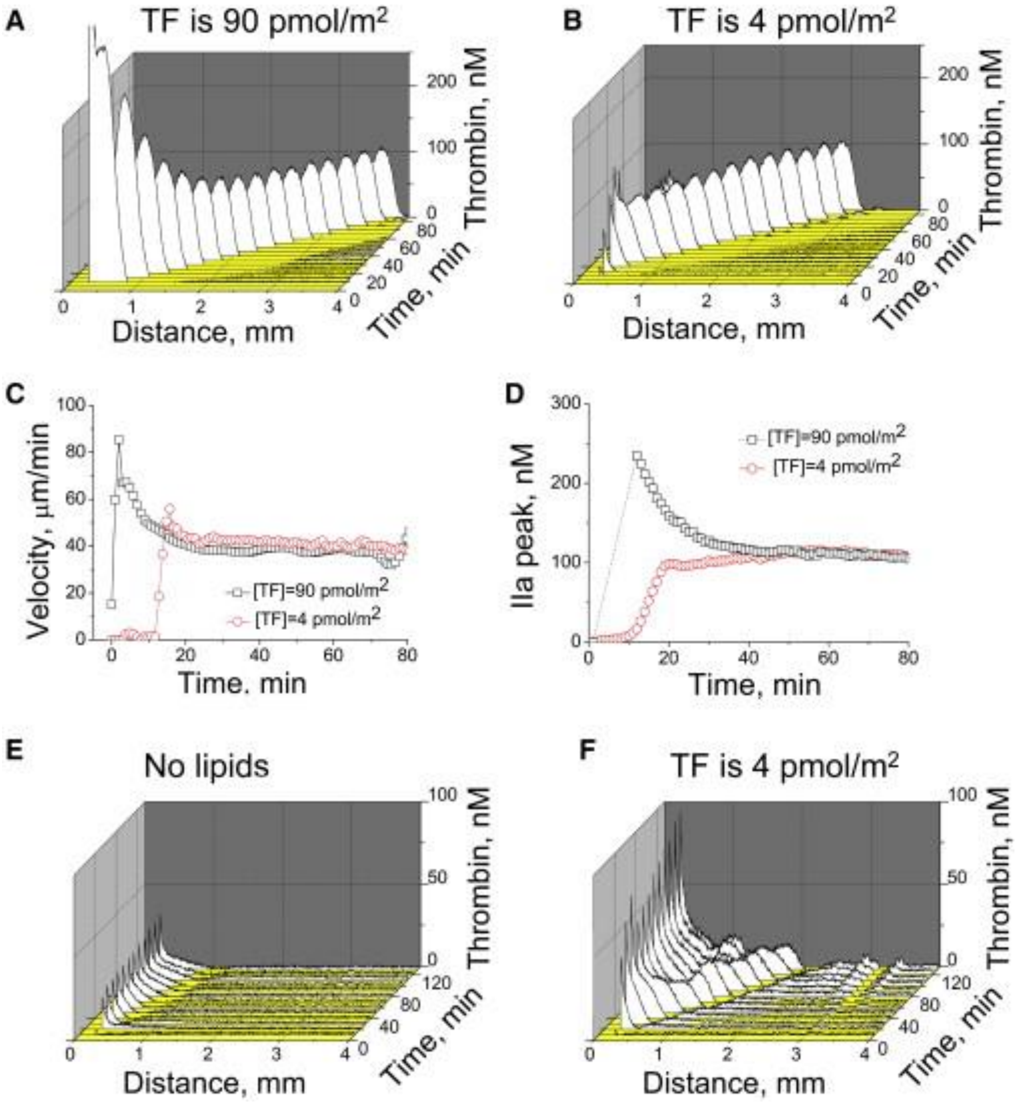

Figure 8 - Propagation of thrombin in blood plasma based on TF stimulation [32]

The propagating wave observation was shown in plasma where fibrin formation was blocked by the addition of snake venom and platelets were not present - hence no clot could form. Where a porous thrombus has formed over the endothelium the situation becomes slightly more complex. Proteins are macromolecules which can be hindered in their movement through the thrombus by the dense packing of cells and fibrin. Solute transport from the flowing blood into the centre of the thrombus and vice versa is hindered. Thrombin is generated by the interaction of prothrombin and prothrombinase, however, these two enzymes are primarily present in the fresh blood flow and thrombus core respectively. Only the region where both enzymes are present will generate thrombin, but as the clot grows in size and hindrance, that region will narrow and perhaps vanish. This mechanism may be a reason for the slowing or cessation of thrombus growth, however, although this has not yet been demonstrated conclusively [34], [60].

1.5.3 Decay

In stagnant blood where thrombin generation is initiated by any mechanism, the thrombin concentration can be seen to rise and then fall over time. The rise in thrombin levels can be explained by the dominance of procoagulant reactions, and conversely, as the thrombin levels fall, the anticoagulant reactions dominate to slow and ultimately cease thrombin production. This process is known as decay. The key substances which act as antagonists to thrombin generation are thrombomodulin and anti-thrombin. Thrombomodulin interferes with factors V and VIII, which are key to maintaining the intrinsic pathway. Antithrombin reacts with factors IXa and Xa to further suppress the production of thrombin by either pathway. In addition, antithrombin reacts with thrombin directly to neutralise it permanently [58].

The relative concentrations, efficacies and reaction rates of the procoagulant and anticoagulant substances can vary significantly between individuals, and can be severely out of balance in patients with haemophilia. In patients with aneurysms and thrombosis, the coagulation potential of a patient's blood is of great interest for both diagnosis and treatment. Various methods have been used in the past, however, pioneering work by Hemker et al. has led to the wide use of a test called the Calibrated Automatic Thrombogram. This test will be described in more detail later [61], [62].

1.6 Fibrin Generation, Morphology and Properties

The primary purpose of thrombin is to act as a catalyst for the conversion of fibrinogen to fibrin. Fibrinogen is a glycoprotein which is synthesised in the liver and circulates in the blood at fairly high concentrations compared to the proteins mentioned previously. In the presence of thrombin, fibrinogen molecules will be activated and become a fibrin monomer. These monomers will readily bond with each other to form long polymer chains known as fibrin strands. When these fibrin strands form over and between the agglomeration of platelets and blood cells, the result is a highly resilient composite - much like ropes tying down luggage on a trailer [43]. The powerful effect of fibrin on a clot is demonstrated in an experiment by Brass and Diamond. It was found that platelet deposits lacking fibrin could withstand maximal wall shear rates up to 5300 s^{-1} (159 dyne cm^{-2} wall shear stress), while a thrombus made of a combination of platelets and fibrin could withstand up to 83 000 s^{-1} (2500 dyne cm^{-2}) before embolization [63].

The relationship between fibrin and platelets is an interconnected one. The initial platelet plug creates a porous zone which acts like pebbles in a stream. Fluid velocities between the platelets are significantly lower than the flowing blood in the main stream [43], [63]. This quiescent zone provides sufficient residence time for blood-borne substances to react and form fibrin [50]. Aneurysms or deformations in the endothelium can create eddies and low velocity zones which may also create the conditions in which fibrin can form [41]. This protective effect of platelets is especially important in large arteries where flow velocity is at its highest. Without the protection of platelets it would be impossible for a fibrin mesh to form [64].

A study of fibrin formation in platelet free plasma at a microfluidic scale shed light on some of the key haemodynamic and biochemical factors which affect fibrin morphology [41]. The results show significant qualitative differences in the appearance of fibrin deposits when shear rate, thrombin concentration, and supply of fibrinogen are varied. The morphologies are classified as thin film, dense mat, or fibrous gel. What was notable was that the thickness of the fibrin strands themselves and the degree of cross linking between them varied greatly. At higher shear rates the quantity of fibrin and the thickness of the strands decreased.

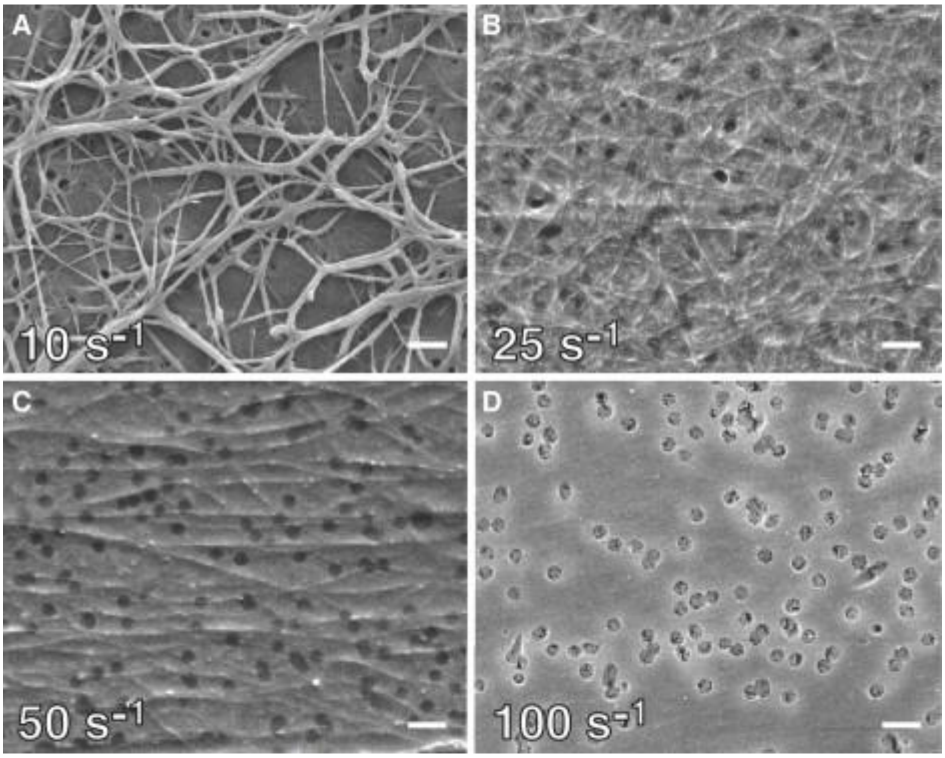

Figure 9- Effect of shear rate on fibrin morphology. Dark dots represent pores in membrane [41]

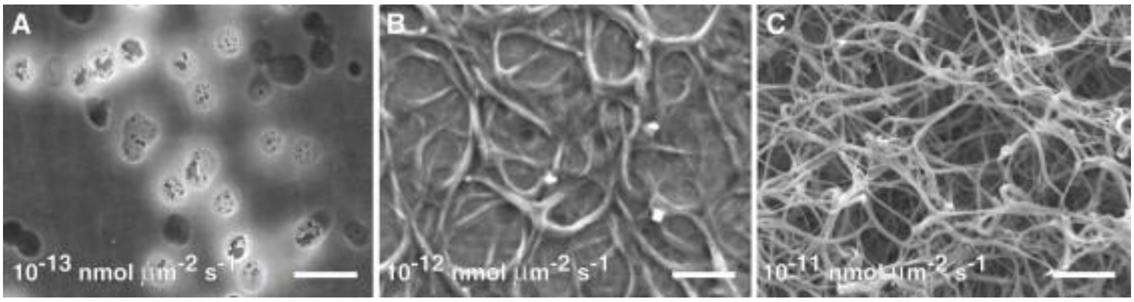

Figure 10 - Effect of thrombin flux on fibrin morphology. Dark dots represent pores in membrane [41]

Another study on this topic found that *"low thrombin concentrations produce fibrin clots that are turbid and composed of thick, loosely-woven fibrin strands. Higher concentrations of thrombin produce fibrin clots that are composed of relatively thinner, more tightly-packed fibrin strands"* [65].

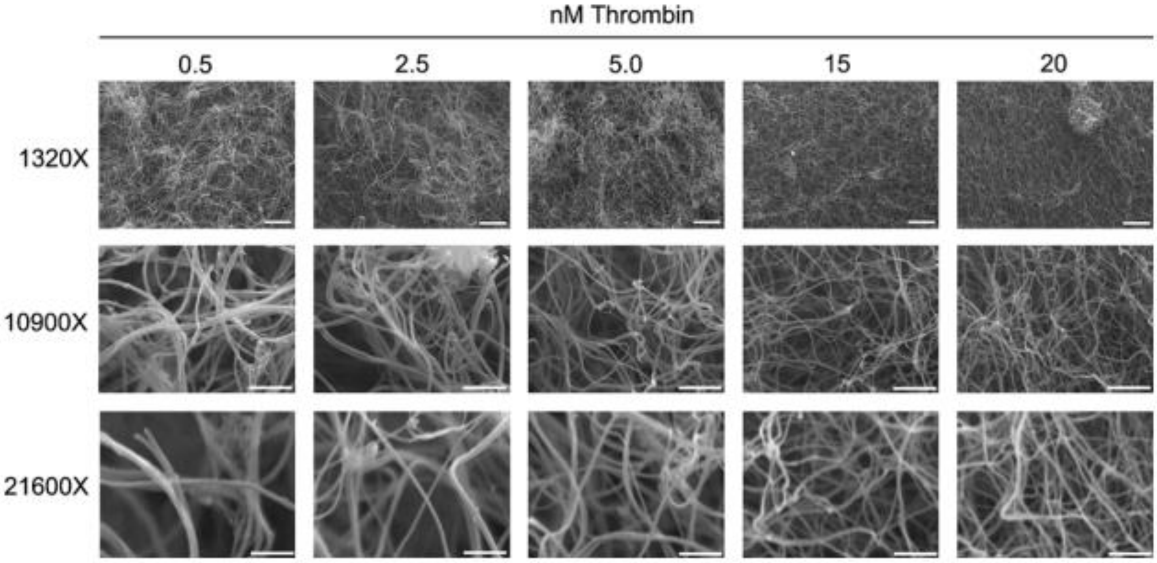

Figure 11 - Effect of thrombin concentration on fibrin morphology [65]

An experiment which sought to account for the haemodynamic effects of platelets on fibrin production used microscopic beads as a means of reducing convection rates or ‘washout’ of coagulation agonists [50]. The study posited that TF-coated silica beads can support coagulation in a way that is comparable to platelets for the purpose of this experiment. Platelet free plasma with supplemental fibrinogen was used, but unlike the previous study, no thrombin was introduced to the fluid. Instead, the tissue factor on the silica beads initiated the coagulation cascade resulting in the production of thrombin and then fibrin, and both of these substances were monitored over time in the experiment.

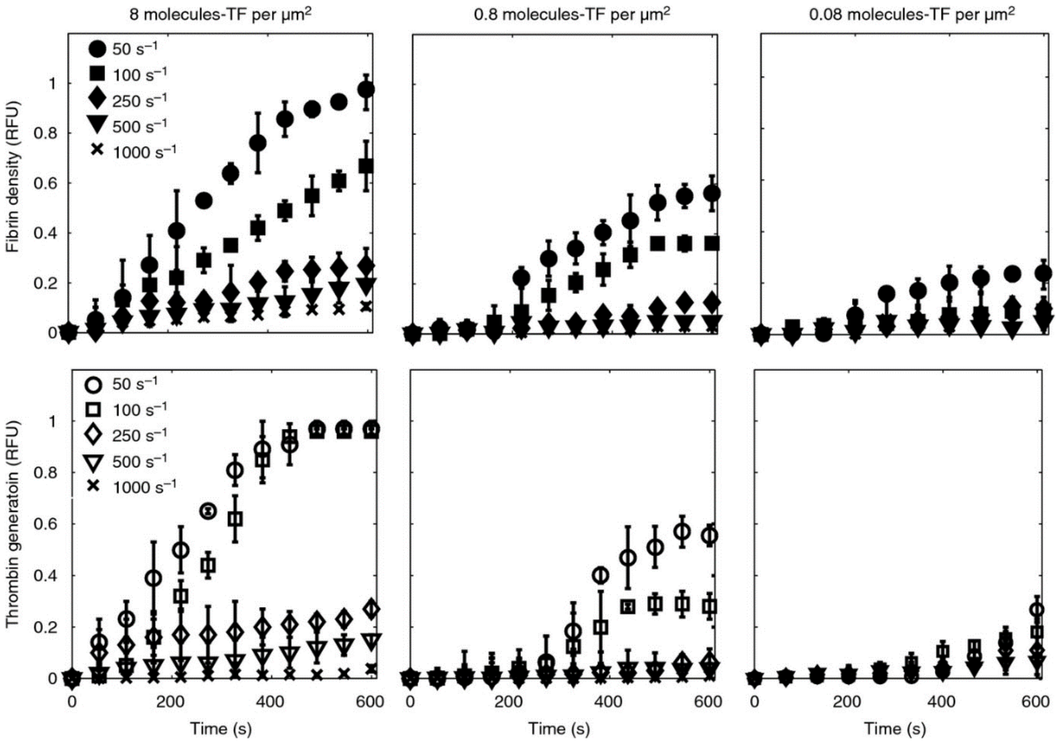

Figure 12 - Fibrin deposition and thrombin generation as a function of shear rate and tissue factor (TF) concentration [50]

Shear rates were varied between $50s^{-1}$ and $1000s^{-1}$ showing that as shear rate increases, thrombin concentration and fibrin density are reduced. At shear rates above $500s^{-1}$ both substances are present in such small quantities as to be practically insignificant. When shear rates were low enough to allow a fibrin gel to form, it was observed that fibrin growth rate and maximum size of clot increased as shear rate dropped, and also increased with the initial concentration of tissue factor on the silica beads. Thrombin density showed a similar response to these two variables - with negligible or low production at 0.08 molecules TF per μm^2, delayed production at 0.8 molecules/μm^2 and rapid production at 8 molecules/μm^2. This shows that the quantity of tissue factor available at the initiation of the coagulation process will have a proportional knock-on effect to the rate and quantity of the final products of the entire chemical cascade. Despite this dependence on tissue factor, the effect of shear rate was shown to be of greater impact on fibrin growth.

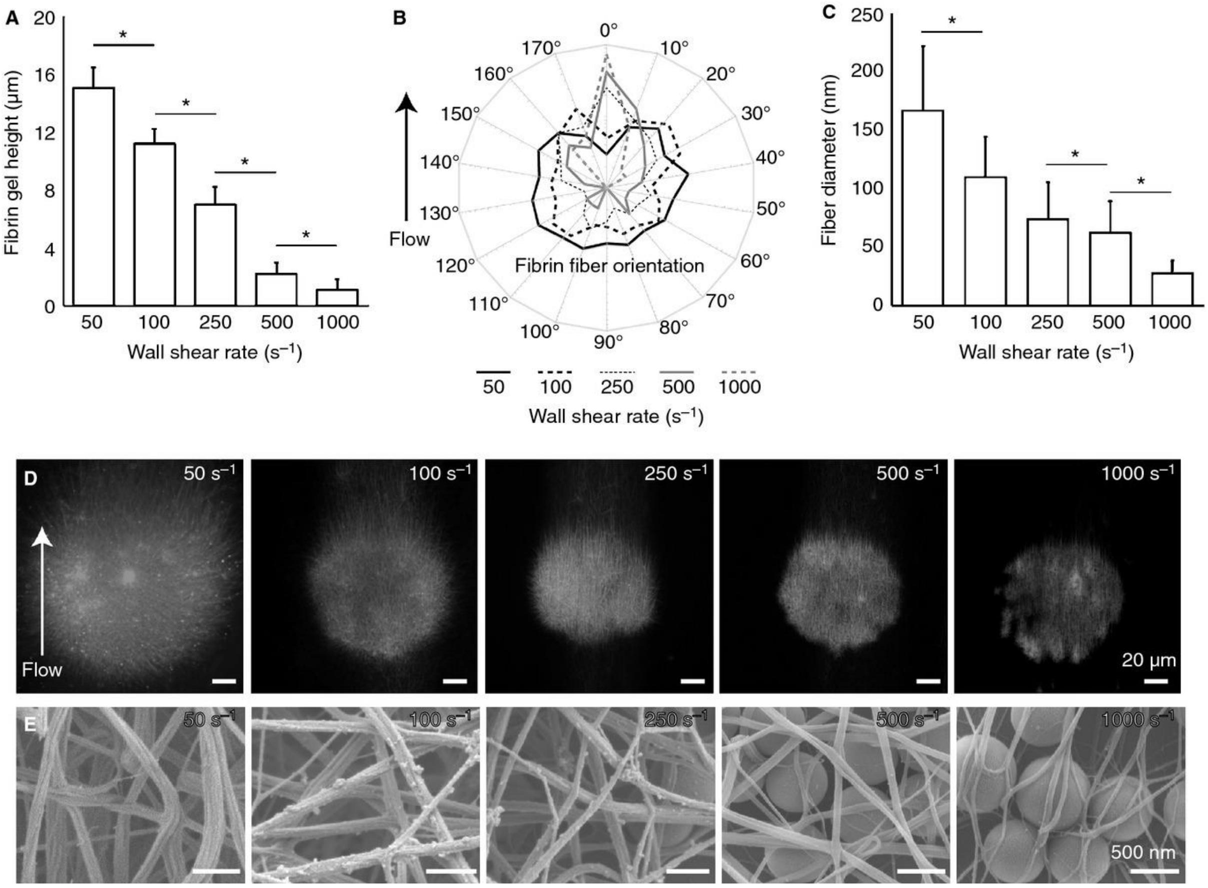

Figure 13 - Effect of shear rate on fibrin diameter, orientation and height [50]

A final point to mention about the morphology of fibrin is cross-linking between fibrin polymer chains. This is a feature of many other types of polymer and has a similar effect. Cross links increase the strength of the polymer and create a more three-dimensional matrix of bonds. The effect of cross-linking is a stronger fibrin mesh, and ultimately a more stable thrombus. Cross-linking is promoted by factor XIII which is present in the blood and is activated by thrombin [45], [66].

1.7 Thrombus Growth and Cessation

Many patients live with aneurysms which contain intraluminal thromboses for years with no ill effects. In these cases, the thrombus is either growing at a rate which can only be observed over long periods, typically measured in the order of mm per month, or has stopped growing completely. Some ILTs grow far more rapidly, often immediately after a surgical procedure, leading to severe complications or mortality. Full vessel occlusion or embolization has been observed one day [67] and even a few hours [68] after surgery for coronary artery repair. This shows that ILT growth rate is highly variable, and highly significant to predicting and managing the effects of AAAs before and after surgery. It is therefore of great clinical interest to understand the mechanisms which influence growth rate.

Many attempts have been made to correlate haemodynamic variables such as time-averaged wall shear stress (TAWSS), oscillatory shear index (OSI), and relative residence time (RRT) with thrombus growth rate. The result of one such study is shown in Figure 14 below [69]:

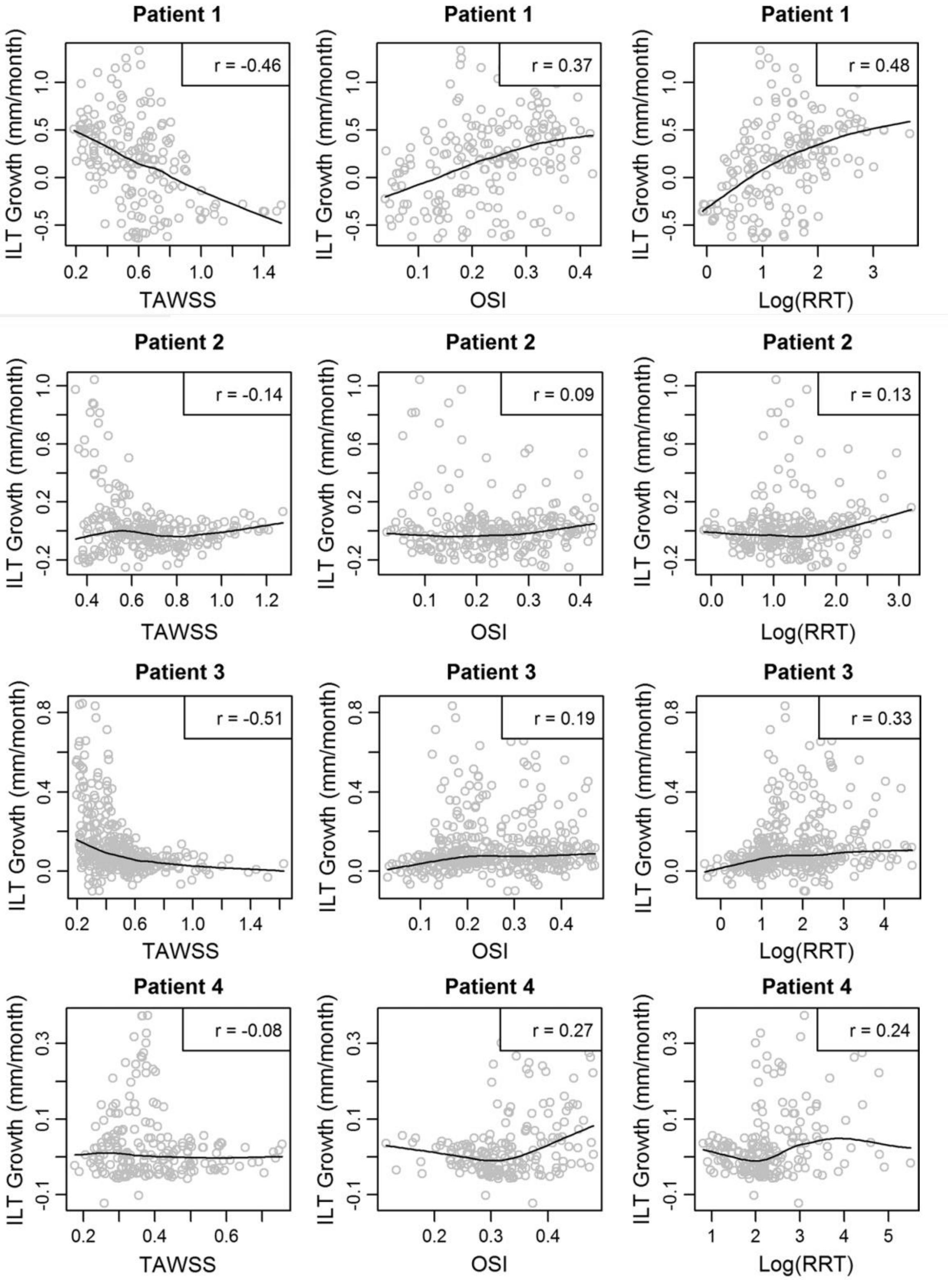

Figure 14 - Plots of haemodynamic variables and ILT growth rate for patients with significant thrombus deposition [69]

Figure 14 shows that haemodynamic variables may be of use in predicting slow ILT growth in some cases, but not all. As for rapid ILT growth, the type that occurs in a few hours, very little information exists on the causes and frequency of this phenomenon. Given the widespread application of vascular surgery (both open and endovascular), and the growing possibilities for other types of endovascular implants, it would be of great value to develop tools to predict likelihood and severity of rapid thrombus growth.

Cessation is another aspect of thrombosis where research could lead directly to improvements in diagnosis, management and treatment. Cessation can be defined broadly as a growth rate approaching zero for a significant period without surgical intervention. There are multiple factors which appear to contribute to this phenomenon, and these will be discussed below.

As mentioned previously, one proposed mechanism for cessation is based on the region in which thrombin can be produced. The proposition by Kattula et al. [34] was that prothrombin (the precursor to thrombin), which is present in the blood, has limited access to prothrombinase (a catalyst generated by both the intrinsic and extrinsic coagulation cascades), which is generated on phospholipid membranes within the thrombus. If transport of either of these substances is hindered by distance, densely packed cells, reduced diffusivity, or washout due to advection so that they cannot react and create thrombin, then cessation will likely be the result.

Another theory of cessation is based on the interaction between the blood flow and the platelets on the surface of the thrombus. It has been demonstrated that platelets can adhere to the thrombus only when shear stress at the surface is below a critical value. If the shear stress exceeds this value, the platelets will either not attach at all, or will attach momentarily then break off in chunks [70]. Initially the ILT tends to form in a region of low flow velocity where stresses are low. However, as the clot grows away from the vessel wall it can encounter more rapidly flowing blood, and thus experience higher shear stress at its surface. If the shear stress over parts of the surface of the thrombus exceeds the critical value, then platelet adhesion is unlikely, and existing platelets may be removed to expose the fibrin network below. This fibrin mesh can resist much higher shear stresses so this layer will remain as the outer layer of the thrombus until such time as the haemodynamic environment changes or the fibrin is broken down by biochemical processes [43], [64].

Another suggestion for a mechanism of clot cessation is based on the location and movement of thrombin within the thrombus. As mentioned previously, platelets can adhere to the thrombus surface weakly when they are inactive, but more strongly when they are activated [43]. Thrombin is a potent platelet activator, and if it is present at the surface of the thrombus then platelets are more likely to be activated and adhere to the thrombus permanently. However, if the surface of the thrombus is primarily fibrin - known as a fibrin cap - thrombin will only be generated deeper within the thrombus where tissue factor and phospholipid membranes are more abundant. The thrombin generated in the clot core may be washed downstream by intra-thrombus flow before it can reach the thrombus boundary. The effect of this is that platelets on or near the surface of the clot will be separated from the regions of high thrombin by the fibrin cap. Without thrombin, these platelets are not likely to become activated nor adhere to the thrombus. The conclusion is that a thick fibrin cap may contribute to cessation of clot growth [71].

1.8 Thrombus Composition

Clot composition has been shown to vary as the thrombus matures, and differences in haemodynamic and biochemical environments will likely cause significant differences between patients. Information of patient specific clot composition is not easily obtainable in-vivo, however, post-operative or post-mortem analysis of thromboses can give detailed information. The typical thrombosis constituents based on averages of many such analyses are shown in Table 1 below.

Table 1 - Average composition of ILTs

Fibrin	Platelets	Erythrocytes	Leucocytes	Reference
49.1 %	11.6 %	24.2 %	3.7 %	Sadowski [72]
55.9 ± 18 %	16.8 ± 18 %	11.5 ± 9 %	1.3 ± 2.0 %	Silvain [73]

1.9 Computational Models

Computational modelling of thrombosis and aneurysms in the past would focus on one aspect of the physiology - such as wall shear stress or tissue factor concentration - in order to draw some conclusions about the overall pathology. With increased hardware capacity and advancing knowledge, the trend has moved more towards integrated approaches which aim to capture as many of the chemical and mechanical intricacies as possible in one model. The following section will attempt to describe the key areas of interest and development in the field of aneurysm and thrombosis modelling, with reference to a wide range of experimental and computational work. The goal of this summary is to learn from the best techniques used by others, with a view to incorporating these techniques into a new model.

1.9.1 Modelling of Blood

The overwhelming majority of studies treat blood - or at least part of the blood - as a flowing continuum which can be described by the Navier-Stokes equations for incompressible fluids. In recent years there has been a move to more accurately represent the interactions between blood cells such as RBCs and platelets by modelling them as discrete particles or small volumes. This approach has the potential to represent physiological clotting and flow with great accuracy, as many of the key features of clotting take place due to the interactions between, or evolution of, individual blood cells or particles. For example, the Lagrangian approach to following a platelet as it enters the flow region would allow one to track the shear stress on the particle over time - thus predicting if that platelet becomes activated, adhered, or eroded from the clot surface [74].

While the discrete particle/volume approach is appealing for its potential accuracy, the computational costs are often prohibitively high [64]. Many studies have chosen to use a completely Eulerian approach and treat the various species in the blood as massless scalar quantities which are generated in certain regions or boundaries, react according to various rules inherent to the model, move due to advection within the fluid, and diffuse according to either the standard mechanism of Brownian motion or according to more complex diffusion models. These features, or partial combinations of them, are usually called CDR models, an acronym for Convection, Diffusion & Reaction. An exciting development in thrombosis modelling is the use of a combination of the discrete and continuum models to form hybrid models.

In a recent example [43], blood proteins such as fibrin and thrombin were calculated using an Eulerian CDR approach while plasma and platelets were treated as small Lagrangian volumes in the flowing medium. Platelets could be active or inactive, and a mechanism for greater bond strength between platelets was incorporated when sufficient fibrin was present to act as mesh. The results showed that as the thrombus grows, the inner bulk of platelets is firmly bonded by fibrin, but the outer ones are not. As the thrombus grows further away from the endothelium it enters a higher velocity region of the flowing blood - this increases the shear rate to a point where the outer platelets are stripped away, exposing the strong but fairly inadhesive fibrin-covered core. As mentioned previously, this is claimed to be a mechanism by which the thrombus would cease to grow.

A feature of the fluid continuum modelling approach which is often mentioned in the literature is the question of Newtonian vs non-Newtonian properties for the fluid - be it plasma or whole blood. There has been some disagreement among researchers on this topic, with some [37], [48], [75] believing that velocity fields calculated with a Newtonian fluid will be inaccurate, and therefore a model such as Carreau-Yasuda must be introduced to simulate shear thinning effects. Other researchers have shown that there are situations where the difference between Newtonian and non-Newtonian simulations is negligible - in which case it is acceptable to use the simpler Newtonian approach [2], [38], [76], [77]. Various factors can influence the choice of using a Newtonian or non-Newtonian fluid model, but in most cases the decision is based on the scale of the blood vessel or experiment. If the flow domain and features are microscopic, such as simulation of capillaries or intra-thrombus convection, then non-Newtonian is deemed necessary - but for larger vessels like the aorta with meso-scale thrombus modelling then Newtonian is a perfectly acceptable approach.

1.9.2 Modelling of Coagulation Reactions

Computational models which aim for maximum accuracy have sought to model the biochemical reactions of haemostasis explicitly and in great detail. There are dozens of enzymes, proteins, and chemicals which interact on various kinds of surfaces or in the fluid domain, so these models can be quite complex. As knowledge and computing power has increased, these models have grown to incorporate more and more features and refinements to generate more accurate results. A comprehensive review of these methods is beyond the scope of this project, however, it is necessary to talk briefly about the way in which biochemical reactions are typically simulated.

Initial concentrations are specified for all chemicals at the beginning of the simulation. Typically these initial concentrations apply to the entire fluid domain, though some are spatially limited to a certain region or boundary. During the course of the simulation the concentrations are not calculated explicitly, rather the rate of change of concentration for all chemicals are calculated at each time step and the actual concentrations are adjusted accordingly. A typical rate of change equation will incorporate the effects of convection, diffusion and reaction as shown in equation 1.1 below

$$\frac{\delta[\Phi]}{\delta t} = \nabla(\vec{v} \cdot [\phi]) + D \cdot \nabla^2[\phi] + S([\phi], [\gamma_1], [\gamma_2], \ldots, [\gamma_n]) \tag{1.1}$$

Where:

$[\phi]$ is the concentration of the enzyme or particle of interest, $\vec{v}$ is the fluid velocity, D is the diffusion coefficient, S is a source function and $[\gamma_n]$ is the concentration of other substances in the fluid.

The rate of change of a particular substance due to reactions is usually dependant on the concentration of one or more other substances in the same computational cell. The simplest representation of this relationship is by means of a linear rate constant.

$$S_1 = \frac{\delta[\gamma_1]}{\delta t} = k_1[\gamma_1] + k_\mathrm{n}[\gamma_\mathrm{n}] \tag{1.2}$$

Where:
k_1 and k_n are rate constants, $[\gamma_1]$ is the concentration of the subject which is changing and $[\gamma_n]$ is the concentration of any other substance of interest in the cell.

This approach is used to model the generation of coagulation chemicals in the Leiderman Fogelson model [78]. An alternative to this formulation which has the potential to more accurately capture the non-linear reaction kinetics present in coagulation reactions is called Michaelis-Menten kinetics. This formulation was intended to simulate the effect of a catalytic enzyme on the conversion of a substrate to a product - for example, the conversion of fibrinogen to fibrin catalysed by thrombin [37]. The reaction process with initial, intermediate and final state is shown in equation 1.3 below:

$$Fg + Th \xrightarrow{k_\mathrm{f}} [Fg\,Th] \xrightarrow{k_\mathrm{cat}} Fn + Th \tag{1.3}$$

Where:
Fg is Fibrinogen, Fn is Fibrin, Th is Thrombin and k_f and k_{cat} are rate constants. The source of fibrin is no longer defined by purely linear kinetics, but according to the Michaelis-Menten formulation as shown in equation 1.4 [79]:

$$S = \frac{\delta[Fn]}{\delta t} = k_\mathrm{cat}\left(\frac{[Fg][Th]}{K_M+[Fg]}\right) \tag{1.4}$$

Where square brackets represent concentration. This formulation of reaction kinetics can be visualised as a graph of reaction rate (S) to substrate concentration $[Fg]$ as shown in Figure 15 below:

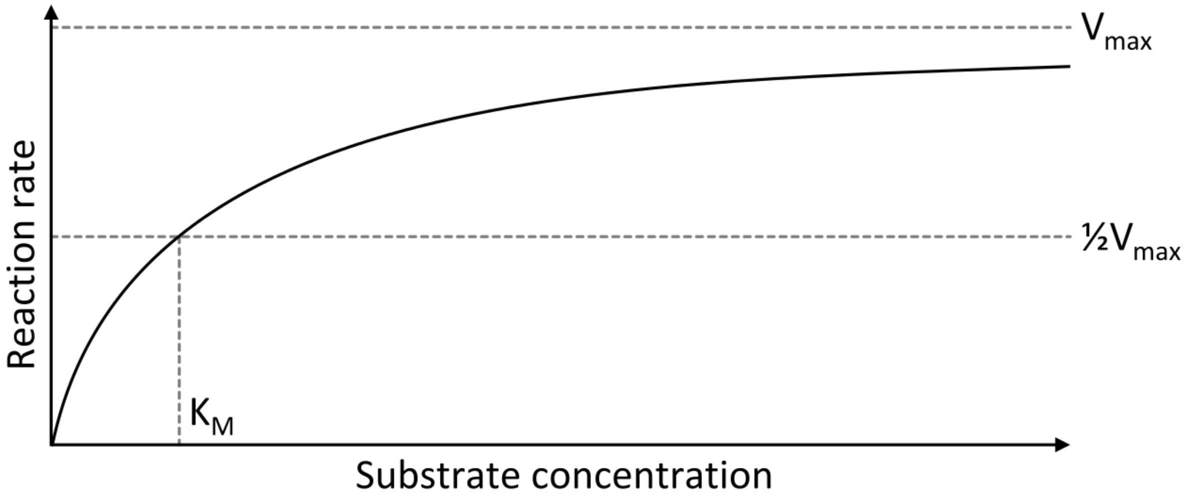

Figure 15 - Diagram of Michaelis-Menten reaction kinetics [79]

Where V_{max} is the theoretical maximum reaction rate in the presence of saturating substrate concentration and K_M is a constant equal to the substrate concentration at which the reaction rate is half of V_{max}.

Most explicit biochemical models use a combination of the linear rate and Michaelis-Menten reaction kinetics to model coagulation reactions, with some including the effects of reaction inhibitors and some not. Some models consider the production of thrombin as the end point of the coagulation cascade, while others include the production of fibrin as the final step. All of these models make use of reaction constants such as k_{cat} and K_M shown above in order to calculate reactions rates. These values are typically drawn from experimental work, but given that the product of a preceding reaction becomes the catalyst of the following one, the final result is highly sensitive to inaccuracies in these constants. The interdependence of the reactions in the coagulation cascade and the large number of variables makes explicit biochemical modelling a challenging approach. A simpler and more accurate method for representing thrombin generation in the blood would be of great benefit to thrombosis modelling. One such method which shows potential is the Calibrated Automated Thrombogram (CAT) [74].

1.9.3 The Calibrated Automated Thrombogram

This test aims to quickly and accurately represent the concentration of thrombin over time for a specific patient using a single drop of the patient's blood. The plot of concentration vs time is called the thrombin generation (TG) curve, and the shape of this curve provides a simple and graphical means to quantify the outcome of the many complex and competing biochemical reactions involving the pro- and antithrombotic substances in the blood.

The test typically follows the following procedure. A sample of blood is taken from the patient - in some cases this blood is used whole, but in some tests erythrocytes and platelets are removed as they would obstruct the results. A synthetic fluorogenic or chromogenic substance is mixed into the sample, then thrombin production is initiated by the addition of a triggering agent containing tissue factor, phospholipids and calcium ions. As thrombin is generated, it reacts with the synthetic substrate to cleave fluorophores or chromophores. These substances emit light, and as thrombin concentration increases, so does the number of light-emitting particles. The output of light is continuously monitored, and this data is used to reconstruct a profile of thrombin concentration over time. The test is also conducted with a known and constant concentration of thrombin to calibrate the results of the blood test [61], [80].

This test has been useful in many clinical applications, for example, identifying hypocoagulant or hypercoagulant conditions in the blood, and for comparison studies to show the effect of drugs, aging or cardiovascular disease [81], [82]. Unfortunately, there is not yet consistency in the parameters and methods used for CAT tests, so comparison between one study and another is problematic. For example, the concentration of TF in the substance used to initiate clotting can vary from 0.5 pM/L to greater than 10 pM/L, with higher concentrations leading to quicker clotting times and more thrombin production [80], [82]. Standardisation is necessary before the CAT can have full clinical value for precise diagnosis and/or computational modelling. Fortunately efforts to standardise these tests are showing promise [83], so in the near future the CAT has the potential to act as a simple, fast, universal, patient specific and quantitative representation of coagulation response for clinical use, but also as a replacement for complex biochemical models used in simulations.

1.9.4 Modelling of Thrombus

1.9.4.1 Platelets

Given the important role played by platelets in coagulation, most computational models seek to account for their presence in some way.

Anand, Rajagopal and Rajagopal [37] treated platelets as massless substances within the fluid, representing their concentration by means of scalar quantities which take part in convection, diffusion and reactions within the fluid flow field. Platelets were split up into activated and resting concentrations and tracked separately. Leiderman and Fogelson [78] treated platelets as a single concentration, with a maximum value based on the estimated size and packing density of platelets in a clot. Within the platelets present, a second variable represented the fraction of bound or unbound platelets, and a probability function based on thrombin, ATP and shear rate controlled the conversion from bound to unbound. Tomaiuolo [84] claimed that it is not necessary to model platelets directly; altering the porosity fraction of computational cells is sufficient to represent a clotted region. Tosenberger [43] used a discrete particle approach to platelets, treating them as cylindrical particles which can bond together by various means and interact with the continuum fluid around them.

1.9.4.2 Fibrin

While some models do not model fibrin generation at all, those that do use a variety of methods. Xu [85] treated fibrin production rate as directly proportional to thrombin concentration. Tosenberger [43] modelled fibrin generation rate as directly proportional to the product of thrombin and fibrinogen concentration. Virag [5] treated fibrin generation as proportional to platelet concentration and inversely proportional to fibrin density within the clot, assuming that there is always sufficient supply of fibrinogen from the blood. The majority of models [37], [38], [86], [87] use Michaelis-Menten kinetics, with fibrinogen as the substrate, thrombin as the catalytic enzyme and fibrin as the product. An interesting similarity is that Anand [37] used a concentration of fibrin above 600 nM/L as the criterion for representing blood as clotted, whereas Bodnar [38] used 1000 nM/L.

1.9.4.3 Porosity

As mentioned in the section on platelets, Tomaiuolo [84] used porosity to represent the clot, claiming that this was sufficient to capture the haemodynamic effects in and around the thrombus. Porosity is typically represented as a number between 0 and 1, where 0 is a totally impermeable solid, and 1 is free flowing fluid. Computational solvers like ANSYS Fluent will use this fraction to reduce the effective volume of a computational cell. Momentum and mass is still conserved as the fluid moves through the porous zone, but as porosity reduces, the fluid must squeeze through a smaller volume. The result of this constriction is that the local velocity of the fluid tends to increase. This result is not necessarily desirable, and when this approach was used for this thrombosis model, higher velocity magnitudes were found within the clot than without. This outcome seems unlikely, and motivates for the incorporation of a viscous resistance or permeability term to reduce the velocity. Indeed the ANSYS Fluent user guide [88] recommends the incorporation of both when modelling porous zones, but more detail on this is given in the next section.

The concept of porosity is refined further in papers by Brass and Tomaiuolo to include two zones within a stable thrombus, namely the core and shell [77], [84]. The core is characterised by higher fibrin concentrations and more densely packed platelets than the shell, so the core can have a porosity between 0.2 and 0.4, whereas the shell has a porosity in the range of 0.4 to 0.7. Visualisations of these two zones within the thrombus are currently limited to diagrams, as CT scans and MRI both lack the sensitivity to differentiate between the variations in density and composition. Confocal fluorescent microscopy has been used to generate some images of the two zones, however, the relative size and of core and shell within a thrombus is still the subject of research.

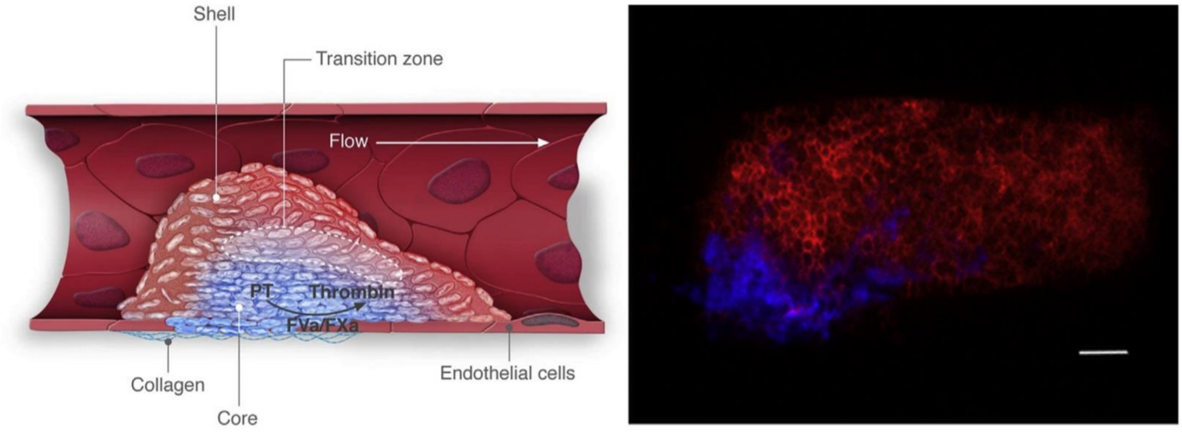

Figure 16 - Diagram of typical core and shell morphology in ILTs (left). Confocal fluorescent microscopy image of markers for core (blue) and shell (red) [89]

1.9.4.4 $u = -\left(\frac{k}{\mu}\right) \cdot \Delta P uk = 3E - 16 \cdot (\Phi_{\mathrm{f}} - \Phi_0)^{1.8}$Viscosity and Permeability

A complete computational model of thrombosis needs to represent the effect of the thrombus on the haemodynamic environment and vice versa. Given that the thrombus is not a solid mass, some fluid will flow into and through the clotted region. The way in which this fluid flows, and the resistance offered by the thrombus, has been modelled in various ways. Some examples are described below.

Anand used the Oldroyd-B formulation to model blood as a non-Newtonian fluid, so within the clot region they altered the properties of this model to give the effect of a more viscous fluid [37]. Bodnar altered viscosity as a linear function of fibrin concentration, with a maximum viscosity for a fully clotted region being 100 times higher than the viscosity of blood [38]. While altering the viscosity directly is a possibility for modelling a clot, it is more common to see the effect of viscous resistance modelled according to Darcy’s Law.

Darcy’s Law is the fluid equivalent of Ohm's Law for electric circuits, where the flow velocity is current, pressure drop is potential difference, and resistance is a permeability variable (k) divided by dynamic viscosity. The law is typically written in the following form

$$u = -\left(\frac{k}{\mu}\right) \cdot \Delta P \qquad (1.5)$$

Where:

u is the superficial velocity through the porous region, μ is the dynamic viscosity, k is the permeability and ΔP is the drop in pressure through the porous region.

Dynamic viscosity is defined by the fluid itself, and in the case of Newtonian fluids will remain fixed and constant. The permeability term is defined by the environment through which the fluid is flowing, and represents the level of resistance that the porous zone (in this case the thrombus) will provide against the fluid flow. A k value of unity represents a perfectly permeable fluid domain, i.e. no hindrance to flow. As k approaches zero, permeability reduces and flow is hindered, i.e. higher pressure difference is required to drive the fluid at a given velocity. The effect of Darcy's Law in the context of a continuum model of fluid flow is represented as a momentum sink in the continuity equation. The result is a set of equations known as the Brinkman equations, or alternatively the Navier-Stokes equations with the addition of a Brinkman term.

Various studies have sought to find a value for the permeability of an ILT [63], [86], however, given the variability between the structure, age, and constituents of clots, results can vary by up to 5 orders of magnitude [90]. Experimental work by Muthard showed that under a constant pressure differential of around 21 mm-hg, permeability was dependent on fibrin concentration. For clots grown with an absence of fibrin, the permeability was 5.45 E−14 cm^2, however, a thrombus containing platelets and fibrin had permeability of 2.71 E−14 cm^2 [91]. Kim attempted to take this into account by calculating permeability as a function of the fibrin density in the clot according to the following relationship [71]:

$$k = 3E - 16 \cdot (\Phi_\text{f} - \Phi_0)^{1.8} \qquad (1.6)$$

Where:
Φ_f is the volume fraction of fibrin and Φ_0 is a constant of 0.0028.

Wufsus [90] took this a step further and developed a method to estimate total permeability based on fibrin and platelet density. The equations are too complex to reproduce here, but the results are summarised in Figure 17:

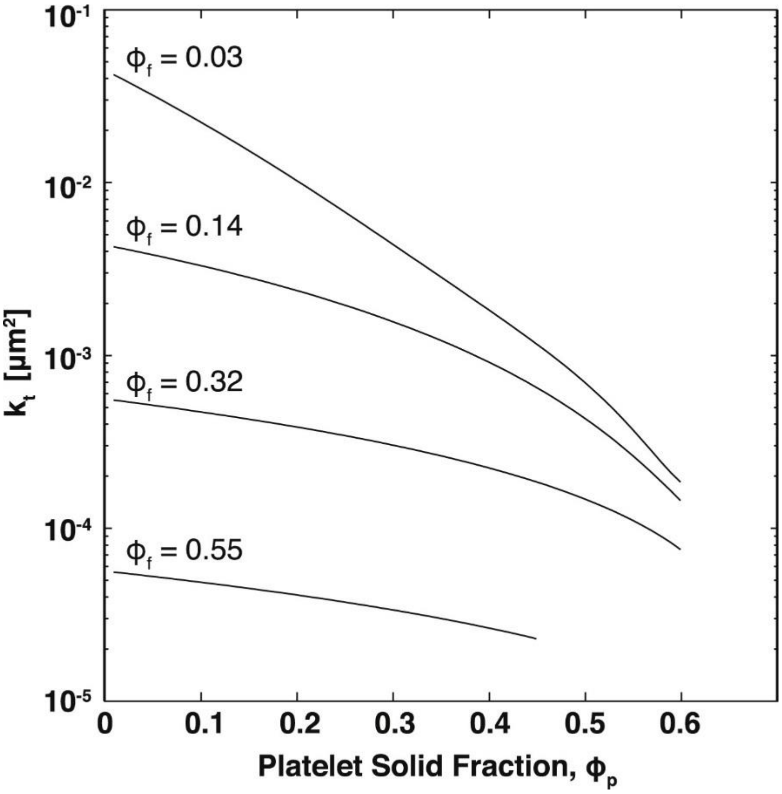

Figure 17 - Permeability of thrombus based on platelet and fibrin volume fraction [90]

1.9.4.5 Enzyme Diffusion

Much experimental work has been done to discover the rate at which the coagulation enzymes diffuse through the blood. Tables showing the diffusion coefficients of all of the major substances within the coagulation cascade are readily available [75], and many coagulation simulations make use of these alone to model diffusion of coagulation factors within the blood and thrombus.

There is, however, reason to believe that diffusion within the clot should not be treated in the same way as diffusion within blood. Coagulation proteins like thrombin are macromolecules, so as the clot becomes densely packed with platelets, fibrin and blood cells, the gaps or paths between these blockages can become small enough to hinder the movement of proteins [60], [77], [84]. This hindrance effect is quantified by a unitless number called tortuosity. Tortuosity is the fraction of the regular diffusion constant (D) in a fluid over the effective diffusion constant (D_{eff}) within the hindered region. Voronov found that tortuosity is between 2 to 2.5 in clots from mice [63], whereas Leiderman & Fogelson treat tortuosity as a function of platelet density which can reach a maximum of 1000 for a dense clot [60].

The values and methods used to model hindered diffusion clearly show significant disagreement, nevertheless its physiological significance has been the subject of various studies. Leiderman & Fogelson suggested that hindered diffusion could contribute to slowing or cessation of late thrombus growth [60]. Tomaiuolo showed that hindered diffusion, rather than advection, is the dominant mechanism responsible for molecular movement within the thrombus [84], however, Brass showed the diffusion alone would be so slow that it would take days for a protein to travel just millimetres within a clot [77].

1.9.4.6 Lysis

In continuum models clot lysis is typically approached from two directions. Firstly, there is biochemical fibrinolysis as a result of plasmin, a reaction that can be modelled in ways very similar to the coagulation cascade. Some fairly recent studies ignore this effect [84], [87], while others [37], [38] use Michaelis-Menten kinetics where plasmin is the catalyst and unbound/deactivated fibrin is the product. A difficulty with fibrinolysis, and perhaps the reason it is not often used, is that it is not clear what effect this reducing fibrin concentration will have on the clot. Clearly it will reduce the mechanical strength of the thrombus, but to what extent and at what level is not well understood. Anand proposed that a fibrin concentration of 600 nM/L should be the threshold below which a clot can be said to have dissolved or broken up [37].

The second direction is based on mechanical rather than chemical lysis, and is called thrombolysis. This erosion is due to stresses on the surface of the thrombus caused by the flowing blood. In order to find the shear stress levels at which clots begin to break up and fracture, Riha used a rotational rheometer and freshly clotted human blood to generate experimental results [92]. Haematocrit (volume fraction of red blood cells) of the blood samples was controlled to three levels, with lower haematocrit leading to more fracture resistant clots. For a haematocrit of 40%, a shear stress of 211 ± 43 Pa was found, and this value was used in a following computational model by Anand as the limit for clot dissolution [37]. Colace used a microfluidic device to test the shear rate at which embolization occurs from thromboses with and without fibrin. Clots with fibrin were significantly more resistant, demonstrating a maximum shear rate of 80 000 s^{-1} [93]. All these papers emphasize that the shear stress at which thromboses rupture or embolize is dependent on the concentration of fibrin and platelets within the clot, however, none present an explicit relationship between these variables.

Virag attempted to take this into account by including a fibrin degradation rate which is proportional to plasmin concentration and inversely proportional to fibrin concentration and mechanical strEtc.h. Notably this model also included the first order degradation of platelets deep within the thrombus [5].

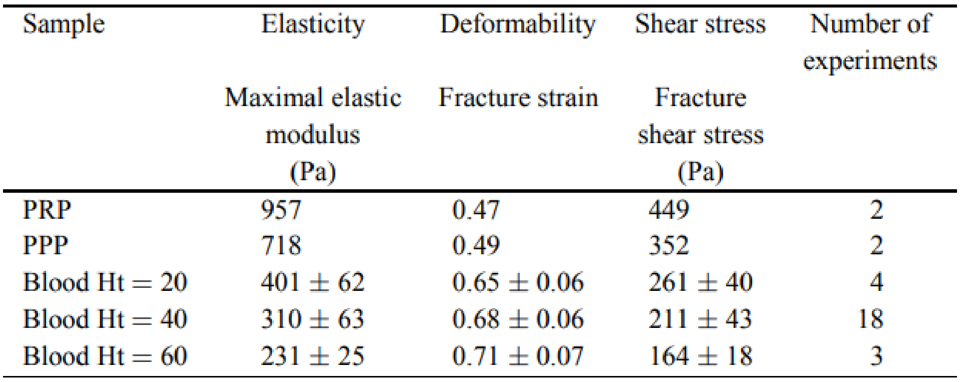

Sample	Elasticity	Deformability	Shear stress	Number of experiments
	Maximal elastic modulus (Pa)	Fracture strain	Fracture shear stress (Pa)	
PRP	957	0.47	449	2
PPP	718	0.49	352	2
Blood Ht = 20	401 ± 62	0.65 ± 0.06	261 ± 40	4
Blood Ht = 40	310 ± 63	0.68 ± 0.06	211 ± 43	18
Blood Ht = 60	231 ± 25	0.71 ± 0.07	164 ± 18	3

Figure 18 - Mechanical properties of thromboses grown in various blood and plasma types [92]

1.9.5 Vessel Size and Environment

In reality, every aneurysm is unique, varying considerably in size, aspect ratio, position, degree of asymmetry, and overall shape. The geometry of the flow domain is one of the most important factors to consider for thrombosis modelling because this geometry affects flow patterns and shear stresses and these in turn will affect enzyme transport, thrombolysis, platelet activation Etc. [30]. Kadri investigated injured blood vessels without aneurysms, and showed that geometric features such as vessel diameter and injury length dictate the maximum volume of a thrombus [89]. One can assume these features will be significant in the presence of an aneurysm too.

Ideally, computational models would treat each patient on a case-by-case basis and adjust the geometry to be physiologically representative. Rayz used patient specific geometry and blood flow conditions to model intracranial aneurysms of three patients which were initially free of thromboses. After several months, the clots had grown, and MR imaging showed good correlation between the regions of these clots and the regions with slow or recirculating flow in the haemodynamic simulation [48]. This result shows that accurate thrombosis simulations are possible even without bio-chemical coagulation reactions, provided the haemodynamic model has sufficient refinement.

Where patient-specific geometry is unavailable or where the focus is on other parts of the simulation, it can be useful to use a representative or typical geometry for AAAs. Unlike intracranial aneurysms which are typically saccular, AAAs are usually spindle or fusiform in shape [3]. As mentioned previously, surgical intervention usually occurs when the AAA grows larger than 5cm in diameter so it is more useful to simulate AAAs smaller than this, yet large enough to generate noticeable flow vortices.

Finol used an aortic diameter of 1.6 cm and a fusiform aneurysm with a maximum diameter of 4.8 cm which was offset from the centreline by various distances to study the effect of asymmetry. The results showed that with increasing asymmetry, the wall shear stress on the distal side of the aneurysm midpoint increased and the flow vortices changed size and position [76].

Virag used an idealised axisymmetric fusiform geometry which has an interesting mechanism where the aneurysm can grow in diameter yet the lumen of the blood vessel remains a constant diameter due to the immediate deposition of thrombus in the extra space. No dimensions were given for this particular study [5].

Biasetti used an axisymmetric fusiform geometry with inlet and outlet vessel diameter of 2 cm and maximum aneurysm diameter of 4.4 cm. The study argued that results from 2D and 3D simulations of this geometry were similar enough to warrant the use of a half-plane from central axis to vessel wall as the flow domain. An interesting addition to this study was to vary the size and position of the aneurysm wall which was treated as ‘injured’. In this injured zone, TF:VII complex has a concentration of 1e-6 nM which triggers the coagulation cascade, whereas the rest of the vessel was left as inert. A larger injured region showed increased thrombin concentration as expected, but notably when the injured zone was placed at the proximal neck of the aneurysm, the region of peak thrombin was still in the distal half of the aneurysm bulge. This ties in with clinical observations, which show the bulk of ILT thickness to be in the distal half of fusiform aneurysms [75].

Another finding of this paper was to show the birth, movement, and destruction of toroidal vortexes in fusiform aneurysms as shown in Figure 19, and following from that, the way in which vortices influence the distribution of thrombin in the flowing blood as seen in Figure 20.

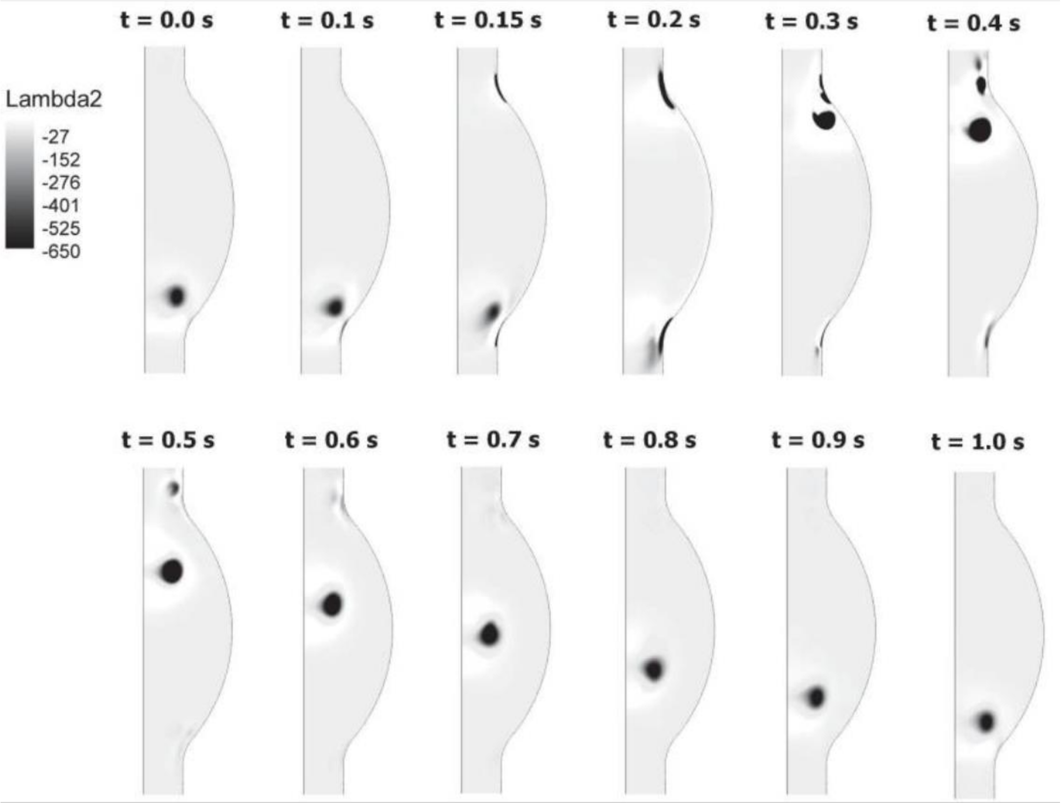

Figure 19 - Initiation and movement of vortical structures during one heartbeat pulse [75]

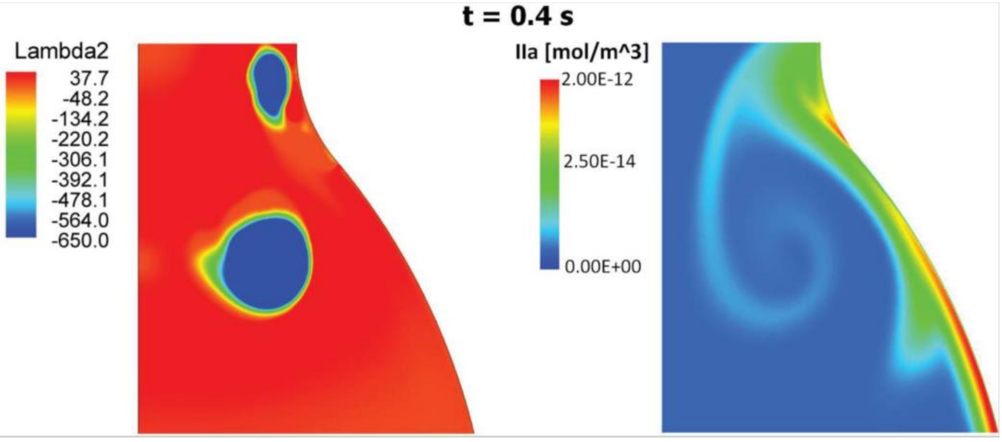

Figure 20 - Effect of vorticity (Lambda 2) on distribution of thrombin (IIa) [75]

1.9.6 Boundary Conditions

In any fluid dynamics simulation, the boundary conditions are key. In order to create a useful and well-defined simulation, one must first know exactly what the boundary conditions are in reality, and then apply them in a way which balances accuracy and computational simplicity. In the case of the aorta, simulations typically have one inlet which defines velocity based on the cardiac output, one or multiple outlets (depending on whether the model takes into account arteries which branch off the aorta), and finally the wall of the blood vessel which in reality is flexible but is most often modelled as a rigid geometry.

1.9.6.1 Inlet Velocity Profile

A unique problem for patient-specific models of haemodynamics in blood vessels is the collection of accurate flow data. Invasive methods are obviously problematic, especially for patients already at risk of aneurysm rupture or embolization, so various studies have sought to use non-invasive methods to derive values of flow rate over time. The graph of flow rate over time for the duration of one heartbeat shall be referred to as the flow waveform.

One of the early attempts was conducted by Mills in 1970 by means of direct catheterisation. The result showed an initial peak during systole followed by a secondary pulse of lesser magnitude [94]. Despite more accurate measurement technology, this profile was still in use recently. Finol et al. normalised the period to 1 second and used discrete Fourier transforms to represent the waveform as a function in their computational model [76].

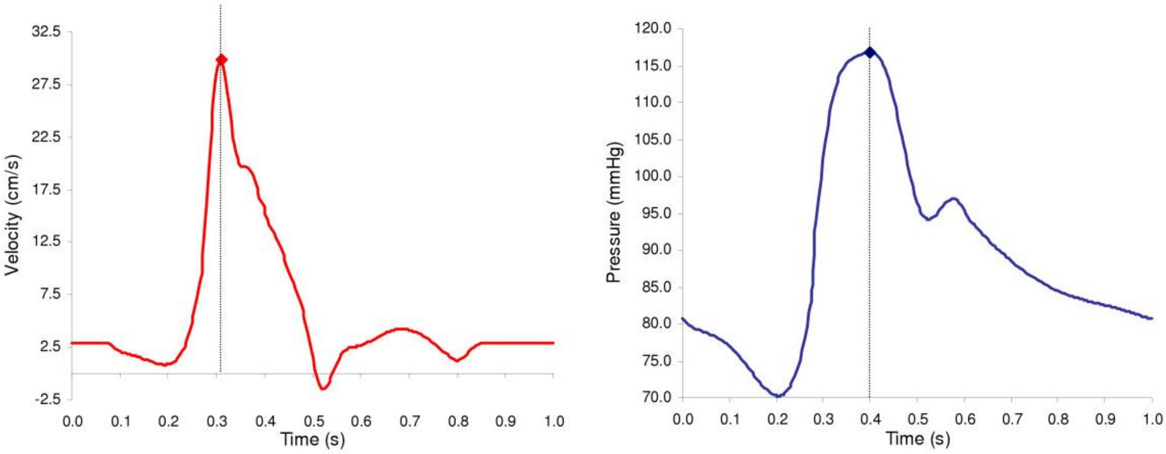

Figure 21 - Aortic flow waveform based on [94] used by [76]

Another popular waveform was derived using Magnetic Resonance Imaging velocimetry in an anatomically accurate physical model of the abdominal aorta. This work by Moore in 1994 showed a similarly smooth curve but with a less pronounced second pulse [95]. This waveform with a period of 0.9 seconds was used by Taylor with the addition of a particular spatial velocity distribution at the inlet [96].

In constant laminar flow within a straight pipe, the velocity will take a parabolic profile if given time to fully develop, this is known as Poiseuille flow. If, however, the flow is pulsatile, the inertial effects of the back-and-forth motion will cause the velocity profile to take on more complex shapes. The significance of this effect is quantified by the dimensionless Womersley number which is dependent on a length scale, frequency of pulsatility and kinematic viscosity [97]. In the aorta, the Womersley number is estimated to be 13.2, and it has been shown that changes in the Womersley number will alter the wall shear stresses found in simulations of blood flow in arteries [98]. While the use of Womersley profiles for inlet flow is clearly beneficial, it does add a layer of complexity to the simulation. Standard Womersley profiles exist for sinusoidally pulsatile flow, as shown in Figure 22 below, however for complex transient changes like in the Mills waveform, profiles would need to be calculated from the first principles of Womersley's work. Various papers claim to incorporate Womersley profiles into their inlet boundary conditions, however, details on how this is achieved were not provided in any of the reviewed literature.

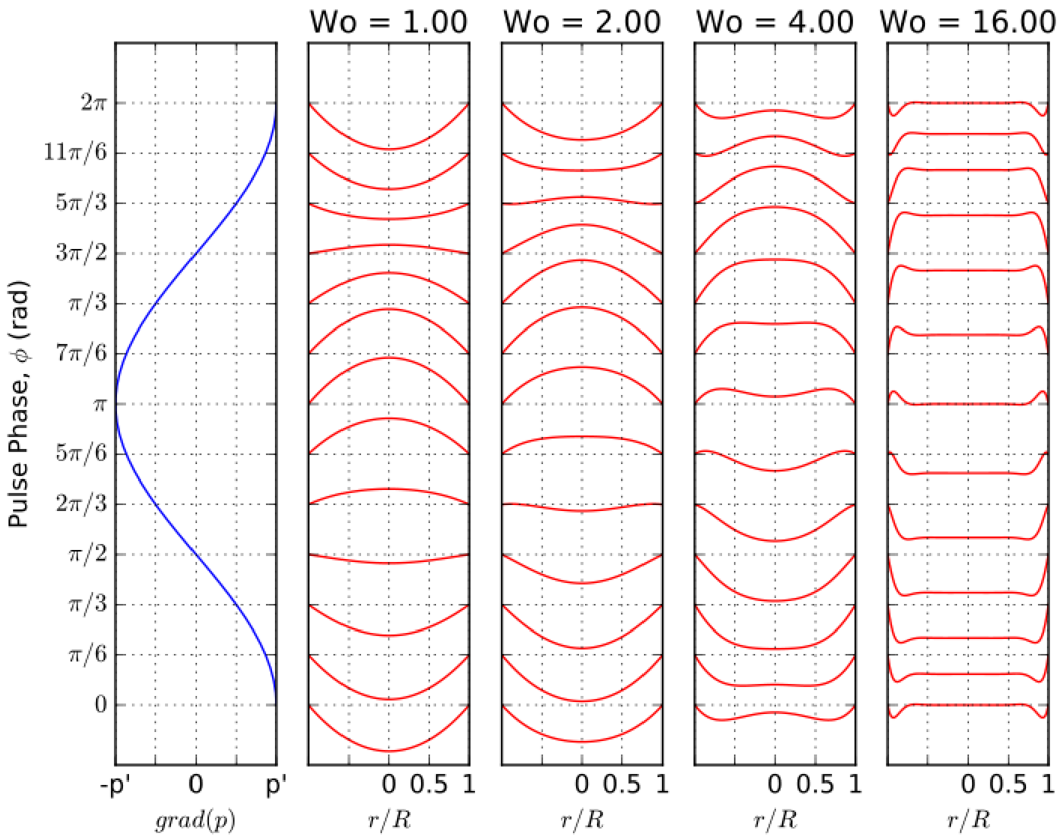

Figure 22 –Velocity profiles for sinusoidal waveform with varying Womersley number [99]

Recently, Phase Contrast Magnetic Resonance Imaging (PCMRI) has had a huge impact on blood flow rate measurement. This non-invasive technique has been developed to find blood flow rates in-vivo, with good temporal and spatial accuracy. The mechanism can be used to develop patient-specific flow waveforms for research and routine clinical applications [100]. Arzani used this method to find patient-specific flow rates in the descending aorta, and combined these with Womersley profiles to create the inlet boundary conditions for their model [2]. Callaghan used a similar approach to find flow waveforms for 6 healthy subjects [101] and Di Achille [4] used a waveform from Les [102] which has promise to be the replacement for Mills and Moore as the new standard for haemodynamic research in the aorta. The waveform presented by Les used PCMRI to find the average flow rate in the infrarenal and supraceliac aorta of 36 elderly patients with abdominal aortic aneurysms. Many previous studies were based on smaller groups of healthy individuals, so this work is especially valuable and apt for haemodynamic simulations of AAA. Average period of the waveform was 0.95 seconds.

1.9.6.2 Outlet boundary condition

Where the vessel wall is modelled as a flexible boundary, then the hydrostatic pressure of the fluid will change the stress on the wall and hence the shape of the flow domain [103]. Where multiple outlets exist, for example when including the minor arteries branching off the aorta, it is important to ensure that the model accurately captures the proportional split of blood flow to each branch [4]. In both these cases a methodology known as the Windkessel model is usually employed to represent flow impedance and reflected pressure waves from the downstream vasculature at the outlets. Where the boundaries are rigid and only one outlet exists, then the velocity field can be calculated accurately without the Windkessel model [104].

For simplicity, a constant pressure outlet condition is typically used. The value of this pressure is arbitrary, seeing as only the difference in pressure between inlet and outlet is relevant to the simulation. The combination of a specified velocity (transient or steady) at the inlet and zero pressure at the outlet is a very common way to set up the haemodynamic problem in simulations of blood flow in the aorta [47], [75], [76], [101].

2 Methodology

2.1 Mathematical Model

Given that this simulation deals only with the aorta, the scale of the flow domain is large enough to warrant the assumption of Newtonian behaviour for blood. The porosity of the thrombus was represented by altering permeability of computational cells within the clot by means of the k value un equation 2.1. The effect of including porosity fraction (also known as volume of fluid) is discussed on page 57. The entire simulation domain was treated as an incompressible fluid defined by the Navier-Stokes equations with the addition of the Brinkman term where necessary [88].

$$\frac{\delta(\rho\vec{v})}{\delta t} + \nabla \cdot (\rho\vec{v}\vec{v}) = -\nabla p + \nabla \cdot \vec{\tau} - \frac{\mu}{k}\,\vec{v} \tag{2.1}$$

$$\frac{\delta\rho}{\delta t} + \nabla \cdot (\rho\vec{v}) = 0 \tag{2.2}$$

$$\vec{v} = \mathrm{f(t)}\ |_{inlet} \quad ; \quad p = 0\ |_{outlet}$$

Where:
ρ is the density of the fluid, $\vec{v}$ is the velocity vector, p is pressure, $\vec{\tau}$ is the stress tensor, μ is viscosity, k is permeability and $f(t)$ is a function describing the pulsatile flow velocity of a heartbeat.

The enzymes thrombin, fibrinogen, and fibrin were treated as massless scalars within the fluid continuum. The transport of these substances was defined by the following equations:

$$\frac{\delta[\mathrm{Th}]}{\delta t} = \nabla(\vec{v} \cdot [Th]) + D_{th} \cdot \nabla^2[Th]\,; \qquad [Th] = f(t)\ in\ \Omega_A \tag{2.3}$$

$$\frac{\delta[\mathrm{Fg}]}{\delta t} = \nabla(\vec{v} \cdot [Fg]) + D_{Fg} \cdot \nabla^2[Fg] - S([Th],[Fg]) \tag{2.4}$$

$$\frac{\delta[\mathrm{Fn}]}{\delta t} = \nabla(\vec{v} \cdot [Fn]) + D_{Fn} \cdot \nabla^2[Fn] + S([Th],[Fg]) \tag{2.5}$$

Where:
$[Th]$ is the concentration of thrombin, $[Fg]$ is the concentration of fibrinogen, $[Fn]$ is the concentration of fibrin, $D_{[\;]}$ is the diffusion coefficient of each substance respectively, S represents the source function for Michaelis-Menten kinetics as shown in equation 1.4, and Ω_A represents the zone adjacent to the aneurysm bulge where thrombin concentration varies in time according to the function f.
These differential equations which govern fluid flow and scalar transport are discretised in the following way [105]:

- The flow domain is divided into discrete control volumes by using a computational grid or mesh. These control volumes may also be called cells.

- The governing equations are integrated over each individual control volume to construct algebraic equations for the discrete dependent variables (in this case pressure, velocity, and the scalar concentrations of thrombin, fibrin, and fibrinogen)
- Linearization of the discretised equations by means of second order upwinding for velocity and scalar concentration and second order spatial discretization for pressure.
- Second order implicit temporal discretisation to solve the linear equations at successive time steps

The finite volume method was used for the discretisation described above. A pressure-based solver was used with second order upwinding for momentum and first order upwinding for scalar transport.

2.2 Fluid Boundary Conditions

As discussed earlier, where the fluid flow domain is a rigid geometry with one inlet and one exit, it is appropriate to use boundary conditions of zero pressure at the outlet and a defined velocity or flow rate at the inlet. Including turbulence modelling would have been beneficial for accuracy and completeness, however, due to time and computational constraints it was omitted. Womersley profiles would have been another desirable addition for the inlet velocity profiles, but this was omitted in favour of a parabolic profile typical of fully developed steady-state laminar flow. This significantly simplified the model, and can be justified based on the observation that the flow velocity naturally develops into profiles resembling Womersley profiles over time. The inlet region is of sufficient length to allow the fluid to develop the characteristics of pulsatile flow which Womersley profiles aim to represent. In order to demonstrate this visually, the flow velocity profile was captured at the inlet and a surface just proximal to the aneurysm neck at three time points. These time points are 2.9, 3.13 and 3.34 seconds – corresponding with peak systole, reverse flow at late systole, and early diastole.

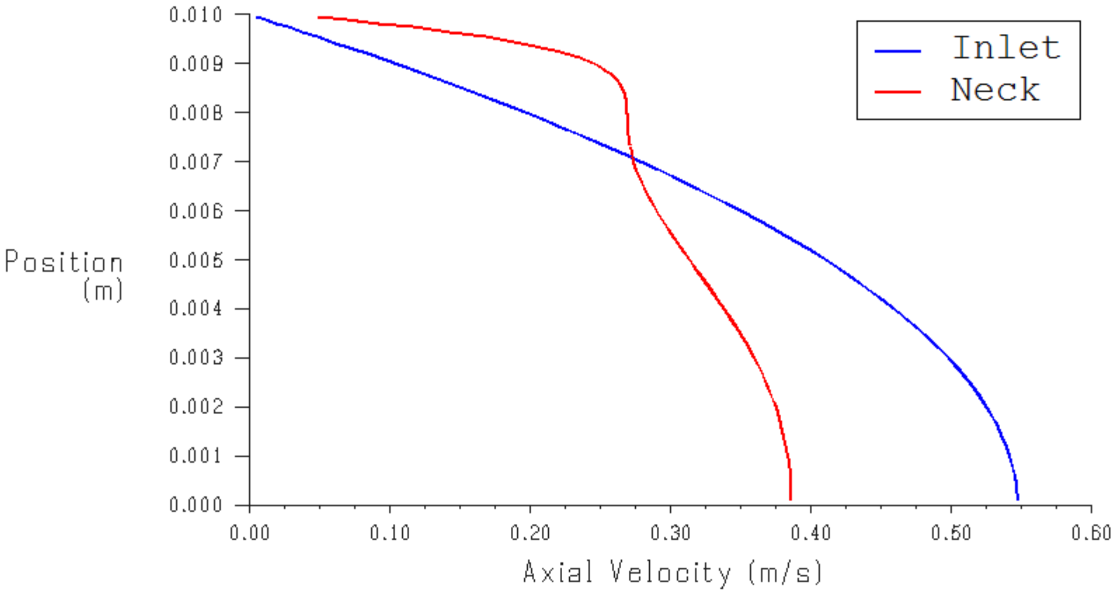

Figure 23 - Flow profiles at peak systole (2.9 sec)

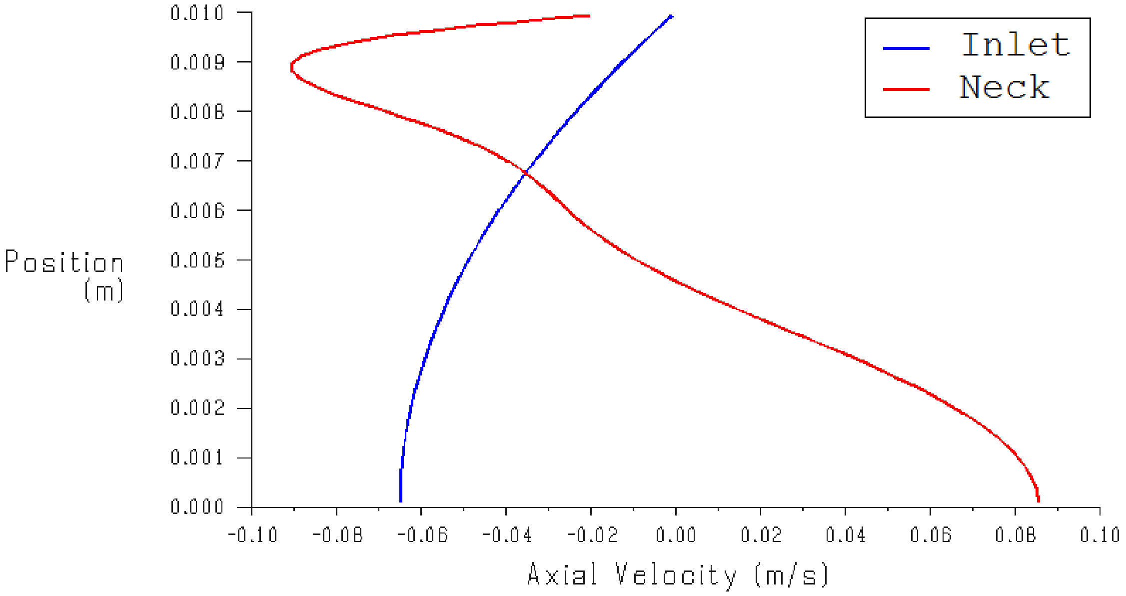

Figure 24 - Flow profiles at late systole (3.13 sec)

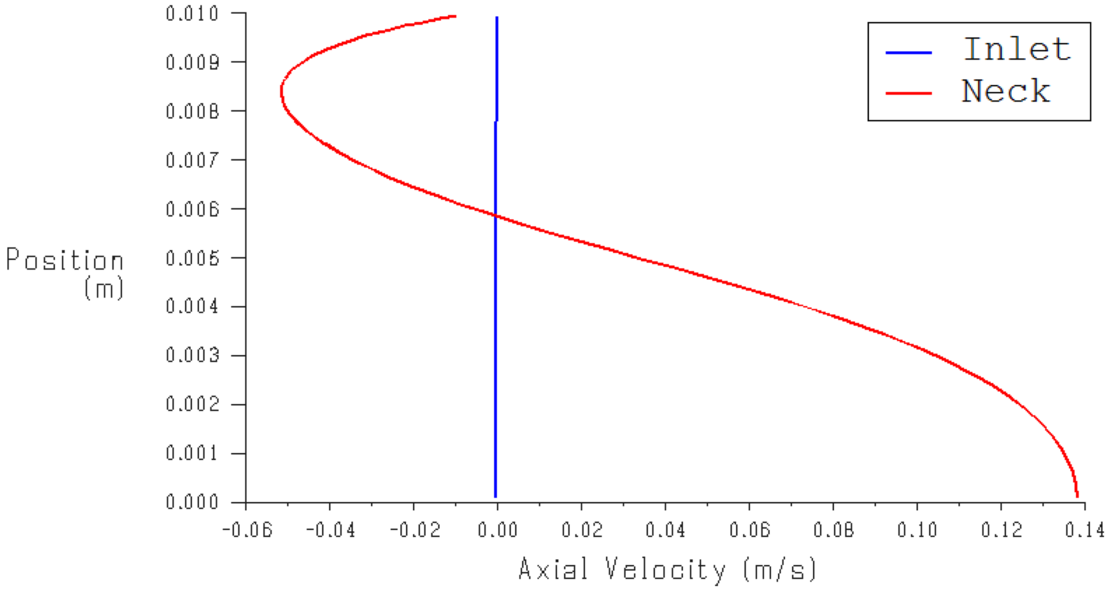

Figure 25 - Flow profiles at early diastole (3.34 sec)

Flow rate over time was taken from Les and is shown in below. The flow at the infrarenal section of the aorta was used, as this area is particularly prone to AAAs. This waveform has a maximum of 114 ml/s and a period of 0.95 seconds [102].

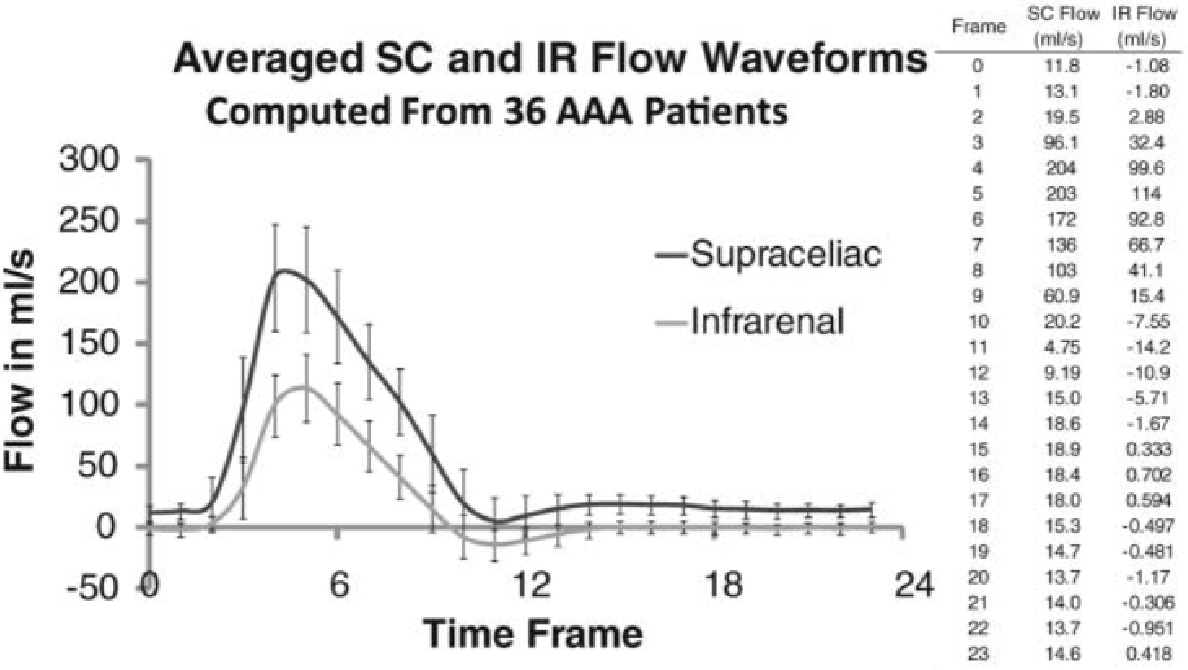

Frame	SC Flow (ml/s)	IR Flow (ml/s)
0	11.8	-1.08
1	13.1	-1.80
2	19.5	2.88
3	96.1	32.4
4	204	99.6
5	203	114
6	172	92.8
7	136	66.7
8	103	41.1
9	60.9	15.4
10	20.2	-7.55
11	4.75	-14.2
12	9.19	-10.9
13	15.0	-5.71
14	18.6	-1.67
15	18.9	0.333
16	18.4	0.702
17	18.0	0.594
18	15.3	-0.497
19	14.7	-0.481
20	13.7	-1.17
21	14.0	-0.306
22	13.7	-0.951
23	14.6	0.418

Figure 26 - Flow rate in the aorta during one heartbeat [102]

In order to use this experimental data in a numerical simulation, there are two possible strategies. The first is to use a table of values for flow rate at given times. The solver will use its current time to look up the nearest flow rate and time values, then interpolate from these to find a value for flow rate at that time step. The limitation of this method is that it does not lend itself to cyclic conditions. Flow rate and time values must be specified for the total duration of the simulation. Not only is this labour-intensive, but it cannot be run indefinitely. The second option is to convert the data for flow rate into a function with time as a variable and flow rate as the solution. This has the advantage of greater control over the outcome and no end-time limit on the simulation. Given that flow from the heart is periodic, Fourier series are commonly used to represent the waveform.

According to Les, their experimental waveform can be reduced to a 12 mode Fourier series, however, the details were not given in the paper [102]. An attempt was made using the multi-variable solver in Microsoft Excel to find the parameters for this series. The only constraint on this solver was to maintain an equal value at the beginning and end of the waveform to ensure continuity over multiple pulses. The goal was to minimise the L2 norm of the error between function and experimental results. After many iterations the resulting 12 mode Fourier series had an error value of 1.70%. The standard Fourier series takes the form shown in equation 2.6 below:

$$Q(t) = a_1 Sin(b_1 \cdot t + c_1) + \mathrm{a_2 Sin(b_2 \cdot t + c_2)} + .. + \mathrm{a_{12} Sin(b_{12} \cdot t + c_{12})} + \mathrm{d} \quad (2.6)$$

Optimised values for the series are shown in below:

	1	2	3	4	5	6	7	8	9	10	11	12
a	-0.003	0.384	-0.018	3.624	-0.562	-2.669	0.205	-2.771	-0.278	-0.397	0.384	0.939
b	0.034	1.750	1.061	0.767	44.88	20.49	8.394	21.15	17.85	23.32	43.58	44.39
c	-1.546	0.460	-0.522	1.328	-0.893	-8.287	0.278	-5.484	-3.962	-3.495	-9.533	-6.878
d	-3.809											

Table 2 - Coefficient values for 12 mode Fourier series representing pulsatile flow

Bearing in mind that this function will be solved each time step, it is vital to reduce computational expense if possible. This motivated an investigation into an alternative function which could accurately represent the experimental waveform more efficiently.

The first attempt was to remove the modes with minimal effect on the total series. These were those with a comparatively small a value such as modes 1 and 3. The next step was to multiply the whole series by an exponential function of the form $g(t) = a \cdot e^{b \cdot t + c}$. A negative value for b ensures that the role of this exponential function is to create larger amplitudes at the beginning of the waveform, and reduced amplitudes at the end of the waveform. Initially this produced good results: an error of just over 2% was achieved with only 4 modes. The problem with this method only became apparent during the mesh independence study. Fine meshes motivated the use of small time steps, but as time steps became smaller unusual flow spikes emerged within the first moments of the simulation. Some details of the waveform had been invisible in the excel analysis because the time resolution used for the curve fitting and waveform graph was too coarse. Only by monitoring velocity at each time step in the Fluent solver did the unwanted oscillations emerge.

Sharp changes in velocity over a few milliseconds are not desirable in a haemodynamic simulation because they generate sharp spikes in pressure and shear rate and may also slow or prevent convergence of the solver. The exponential function was causing an unwanted spike in the first few milliseconds of the waveform, so it was discarded in favour of non-exponential functions. A linear function showed some benefit, but a sinusoidal function showed the most promise. Ultimately the best performing function was a combination of the two, this function is shown in equation 2.7 below with variable values in :

$$Q(t) = (a_1 \cdot Sin(b_1 \cdot t + c_1) + \ldots + a_4 \cdot Sin(b_4 \cdot t + c_4) + d \cdot t + e) \cdot (a_5 \cdot Sin(b_5 \cdot t + c_5) + f \cdot t + g) \tag{2.7}$$

	1	2	3	4	5		d	-4.56441
a	8.09423	7.1611	-6.73674	-6.50845	-0.05959		e	3.89766
b	12.90847	13.75438	28.53115	28.92759	9.1563		f	-0.09942
c	-2.99266	-0.32451	-8.16715	-5.26343	-3.92483		g	0.03503

Table 3 – Coefficient values for custom pulsatile velocity function

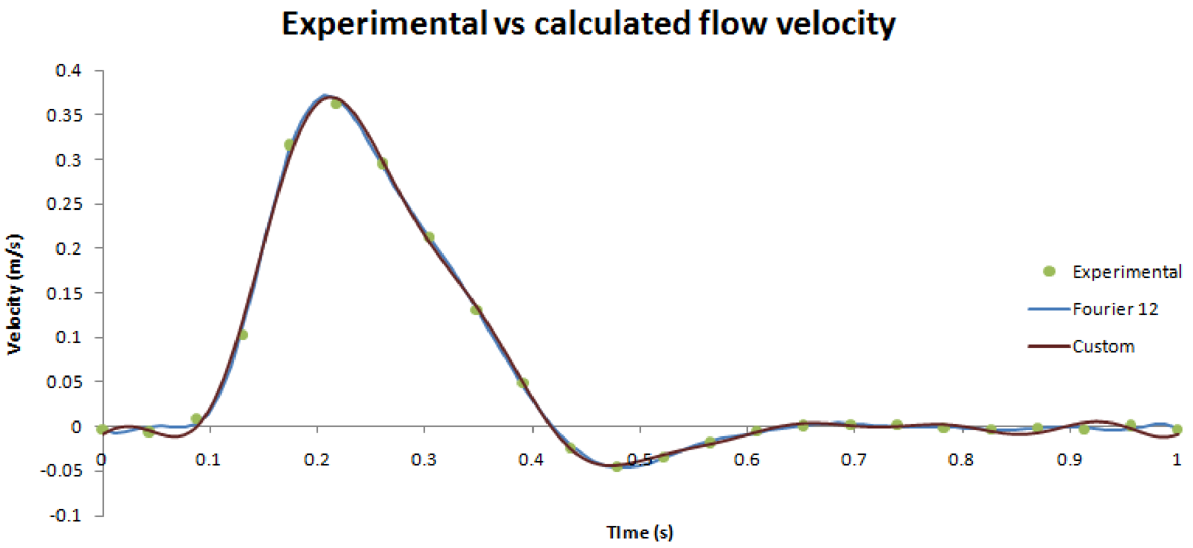

Figure 27 - Inlet flow waveforms based on experimental work and optimised functions

As seen in Figure 27 above, the custom function represents the experimental data closely. It has an error norm of 3.0% compared to the 1.7% of the 12 mode Fourier series. This value was deemed to be acceptable for the purposes of this simulation. Given that only 5 Sinusoidal functions are used rather than 12, this function is expected to be significantly faster to solve. The problematic effect of using this custom function is that special care must be taken with the input variable, namely flow time. A pure Fourier series would generate a cyclic output for indefinitely increasing time, however the custom function only generates an appropriate output for time values between 0 and 1. However, the limitation of the custom function can be treated in such a way that actually benefits the flexibility of the haemodynamic model.

The strategy is to convert the simulation flow time to a pseudo time between 0 and 1 and use this pseudo time in the custom function to calculate flow rate. This conversion is a surprisingly simple function that has the added benefit of introducing the variable of heart rate. The details of the function can be seen in the UDF section of the appendix, but essentially the wave form can be scaled horizontally to any length of time simply by changing one variable value. The value of this feature is that it allows the model to be quickly and easily adjusted for patient-specific heart rates. Even within the course of a simulation, the heart rate can be varied with negligible computational cost, opening up opportunities for investigation into the effect of heart rate on thrombus growth.

2.3 Chemical Boundary Conditions

Three chemical species were incorporated into the model as massless scalar quantities in the fluid continuum. These species were the glycoproteins fibrinogen, fibrin, and thrombin.

2.3.1 Fibrinogen

Fibrinogen is always present in the bloodstream at fairly high concentrations. A concentration of 7000 nM/l from Bodnar was used for this model [38]. The entire fluid domain was initialised with this concentration, and during the simulation the incoming fluid also has a Fibrinogen concentration of 7000 nM/L. The outlet is treated as a constant Dirichlet boundary condition with concentration of 7000 nM/L. Given that there is a brief period of reverse flow each heartbeat, the outlet will become the inlet momentarily and this fibrinogen concentration will propagate back into the flow field. The equal concentration at both outlet and inlet is based on the assumption that fibrinogen is not significantly depleted in the aneurysm region by the growth of a clot. Following some simulations with the full clotting model, the slow thrombus growth rate made it clear that this assumption is reasonable.

Fibrinogen was advected with the velocity field as a massless scalar. Fick's law was used to represent diffusion due to Brownian motion. The effect of hindered diffusion within the clot (as discusses in section 1.9.4.4) was neglected for the sake of computational simplicity. The diffusion coefficient for Fibrinogen in blood was either taken from Bodnar [38], as $D_{Fg} = 3.1\, E-7\; cm^2/s$, or the over-diffusive condition of $D_{Fg} = 10\; E-5\; cm^2/s$ from Biasetti [75]. The choice will be clarified in the results section. Reaction of fibrinogen proceeds according to Michaelis-Menten Kinetics, where the rate constants were taken from Bodnar [38] as $k_{cat} = 3450\; min^{-1}$ and $K_M = 3160\; nM$. Given that a fibrinogen molecule is converted directly to a fibrin molecule, the concentration of fibrinogen and fibrin should change by equal but inverse quantities. The formulas for the sink of fibrinogen and source of fibrin for a given computational cell are shown in equations 2.8 and 2.9 respectively below:

$$S_{Fg} = \frac{\delta[Fg]}{\delta t} = -3450 \cdot [Th] \cdot \frac{[Fg]}{3160+[Fg]} \tag{2.8}$$

$$S_{Fn} = \frac{\delta[Fn]}{\delta t} = +3450 \cdot [Th] \cdot \frac{[Fg]}{3160+[Fg]} \tag{2.9}$$

2.3.2 Fibrin

The initial concentration of fibrin in the entire domain is zero to represent a completely uncoagulated state. The function for the source of fibrin has been shown in equation 2.9 above. Diffusion is treated in the same way as fibrinogen with a diffusivity constant of either $D_{Fn} = 2.7\; E-7\; cm^2/s$ from Bodnar [38] or $D_{Fn} = 10E-5\; cm^2/s$ from Biasetti [75].

Convection is treated as a simple massless scalar in a fluid continuum. However, it should be noted that for fibrin specifically, this assumption represents a much greater simplification than for fibrinogen. While fibrin monomers are small enough to be washed along in the blood, they quickly polymerise into long chains and thick fibrils. These adhere to each other, platelets and endothelium to form resistant networks. When fibrin matures into a cross-linked mesh it has been found to resist high shear stress even in the absence of platelets. In this state, advection in the flow field and diffusion due to Brownian motion will reduce or totally cease. This implies that mature fibrin strands ought to be treated differently from free fibrin monomers. For the sake of simplicity though, this model treats all fibrin as unbound monomers. The increased viscous resistance of the thrombus (described in the chapter on permeability on page 57) could be considered a proxy for the fibrin polymerisation and cross-linking effects, as it will significantly reduce the flow velocity within the thrombus, and hence hinder the convection of fibrin.

2.3.3 Thrombin

As mentioned earlier, most recent computational models of Thrombosis have modelled the entire coagulation cascade as a collection of reactions with all the procoagulant and anticoagulant enzymes involved [37], [75], [85]. It is necessary to specify starting concentrations and reaction rates for every substance and interaction, and when platelets in multiple stages of activation are included - the biochemistry can become quite complex and expensive to simulate. These concentrations and rate constants are typically based on population averages, so to tailor the model to a specific patient would require re-evaluation of some or all of these values. The testing necessary to achieve this seems to be prohibitively complex or impractical, as it has not been attempted or suggested in any of the reviewed literature. The model presented in this thesis uses a novel alternative approach to thrombin generation which would allow important features of patient-specific blood chemistry to be simulated with relative ease.

The strategy is to simplify a thrombin generation curve from a CAT test for the patient in question to an explicit function in time. Hemker and Wagenvoord have developed an analytical function which can represent a patient-specific TG curve to high accuracy and contains only 3 variables. These variables are peak thrombin concentration (PEAK), time to peak concentration (TTP), and endogenous thrombin potential (ETP) - which is the total quantity of thrombin produced or the area under the TG curve. This function for thrombin concentration over time is used as replacement or proxy for the biochemical model of the coagulation cascade. This approach makes patient-specific coagulation modelling significantly easier from a biochemical perspective because a blood test can reveal the three variables required to describe the evolution of thrombin production. It may also be more accurate than previous methods, as the thrombin generation is observed experimentally rather than simulated.

The function to analytically describe the time course of thrombin concentration in a TG test was published as follows (copied by screen grab from the text) [106]:

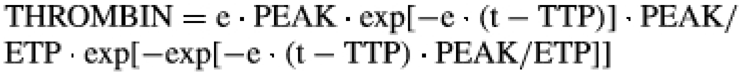

$$\mathrm{THROMBIN} = e \cdot \mathrm{PEAK} \cdot \exp[-e \cdot (t - \mathrm{TTP})] \cdot \mathrm{PEAK}/\mathrm{ETP} \cdot \exp[-\exp[-e \cdot (t - \mathrm{TTP}) \cdot \mathrm{PEAK}/\mathrm{ETP}]] \tag{2.10}$$

After careful analysis, it was found that equation 2.10 does not produce a TG curve with the appropriate shape. One would expect that if the ‘PEAK’ variable is 100nM/L then the maximum of the resulting function would be 100, the same for TTP and ETP. This, however, is not the case, so some modification is called for. Moving the second closing bracket to after the ETP term caused it to work perfectly, so presumably the function was meant to be in this form but was mis-typed. below summarizes the results of the original function and the function with modified brackets.

Table 4 - Results of modification to TG curve equation

	Input 1	Original (eqn 2.10)	Modified (eqn 2.11)	Input 2	Original (eqn 2.10)	Modified (eqn 2.11)
PEAK	367	26996	368	128	1361	128
TTP	6.3	2.16	6.32	4	1.12	4.00
ETP	2277	62554	2228	633	2706	631

The values for input 1 came from Wu [70] and the values for Input 2 came from Ninivaggi [61] with TTP added. Based on these results, it can be concluded that the function as published was accidentally mis-typed, and that the bracket should be moved to its correct place. The modified function is as follows:

$$THROMBIN \;= e \;\cdot PEAK \;\cdot \exp\left[-e\cdot(t-TTP)\cdot\frac{PEAK}{ETP}\right]\cdot exp[-exp[-e\cdot(t-TTP)\cdot PEAK/ETP]] \qquad (2.11)$$

The values available for peak, ETP and TTP vary widely in the literature. The decision was made to use data that is both recent and originates from Dr Hemker's research group at Maastricht University. An added advantage of these values is the short clotting time which fortunately reduced the total simulation time to manageable levels. The values from Bloemen [107] are shown in Table 5, along with the TG curve based on the modified formula in Figure 28.

Table 5 - Values used in Equation 2.11 to generate TG curve

ETP (nM · min)	Peak (nM)	Time-to-peak (min)
1169.0	264.1	3.0

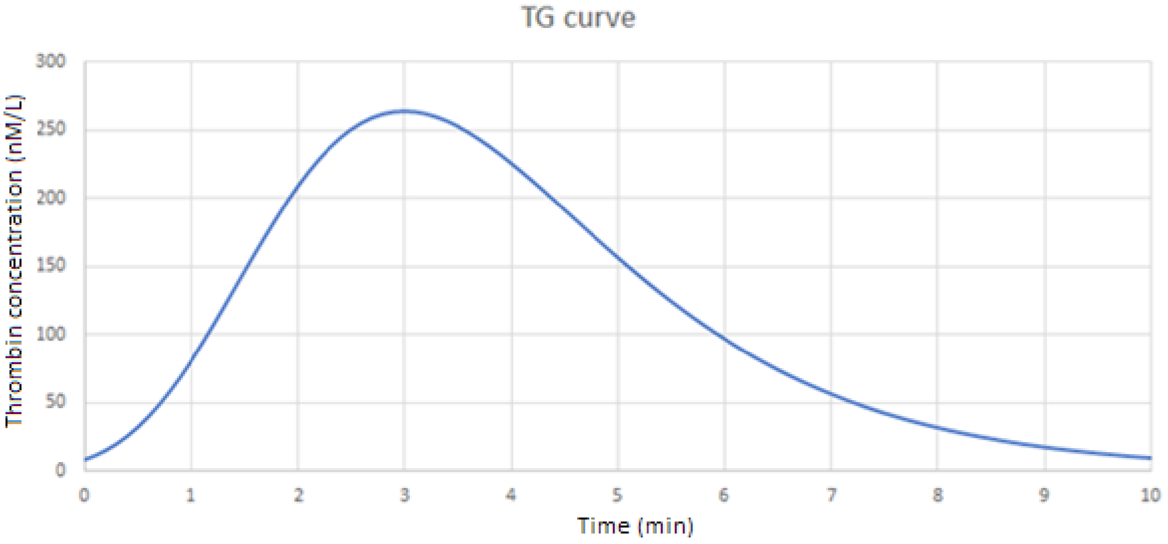

Figure 28 - Thrombin concentration curve based on equation 2.11 and parameters from Bloemen 2018

The challenge of this approach, however, is in the spatial complexity of applying this thrombin concentration function. In models which simulate the coagulation cascade this was not a problem because thrombin generation rate was calculated for every computational cell at every time step based on the presence of other substances. As these other substances are unevenly distributed, a region of thrombin generation will emerge only where sufficient chemical precursors are present. For example, Leiderman and Fogelson [60] created a model where thrombin can only be generated in the presence of sufficient prothrombin and prothrombinase. Prothrombinase was abundant within the clot and prothrombin was abundant in the flowing blood, so the region of overlap was found to be a narrow band at the edge of the clot. Dashkevich [32] showed that blood plasma is an excitable medium in which thrombin generation can vary in space and time. In quiescent plasma the region of peak thrombin generation started at a TF coated surface then propagated out into the fluid like a wave. Both these studies show that the region of thrombin generation is a significant consideration in a biochemical model of thrombosis.

CAT tests are done in a laboratory with a sample of stationary blood, so they represent the average values in the fluid as a whole. While they capture the temporal development of the coagulation biochemistry, they do not capture any spatial information. So in order to use the TG curve in a thrombosis model some assumptions must be made about the location of thrombin generation.

One possibility is to specify the flux or concentration of thrombin at a boundary. Biasetti [75] took this approach with a fixed concentration of tissue factor at the aneurysm wall. Given that the output of a CAT test is static thrombin concentration over time, the flux boundary option was dismissed in favour of specifying the concentration of thrombin. The boundary corresponding to the concave region of the aneurysm bulge was selected as the site of thrombin concentration. The same region was used by Biasetti and can be thought of as the region where the endothelium is most damaged.

This approach did not produce any blood clot in the simulation, and even when thrombin was maintained at its peak value for close to a minute, there was little or no transport of thrombin into the blood. The reason for this is most likely because the no slip condition ensures that velocity is zero and advection is negligible at this boundary, so the only mechanism driving thrombin into the fluid domain is diffusion. Even when higher diffusivity was used for thrombin in blood based on Biasetti’s over-diffusive values, it was not sufficient to generate a thrombus in reasonable time.

The model was then modified to specify thrombin concentration in the first layer of cells adjacent to the endothelium of the aneurysm bulge. These cells, though only 0.04mm thick, experience the effect of convection as fluid flows through them. This in turn transports the thrombin more effectively away from the wall than pure diffusion. The result was noticeably faster thrombus growth and more widespread thrombin transport.

The choice of locating the region of thrombin concentration at the aneurysm boundary will have various consequences for the thrombus growth over time. Hindered transport (applied to convection or diffusion) is a necessary feature of a thrombosis model, however it also means that as the clot grows, transport from the region of high thrombin to the growing edge of the thrombus will become more difficult. As the thrombus boundary moves further away from the endothelium one would expect to see thrombin concentration reduce and hence clot growth could slow or cease. This implies that the ultimate size and shape of the clot could be limited by the distribution and transport of thrombin. This mechanism of self-limitation has a basis in the literature [84], so this modelling strategy provides a means to investigate this phenomenon. This approach to the location of thrombin generation shall be called Strategy A in the results section.

An alternative strategy, based on the findings of Leiderman and Fogelson [60], is to site the region of peak thrombin generation in a narrow band at the outer edge of the thrombus. This strategy would totally negate the effects of hindered transport within the thrombus, hence the self-limiting mechanism described above would no longer come into play. The availability of thrombin at the growing edge of the thrombus is expected to increase the speed of growth, and increase the effects of advection on thrombin and fibrin distribution.

With this strategy, one likely limitation on thrombus growth will be the reducing thrombin generation due to the TG curve, however this would only occur in the later part of the simulation. The only mechanism which will limit clot growth within the first few minutes is mechanical lysis. This strategy was implemented by specifying thrombin concentration (based on the TG curve) within the cells representing the shell and deposited platelets.

The details of this method to localise thrombin generation are as follows. The thrombus region has three distinct zones, namely the bound platelet layer, shell and core. The bound platelet layer is always one computational cell thick and covers those areas of the thrombus boundary where shear stress is low, the shell is any region where fibrin concentration exceeds 600 nM/L but is less than the concentration necessary to be part of the core. This particular value of fibrin concentration which separates core from shell has not been discussed in the reviewed literature, so various values were tested in order to find one which would produce a shell of appropriate thickness. This concentration value shall be known as the boundary fibrin concentration (BFC) from now on. All computational cells which are designated as shell or platelet layer can generate thrombin. Generation is represented by finding the concentration of thrombin from the TG curve corresponding to the elapsed flow time, and applying it to all ‘thrombin generating’ cells at the end of each time step. Diffusivity of Thrombin is either 6.47 E-7 cm2/s from Bodnar [38] or 10 E -5 from Biasetti [75]. This thrombin methodology shall be called strategy B.

2.4 Software

The Ansys workbench suite of programs was used exclusively for this project. Space Claim was used to create the geometry, Mechanical for meshing, and Fluent 19.2 for simulation, compilation of user defined functions (UDFs), data output and visualisation of results. Initial simulations were done on a 4 core desktop PC, however, final simulations were run on the Lengau cluster at the Centre for high performance computing (CHPC) in Cape Town. A 24 core compute node was used with remote visualisation of the Fluent user interface by means of a VNC client and SSH tunnelling. The simulation time was dramatically reduced by using the CHPC rather than the desktop PC, however, an actual value for speed-up was not calculated. A 9-hour simulation would cover 1 to 3 minutes of blood flow time depending on the various features of the model or time step strategy.

2.5 Meshing

The 2D axisymmetric geometry from Biasetti was used as the fluid flow domain. In that model, a mesh of 58 194 triangular elements was used with an element quality greater than 0.81. The mesh was refined near the blood vessel boundary with gradually decreasing cell size. Unfortunately no data is given on element sizing [75].

For the fluid model presented here, a different meshing strategy was employed. Firstly rectangular elements were preferred over triangular ones for the following reasons:

- The Fluent meshing guide recommends the use of triangles in 2D and tetrahedrons in 3D only for complex geometry. For simple geometry, rectangles or hexahedrons are expected to be quicker and more accurate [108]. The fusiform aneurysm geometry is simple enough for rectangular elements to be the more appropriate choice.

- A clotting simulation was carried out with both element types, and the triangular cells proved problematic for implementing the moving boundary method which represents thrombus growth and lysis. Some cells experienced unusually high or low shear stress which made the transition from thrombus to blood or vice versa unpredictable.

- Rectangular cells have corners which are less sharp, and this was preferable for representing the smooth surface of the thrombus boundary. By the same logic, polygon cells would be even better, but these were not available in the meshing software used.

All meshes incorporated inflation at the interface between a stationary boundary and the moving fluid. This inflation was based on a first layer in the order of 0.04-0.1 mm and a growth rate of 1.2 for 7 layers. Local refinement was implemented along the boundary of the aneurysm bulge where the thrombus will begin to grow. High mesh resolution is desirable in this region to capture the details of the irregular thrombus geometry. Further local refinement was considered necessary at the aneurysm neck due to high shear stress and rotational flow in this region.

Figure 29 shows a detailed view of the mesh at the boundary in the centre of the aneurysm sac. The inflation layer is visible at the top edge, followed by a region of local refinement which gradually expands to the regular cell size. While the mesh is quadrilateral dominant, some triangles are included in order to improve overall cell orthogonality.

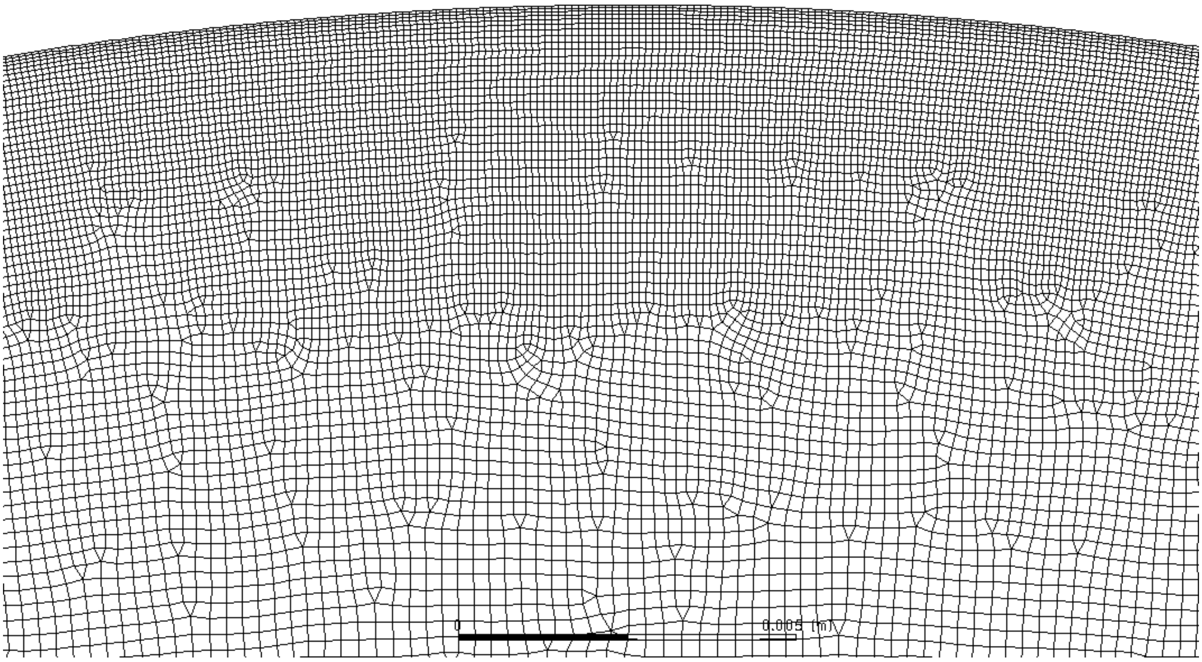

Figure 29 - Detailed view of mesh at aneurysm wall

2.6 Solver Parameters

Ansys Fluent 19.2 offers four options for solving the pressure and velocity terms of the discretized Navier-Stokes equations. These are called SIMPLE, SIMPLEC, PISO, and Coupled. SIMPLE is the default, however for transient flow simulations the PISO scheme is recommended by the developers [109]. This was tested with the Biasetti geometry, a time step of 0.002 seconds, a maximum cell edge size of 1mm and a pulsatile inlet flow. The maximum Courant number for this particular simulation was close to 1. The time taken to complete 25 time steps is shown in Table 6 below.

Method	SIMPLE	SIMPLEC	PISO	Coupled
Run time (sec)	72	71	62	61

Table 6 - Speed of pressure & velocity solution methods

Clearly PISO and Coupled are closely matched, so various other parameters were adjusted for these two methods to see the results. Higher order term relaxation was applied to the calculation of all variables with a relaxation factor of 0.75. The results are shown in Table 7 below.

PISO	Coupled
61 seconds	60 seconds

Table 7 - Effect of relaxation factor on speed

Higher order term relaxation offers a small speed up, so it will be incorporated into future calculations. The difference between the Coupled and PISO solvers is small enough to be negligible, so initially the decision to go with PISO was made on the basis of the recommendation by the software developers. However, after further investigation of sensitivity to time-step size, that decision was reversed. More details on this in the next section.

For the spatial discretisation of pressure, the solver offers four options. ANSYS documentation recommends the PRESTO! for incompressible flows with small body forces and porous zones [109]. This description closely matches that of the haemodynamic model used in this simulation. A timing test was done for 50 time steps, and the results in Table 9 show that PRESTO! is the fastest. Given that PRESTO! is recommended and shows good speed, it will be used for all future calculations.

Pressure discretisation	Standard	Second order	PRESTO!	Linear
Run time (sec)	129	124	120	124

Table 8 - Speed of pressure discretisation methods

2.7 Grid Independence Study

The purpose of a grid independence study is to minimise the error due to the discretization of the flow domain into small computational cells. Meshes of various refinement were generated and used to simulate an identical fluid problem. The problem was purely haemodynamic, with no porous zones or chemical transport. Two seconds of pulsatile flow were simulated using identical time steps. At the end of this time, variables describing haemodynamic features relevant to clotting were recorded. These variables are described below.

1. Average shear stress over the entire concave surface of the aneurysm bulge
2. Average strain rate over the entire concave surface of the aneurysm bulge
3. Velocity at a point located within the distal region of the aneurysm bulge, roughly 8mm away from the vessel wall
4. Maximum velocity anywhere in the fluid domain

The original values for a coarse mesh, followed by the relative difference between the values of subsequent more refined meshes are shown in Table 9 below.

Number of cells	1. Average shear stress	2. Average strain rate	3. Velocity at point	4. Maximum velocity
15000	0.0638 Pa	22.2 s^-1	0.0170 m/s	0.136 m/s
Relative change				
26000	14.97%	12.43%	-0.20%	7.00%
48000	-1.01%	0.92%	5.14%	0.55%
88000	-0.36%	-0.38%	0.17%	-0.02%

Table 9 - Results of mesh independence study

Typically the mesh is refined by a factor of 2 at each step, and a change of less than 2-5% between successive mesh refinements is considered sufficient for convergence [110]. However, doubling the number of cells is a large change, and can lead to unnecessarily fine meshes. A mesh is too fine if it slows computation time significantly in return for negligible improvements in accuracy. As seen above, the 48 000 cell mesh does not quite meet the 5% relative change criteria, but the 88 000 cell mesh is too fine with less than half a percent improvement in accuracy. In order to find the optimum refinement, three meshes with cell counts between 48 000 and 88 000 were generated. Graphs showing the results of all the tested meshes are presented in Figure 30 below.

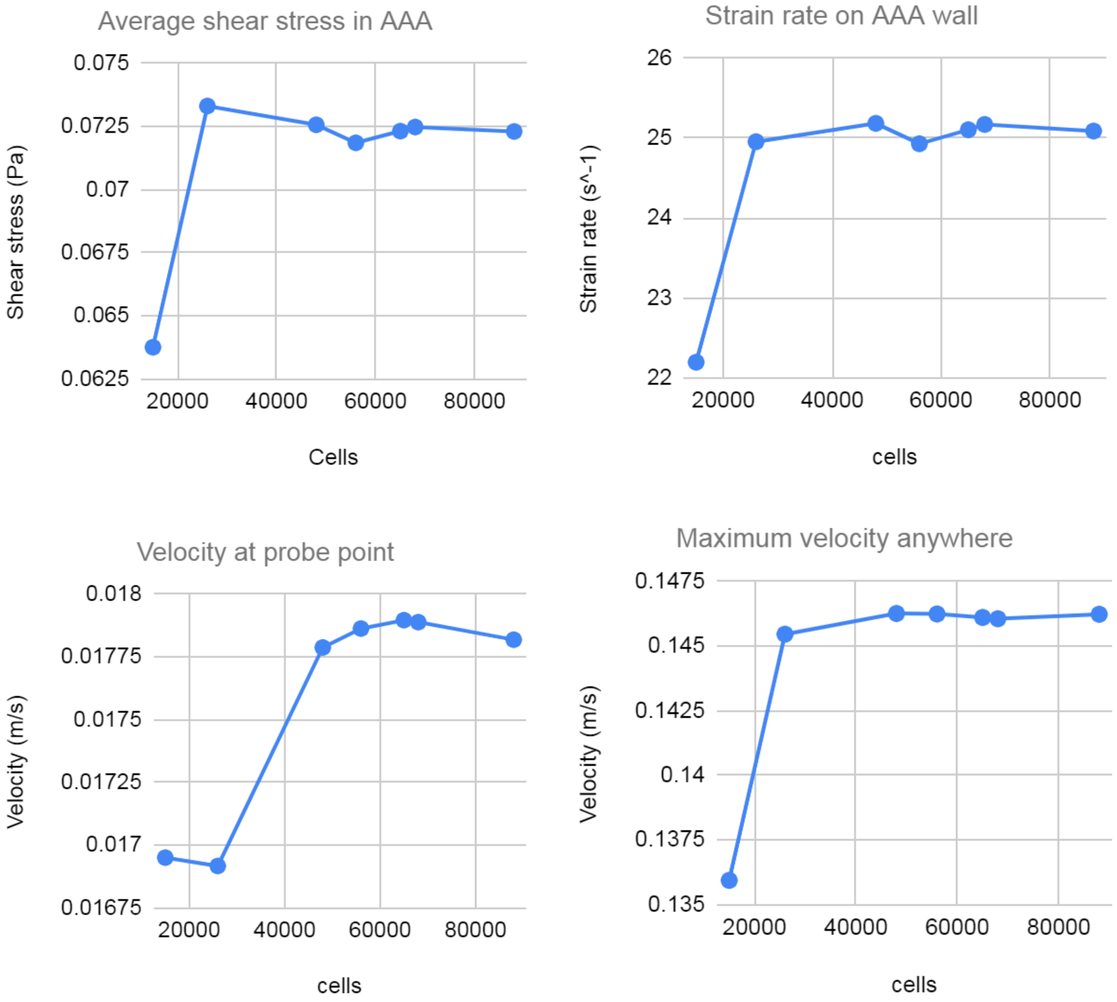

Figure 30 - Response of key haemodynamic variables to mesh refinement

From visual inspection it appears that anything above 60 000 cells is sufficient to guarantee mesh independence. A mesh of 64 000 cells was used for all future simulations. Detailed images of the mesh are shown in Figure 31 and Figure 32 below:

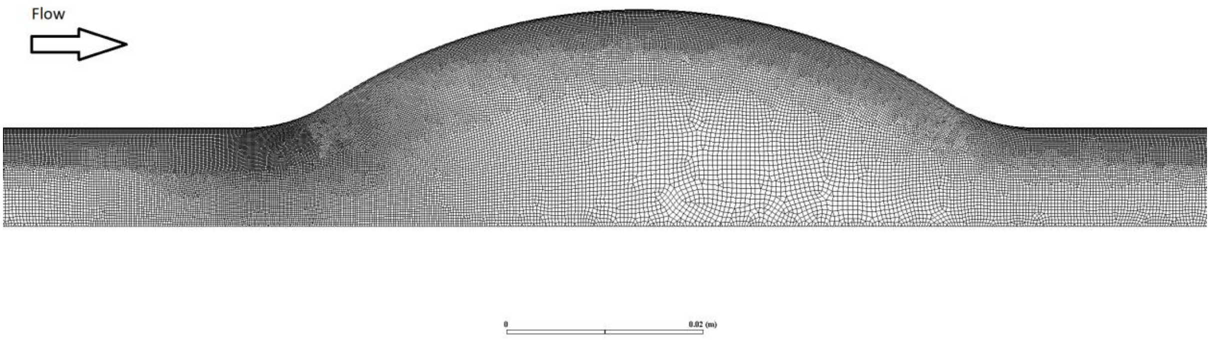

Figure 31 - Overall view of mesh with 64 000 cells

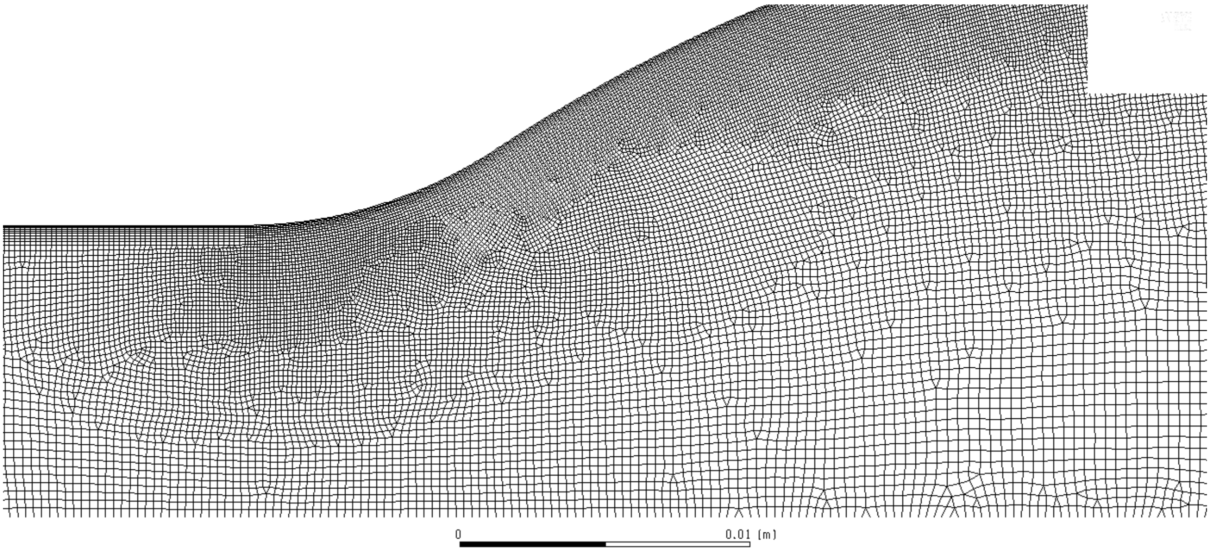

Figure 32 - Close up view of mesh at aneurysm neck

The standard mesh report from ANSYS fluent is as follows:

Minimum Orthogonal Quality = 7.65989e-01; Maximum Aspect Ratio = 3.51811e+00

To gain more insight into the quality of the mesh, histograms for various cell quality metrics were generated in ANSYS Mechanical. These metrics are orthogonality, aspect ratio, skewness and finally overall quality. The histograms for the 64 000 cell mesh appear below:

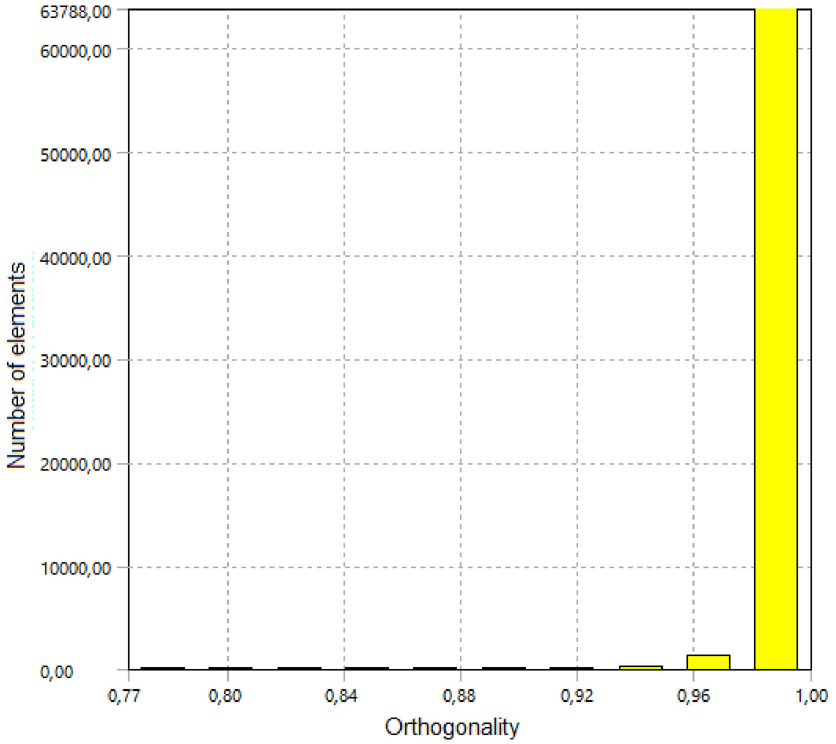

Figure 33 - Histogram of cell orthogonality in final mesh

As seen in Figure 33, Cell orthogonality is good. Figure 34 shows that most cells have close to perfect aspect ratio. However, cells in the inflation layer are thin in the radial direction compared to the axial. This leads to some aspect ratios up to 3. Given that these cells typically experience flow oriented to the longitudinal axis of the cells, this aspect ratio issue was considered insignificant.

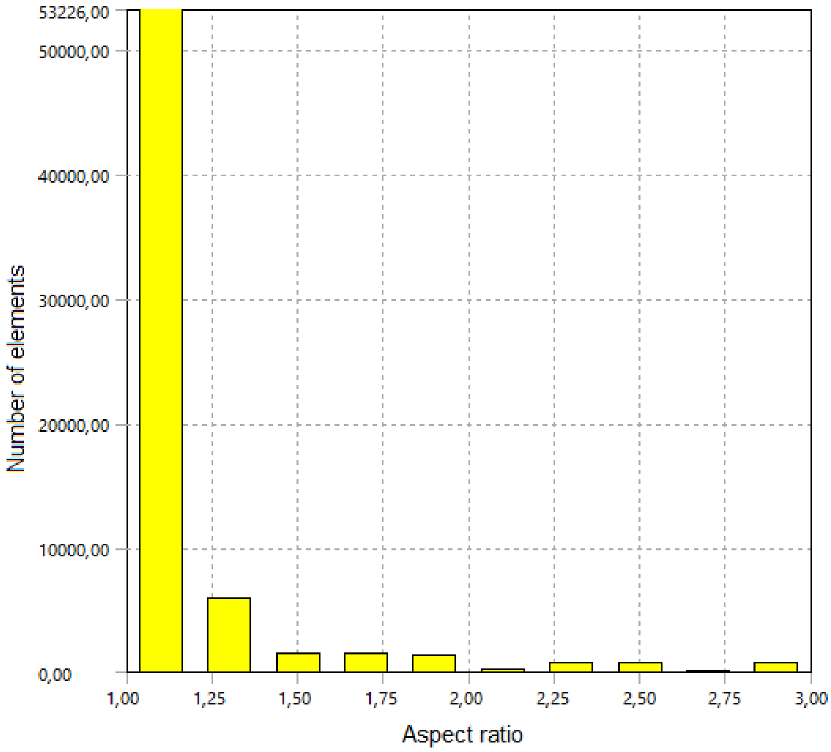

Figure 34 - Histogram of cell aspect ratio in final mesh

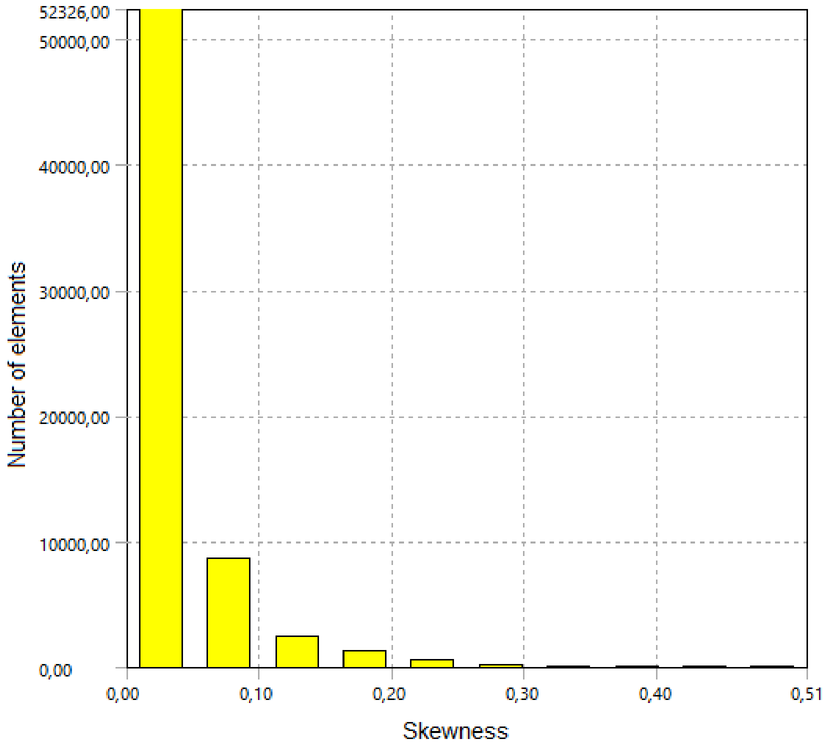

Figure 35 - Histogram of cell skewness in final mesh

Figure 35 shows that cells skewness is generally low and within reasonable bounds. Figure 36 shows that the great majority of cells have a quality above 0.9, however, there are some of lower quality, most likely due to the aspect ratio imbalance mentioned above. Overall the mesh quality metrics show that the mesh is of a good standard and suitable for use in the fluid solver.

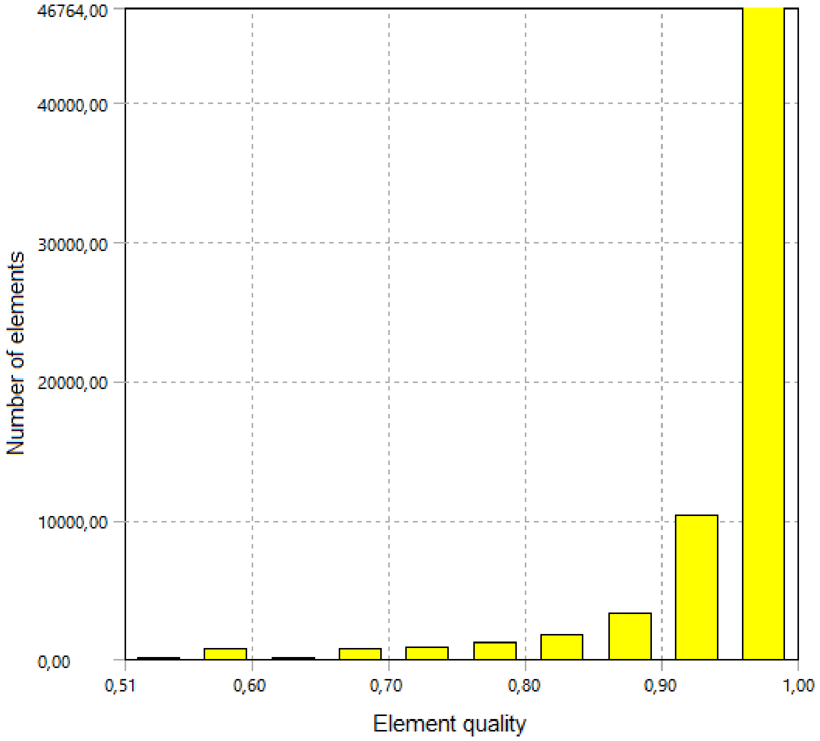

Figure 36 - Histogram of overall cell quality in final mesh

2.8 CFL Condition and Time Step Size

The Courant-Friedrichs-Lewy (CFL) condition describes the maximum Courant number which a time stepping numerical method can use. The Courant number is a measurement of how much information traverses a computational cell in a given time, so in fluid dynamics this translates to flow velocity multiplied by time step size divided by the length of the cell. The purpose of checking the CFL condition for a given simulation is to find an appropriate time step size which is small enough to ensure convergence and accuracy, but not so small that the simulation takes longer than necessary. Speaking of higher or lower Courant numbers is analogous to using longer or shorter time steps [111].

For explicit schemes, a CFL<1 is a necessary condition for stability, however, the solvers used in ANSYS Fluent are implicit and therefore from a mathematical perspective are unconditionally stable. In reality though, computational limitations and non-linearities in the governing equations can lead to inaccuracy and instability if the time steps are too large. The question of “how large is too large” is not simple to answer, as the appropriate time step size is dependent on the nature of the problem being solved. In ANSYS Fluent the default Courant number for the coupled solver is 5, however, numbers above 100 are possible for certain situations [109]. No CFL condition is recommended for the PISO method in the literature, but when a Courant number above 2 was used to simulate a flow with a porous zone the solver quickly diverged. The coupled solver did not diverge even at much higher Courant numbers therefore this was the preferred discretisation method for future simulations.

An additional topic in the search for computational speed and accuracy is matrix preconditioning and stabilization. Two of the most popular methods which are available in Fluent are BCGSTAB and GMRES. These methods improve the conditioning of the matrices used in the linear solver, the result being more stable with potentially faster convergence [112]. Some experiments were conducted to find the effects of these methods versus the standard coupled solver.

One systolic pulse was simulated in the geometry from Biasetti [75] using the coupled solver and varying timestep sizes. No porous zone was present in this case. The values for various flow variables were recorded throughout the simulation. The L_2 norm technique was used to reduce this time series to a single value for comparison. A solution with no stabilisation and a Courant number below 1 was used as the benchmark from which to test the accuracy and speed of other solutions. Where percentages are shown, these represent the variation from the benchmark. Speed-up is a dimensionless factor found by dividing the benchmark computational time by the new computational time.

Courant number	Stabilisation	Average velocity	Strain rate	Velocity at test point	Speed-up
1	None	-	-	-	None
2	None	0.05917%	0.33276%	0.19772%	2.07
	BCGSTAB	0.05917%	0.33276%	0.19772%	1.78
	GMRES	0.05917%	0.33276%	0.19772%	1.23
5	None	0.72958%	1.13593%	0.89934%	5.21
	BCGSTAB	0.68296%	0.96732%	0.79049%	4.39
	GMRES	0.67983%	1.13595%	0.89934%	3.67
10	None	1.29547%	2.30860%	1.82259%	10.54
	BCGSTAB	0.73662%	1.35198%	1.00335%	8.67
	GMRES	1.29547%	1.15826%	1.82265%	6.07
20	None	1.28031%	2.43038%	1.86963%	23.28
	BCGSTAB	1.28032%	2.43030%	1.86957%	19.95
	GMRES	1.28031%	1.44926%	1.86959%	14.32

Table 10 - Effect of Courant number on simulation accuracy and speed

When standard averaging was used rather than an L2 norm, errors were all below 1.5%. A comparison of peak values of each variable showed errors all below 0.2%. The results in Table 10 show that even with a Courant number of 20, results can differ less than 2% from a Courant number of 1. Considering the significant speed up obtained by larger time steps, an argument can be made that this small reduction in accuracy is an acceptable price to pay.

Regarding stabilisation techniques, in this case they usually provided a minor improvement in accuracy for a minor cost in simulation time. BCGSTAB is consistently faster than GMRES, but accuracy shows no such consistent trend. When a porous zone was added to the flow domain in a later experiment, the effects of BCGSTAB versus no stabilisation were compared by observing the real time plot of residuals in the Fluent solver. The standard solver converges quickly initially, but slows exponentially with each iteration. When BCGSTAB is activated the residuals reduce rapidly and linearly, resulting in significantly faster convergence. This motivated the use of BCGSTAB for all future simulations.

Unfortunately, the concept of a CFL condition becomes less useful and clear when considering a mesh with a wide range of cell sizes and a flow with unsteady velocity. The "worst case scenario" method would be to use the maximum velocity at any space and time, and the length of the smallest cell in the mesh. While this method was used in the previous time step analysis, it is worth remembering that this number may be unreasonably inflated due to the underlying assumptions. Two arguments against the use of this worst-case approach are described below.

The first issue is the common practice of using inflation layers for extra cell refinement near stationary walls. The purpose of this refinement is to capture the high shear gradients caused by a viscous fluid flowing past a stationary surface. Assuming a no-slip condition at the boundary means that flow velocity approaches zero in the same region where cell sizes are becoming smaller. This means that the smallest cells will typically experience the lowest velocities, and larger cells in the centre of the domain will experience higher velocities. Generally this should lead to fairly consistent Courant numbers far below the worst-case scenario estimate.

Another complication for analysis of Courant number is the pulsatile flow generated by the heartbeat. Inlet flow velocity is close to zero for much of the waveform and peaks only for an instant. If one selects a time step based on the Courant numbers at peak systole, it would be far too conservative for the diastolic period. Larger time steps during diastole are desirable in order to reduce overall simulation time.

The strategy employed was to calculate the Courant number in every cell for various time step sizes and various flow rates. Four heartbeats were simulated to stabilise the flow field, then on the fifth beat, histograms were generated to illustrate the number of cells within a certain range of Courant number. Three points in time were selected for analysis, firstly maximum flow rate at peak systole, secondly a medium flow rate immediately after systole, and finally a low flow rate at late diastole. Time step size was varied at each of these moments with the aim to keep the Courant number below 3 in the majority of computational cells. The points of investigation and time step sizes are shown in Figure 37 followed by histograms of Courant numbers in each cell.

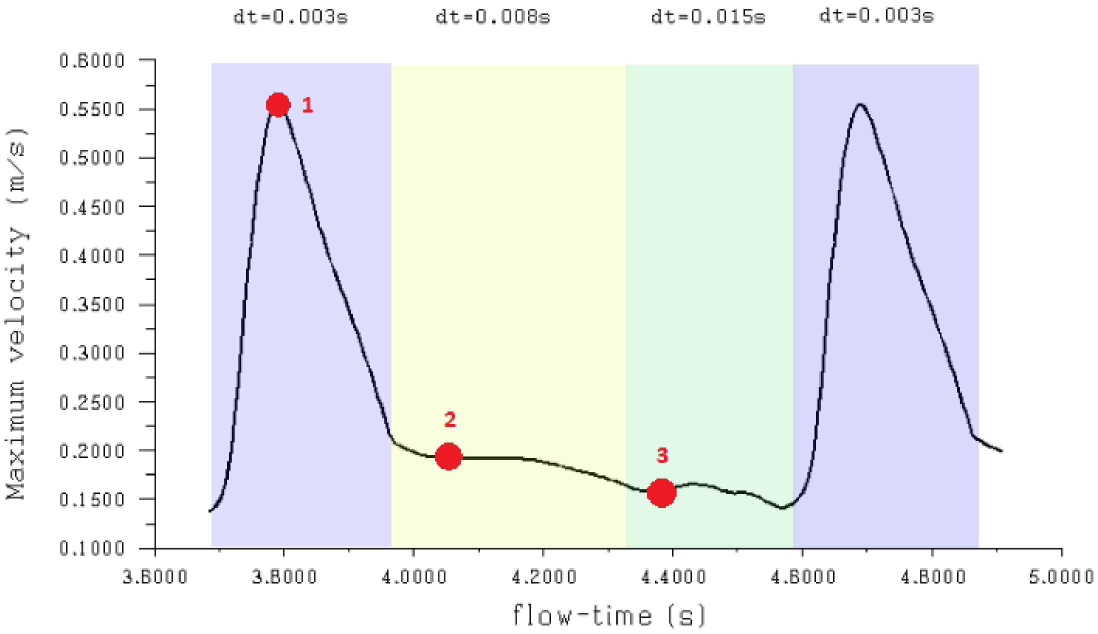

Figure 37 - Variable time step size during heartbeat and indication of representative points 1,2 & 3

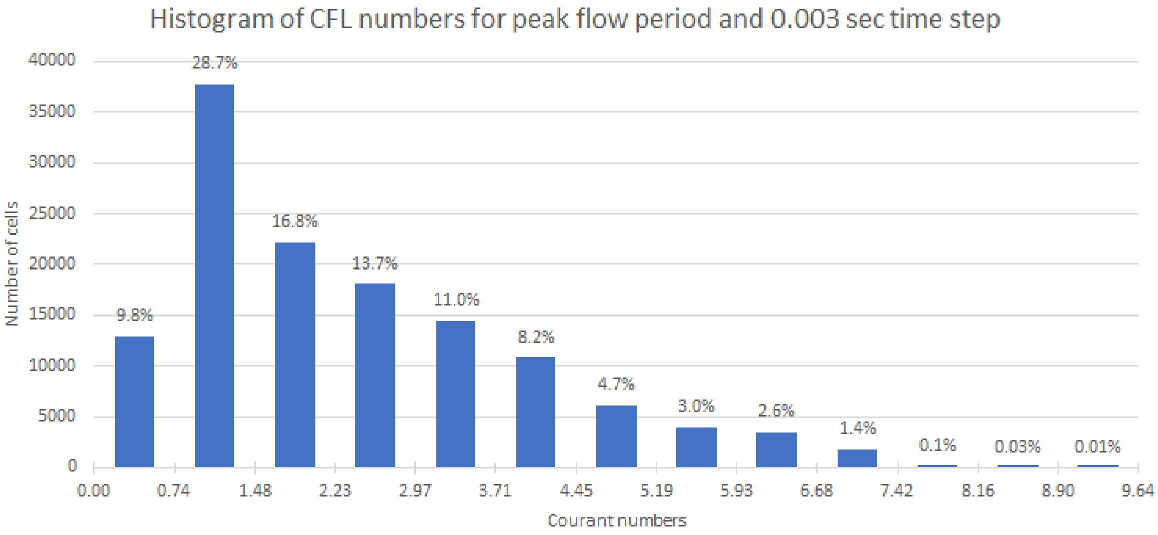

Figure 38 - Courant numbers at point 1: Peak systole

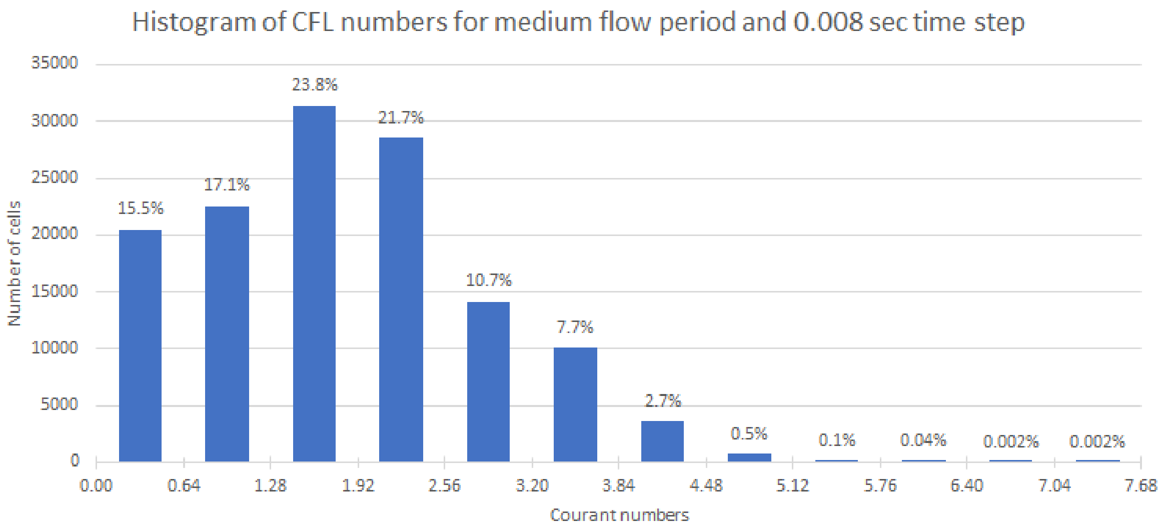

Figure 39 - Courant numbers at point 2: Early diastole

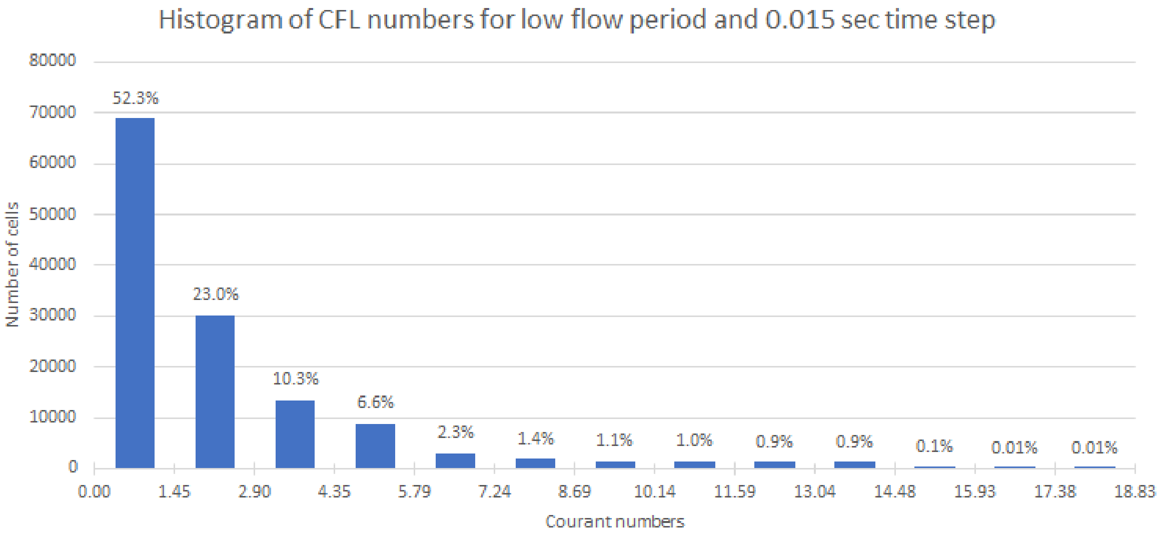

Figure 40 - Courant numbers at point 3: late diastole

Once appropriate time step sizes had been selected for each phase of the flow waveform, a user defined function was written to periodically adapt the time step size as shown in **Error! Reference source not found.** above.

2.9 Model for Thrombosis

In order to model the interaction between the thrombus and the haemodynamic environment, it is first necessary to keep track of the regions which are clotted and unclotted. For an extra layer of complexity, the region model should also differentiate between core and shell regions in the thrombus. This was achieved in ANSYS Fluent by means of a user-defined memory value for each computational cell. A numeric value is stored for each cell representing its identity in the following way:

Fluid	Bound platelet layer	Clot shell	Clot core
0	1	2	3

The purpose of storing a value for each cell is to limit the thrombus growth to appropriate regions. The thrombus should propagate out from the damaged endothelium rather than simply emerging anywhere in the fluid where fibrin is present. The concept behind the three numerical values is based on the platelet adhesion and agglomeration mechanism described earlier in section 1.4. Platelets bind to endothelium or other platelets to form a layer in which fibrin strands can form. The cells with number 1 represent this region of bound platelets, and consequently a computational cell can only have a value of 1 if it is adjacent to a cell which is either thrombus shell or endothelium. This layer of bound platelets is also less stable due to the lack of mature fibrin, so it is limited to be no more than one computational cell thick.

Once a cell containing bound platelets reaches a high enough concentration of fibrin, it changes to 2 and is now considered part of the thrombus shell. At this point the properties of the cell will change from the default for the fluid to those of thrombus shell. If fibrin concentration increases higher still, then the cell converts from shell to core, with properties changing accordingly.

Similar models which have aimed to represent the haemodynamic differences between fluid and thrombus, and between core and shell, have relied on porosity fraction and/or viscous resistance. These two mechanisms can be applied separately in ANSYS Fluent, and result in modifications of the continuity and conservation of momentum equations as shown in equations 2.12 and 2.13 below (Source: ANSYS Fluent user guide chapter 7.2.3).

$$\frac{\delta(\gamma\rho)}{\delta t} + \nabla \cdot (\gamma\rho\vec{v}) = 0 \tag{2.12}$$

$$\frac{\delta(\gamma\rho\vec{v})}{\delta t} + \nabla \cdot (\gamma\rho\vec{v}\vec{v}) = -\gamma\nabla p + \nabla \cdot (\gamma\vec{\tau}) + \gamma\vec{B}_f - \left(\frac{\mu}{\alpha} + \frac{C_2\rho}{2}|\vec{v}|\right)\vec{v} \tag{2.13}$$

Where:
γ represents porosity fraction, α is permeability, B_f is the body force vector and C_2 is the inertial loss coefficient.

Tomaiuolo [84] claimed that porosity fraction and hindered diffusion were sufficient to model a thrombus, and permeability was not necessary. The porous model used in their study to investigate core and shell was static and used values of 0.2 and 0.4 respectively. Govindarajan [86] used variable permeability based on fibrin and platelet concentrations and neglected porosity fraction, the key difference being that this model was not static, and aimed to show thrombus growth over time. This difference between strategies for static and dynamic initially seemed arbitrary, however, the reason became clear as soon as an attempt was made to apply porosity fraction to a dynamic model of a growing thrombus. In the fluid region $\gamma = 1$ but in cells converted to thrombus $\gamma = 0.7$. Permeability was infinite for the fluid region and $\alpha = 5.0\,E9$ in the thrombus region. Figure 41 shows the results of 14 seconds of flow time with a constant concentration of thrombin (100 nM/L) at the wall of the aneurysm sac.

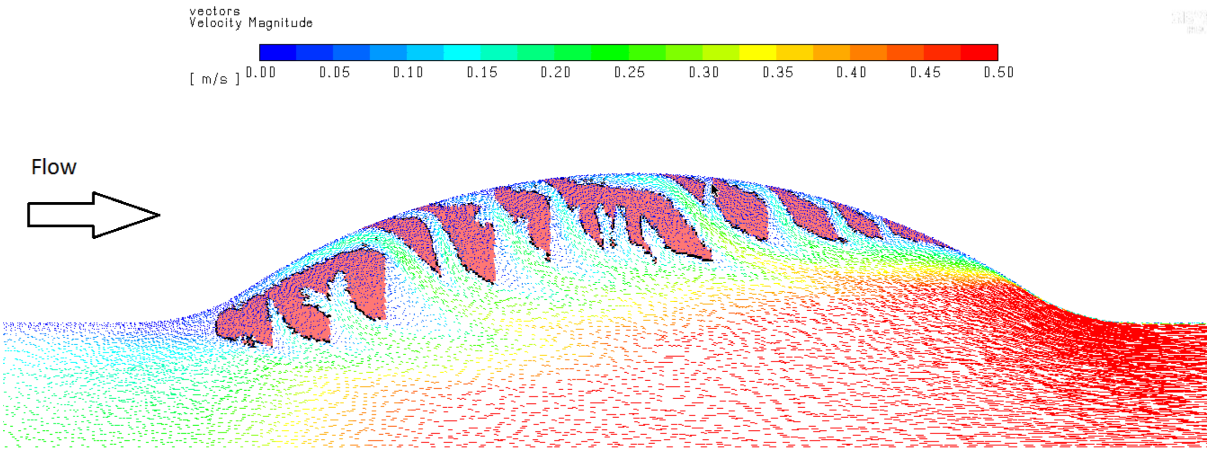

Figure 41 - Failed attempt to implement variable porosity in growing thrombus simulation

High velocity jets emerged from within the centre of the thrombus, driving rapid movement of thrombin and fibrin away from the vessel wall. This led to rapid growth in some zones, and severe lysis in others, leading to a striated pattern. These jets fed into the luminal flow and raised the outlet flow rate to be orders of magnitude higher than the inlet flow rate. A visual inspection of the velocity field indicates that mass and momentum are not conserved over the simulation domain, however, at each time step the Fluent solver was converging to residuals below 5e-4 for continuity and velocity components. This implies that each cell was satisfying the modified continuity and momentum conservation equations (2.12 & 2.13) to sufficient accuracy, therefore the problem must originate with the equations themselves.

A possible reason for this issue is the time derivative terms which contain γ in both the mass and momentum equations. Take for example the first term of the mass conservation equation (2.12). For a static porous region in an incompressible fluid, the first term $\delta(\gamma\rho)/\delta t$ will always be zero. For a moving porous region, a cell can change porosity from one time step to the next, so γ is variable in time and $\delta(\gamma\rho)/\delta t$ can be non-zero. This term represents the change in the mass of a cell over time, so for an incompressible fluid like blood it should always be zero. If a cell changes from fluid to shell, so that its porosity goes from 1.0 to 0.4 during a time step of 0.005, this term will now be in the order of 10^5 kg/(m^3s). This will in turn affect the second term in equation (2.12) and then the conservation of momentum equation (2.13). The result is the physically unreasonable velocity field seen in Figure 41.

While it may be possible to rewrite the governing equations so that porosity fraction can be included in a dynamic porous zone, that task was beyond the scope of this project. With the equations as they are applied in Fluent, it appears to be impossible to use porosity fraction in a zone of varying size. Given that a growing thrombus is a key feature of this model, and that Fluent had been selected as the ideal software for various other reasons, unfortunately porosity fraction had to be neglected from the thrombus model for all future simulations.

Permeability is taken into account by altering the α value in the conservation of momentum equation. The effect is to create a momentum sink which is proportional to velocity and inversely proportional to permeability. Fluent calls this effect viscous resistance, but it can also be referred to as the Brinkman term. Permeability values for core and shell were taken from Wufsus [90] and are based on experimental data of the constituent ingredients of an average clot. The core has a fibrin fraction of 49% and a platelet fraction of 12% according to Sadowski [72], which translated to a permeability value of 2 E-12 cm^2. Tosenberger [43] claimed that the shell has lower fibrin concentration, however, it is not clear how this translates to a value for fibrin fraction. A fibrin concentration of 3% and a platelet concentration of 12% were selected resulting in a permeability that is two orders of magnitude greater than the core. This shell permeability of 2 E-10 cm^2 is supported by the experimental work by Kim [71] which found that the shell permeability is roughly 100 times that of the core and is in the range of 10^{-12} to 10^{-9}. Inertial resistance was neglected due to lack of precedent and experimental data.

A final mechanism of the model is lysis due to stress on the surface of the thrombus. Cells can only become thrombus shell or core when shear stress is sufficiently low, and they can revert back to fluid by the effect of high shear stress. A shear stress limit of 211 Pa was used based on the experimental work of Riha [92]. Observation during simulation showed that this value was close to optimal, as the thrombus could grow to fill the aneurysm sac and cause some stenosis, but never fully occlude the vessel. Lysis based on strain rate was not utilised as values observed in the flow were orders of magnitude lower than the 83 000 s^{-1} level recommended by Brass [77]. A diagram showing the criteria for conversion from one identity to the next is shown in Figure 42 below.

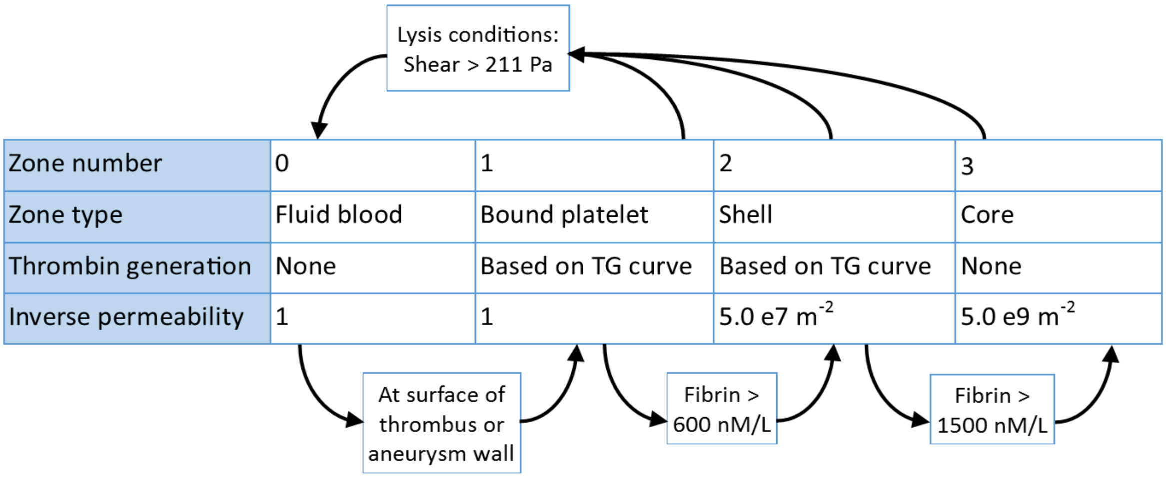

Zone number	0	1	2	3
Zone type	Fluid blood	Bound platelet	Shell	Core
Thrombin generation	None	Based on TG curve	Based on TG curve	None
Inverse permeability	1	1	5.0 e7 m^{-2}	5.0 e9 m^{-2}

Figure 42 - Modelling strategy for conversion from fluid blood to multi-zone thrombus

2.10 Summary of Computational Strategy

ANSYS Fluent is an efficient and detailed fluid dynamics solver which has many built-in features, however, for specific problems, additional customisation is necessary. User defined functions (UDFs) can be written in the C++ code language and compiled within fluent to adjust almost any feature of the fluid problem and the solver properties. The following is a pseudo-code version of the computational methods implemented at each time step. The first step is completed by the Fluent solver, but the rest are implemented by custom UDFs.

For each time step:

1. Solve velocity and pressure field from previous time step so that velocity, scalar transport and continuity residuals are less than 10e-4

2. Calculate appropriate inlet velocity for time step based on flow rate waveform
3. Apply flow rate to inlet boundary in the form of a parabolic velocity profile
4. Calculate thrombin concentration based on function for TG curve
5. Apply this value to the appropriate region where thrombin is being generated
6. Loop over every computational cell and do the following:
    6.1. Calculate how much fibrinogen is converted to fibrin according to Michaelis-Menten kinetics
    6.2. Increase fibrin concentration and decrease fibrinogen concentration by this amount
    6.3. For cells containing bound platelets, if fibrin concentration is above 600, convert to shell
    6.4. For shell cells, if fibrin concentration is above 1500, convert to core
    6.5. For all fluid cells, if any neighbour is not fluid, become bound platelet layer.
    6.6. For all non-fluid cells, if shear stress in cell or any neighbour cell is greater than 211 Pa, convert cell to fluid
7. Find length of next time step based on adaptive step sizing function
8. Write flow data to file and record image for animation
9. End and move to next time step to repeat from 1.

2.11 Summary of Fluid Values

The following table shows the values used for all fluid and modelling variables used for the final simulations including the reference for the chosen value.

Variable	Value	Reference
Density of blood	1033 kg/m^3	[43]
Viscosity of blood	3.5 E-3 kg/(m s)	[35]
Porosity of clot core	0.35	[77]
Porosity of shell	0.7	[77]
Viscous resistance of clot core	2.0 E-12 m^2	[90]
Viscous resistance of clot shell	2.0 E-10 m^2	[71]
Minimum fibrin concentration to become clot shell	600 nM	[37]
Minimum fibrin concentration to become clot core	1500 nM	[38]

Minimum shear stress for lysis	211 Pa	[92]
Minimum shear rate for lysis	83000 s^{-1}	[77]
Diffusion coefficient of thrombin	6.68 E-8 kg/(m s)	[38]
Diffusion coefficient of fibrinogen	3.20 E-8 kg/(m s)	[38]
Diffusion coefficient of fibrin	2.55 E-8 kg/(m s)	[38]
Blood concentration of fibrinogen	7000 nM/L	[38]
k_{cat} for Michaelis-Menten reaction	3450 min^{-1}	[38]
K_M for Michaelis-Menten reaction	3160 nM	[38]
Heart rate	66.6 bpm	n/a

Table 11 - Values used for model constants

3 Results

3.1 Strategy A

The two strategies for location of thrombin generation which were discussed at the end of section 0 are here named A and B. In strategy A the region of thrombin generation was restricted to the concave section of the aneurysm wall. The value for thrombin concentration was initially maintained at 300 nM/L in order to see the result of this strategy with high thrombin concentration at the boundary. The thrombin concentration was applied to a layer of computational cells adjacent to the vessel wall. Diffusivity was raised to the over-diffusive case, where all three chemical species have a diffusivity constant of 10^{-8} m^2/s. The simulation was run for 87 seconds of flow time. The result at the end of this time is shown in Figure 43 below.

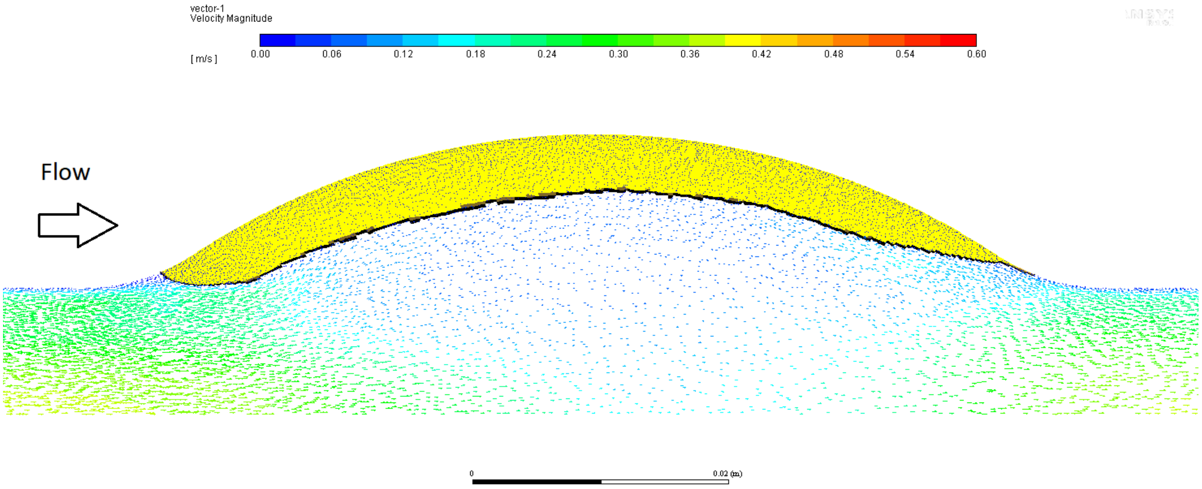

Figure 43 – ILT with velocity vectors for over-diffusive, high thrombin concentration environment using strategy A

The first thing to notice in Figure 43 is that the ILT has a consistent thickness, with slightly more volume on the proximal side. This indicates that the effects of advection have been negligible, as one would expect the flow from left to right to carry thrombin and fibrin downstream, thus promoting more thrombus growth in the distal region of the aneurysm. One of the key findings of Biasetti [75] was this specific feature, namely that ILTs grow larger in the distal region due to the effects of advection. The uniform thickness is consistent with purely diffusive transport, as pure diffusion would cause thrombin molecules across the concave boundary to spread at a uniform rate. As thrombin moves outwards, layers of fibrin will be generated and deposited over the entire ILT boundary, thrombin will advance slightly further by diffusion - and the process repeats. Distribution of thrombin is shown below in Figure 44, demonstrating that thrombin does indeed diffuse normal to the boundary in a uniform and consistent way despite the pulsatile flow conditions.

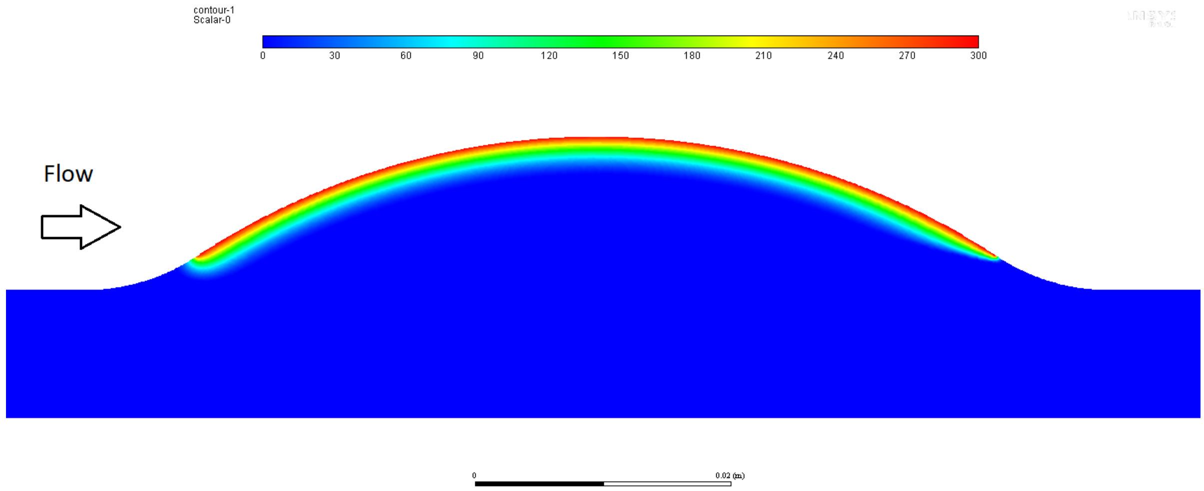

Figure 44 - Thrombin distribution for over-diffusive, high thrombin concentration environment using strategy A

The second key feature of this test was the concentration of fibrin within the thrombus. The plot of fibrin concentration in Figure 45 below shows that most of the ILT interior has the maximum fibrin content is 7000 nM/L. This figure is the maximum because fibrinogen concentration in the incoming blood is 7000 nM/L, and fibrin can only be formed by the conversion of available fibrinogen. This high concentration shows that fibrin generation is proceeding quickly within the ILT, but this does not translate to quick growth of the ILT volume. Again, this is probably due to the effect of slow diffusion and negligible convection, as the fibrin molecules have no way to escape the cell in which they are generated.

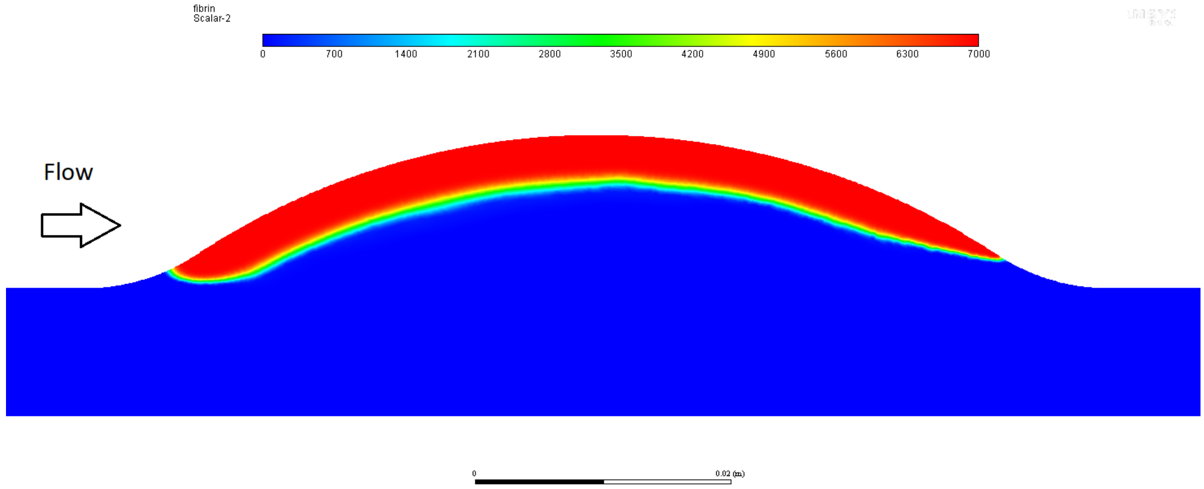

Figure 45 - Fibrin distribution for over-diffusive, high thrombin concentration environment using strategy A

The experiment was repeated, but this time with the thrombin concentration curve applied as the boundary condition rather than a fixed 300nM/L. Given that the peak thrombin concentration of this curve was 264.1 nM/L, and the initial value less than 10 nM/L, it was assumed that the ILT would grow more slowly than the previous test. This test would also show if the variable thrombin concentration has a corresponding effect on ILT growth rate. The evolution of ILT size and boundary thrombin concentration are shown in Figure 46 below.

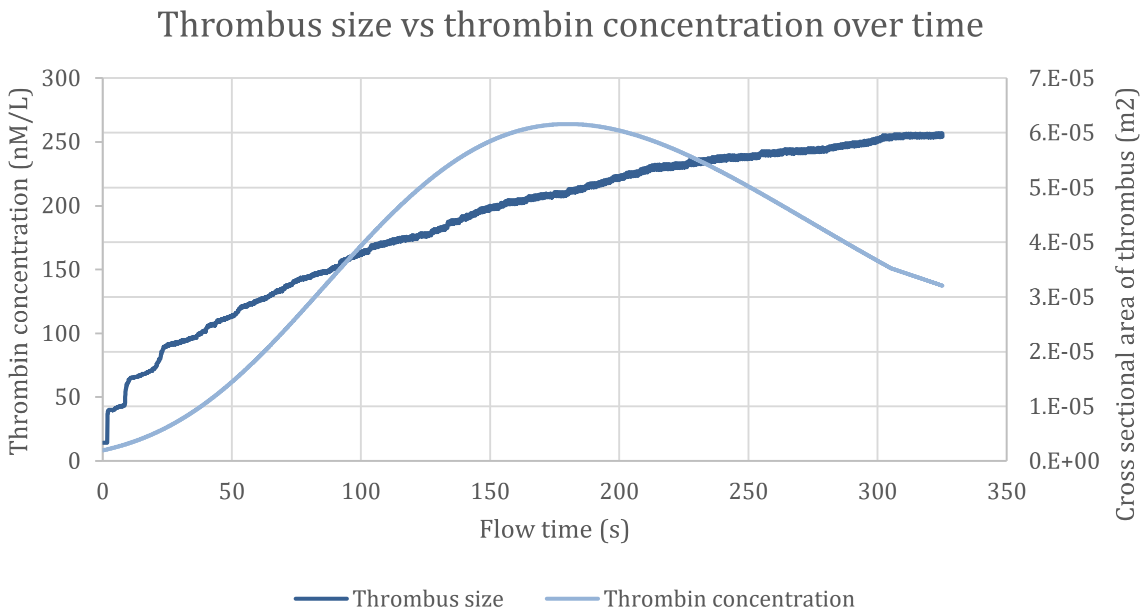

Figure 46 - ILT growth for strategy A

Figure 46 shows that ILT growth rate is largely independent of thrombin concentration. In fact, ILT growth is at its fastest when thrombin levels are relatively low. This demonstrates that even small quantities of thrombin can generate sufficient fibrin to drive clot growth. Over time the thrombus growth rate decreases at a uniform rate until it stalls at the 5-minute mark. This slowing growth could be due to various reasons. Firstly depletion of fibrinogen. This would explain why increasing thrombin makes no difference to growth rate, as it is no longer a limiting factor. A second option is that growth rate decreases as thrombus size increases. This would confirm the self-limiting mechanism of thrombus growth mentioned previously. As the thrombus/fluid boundary moves away from the vessel wall, less thrombin can reach it, so at some point there is insufficient thrombin to generate fibrin and the growth stops. A third option is the effect of mechanical lysis, which will be discussed in the next paragraph. Figure 47 below shows the barely-visible thrombus after 150 seconds of flow time.

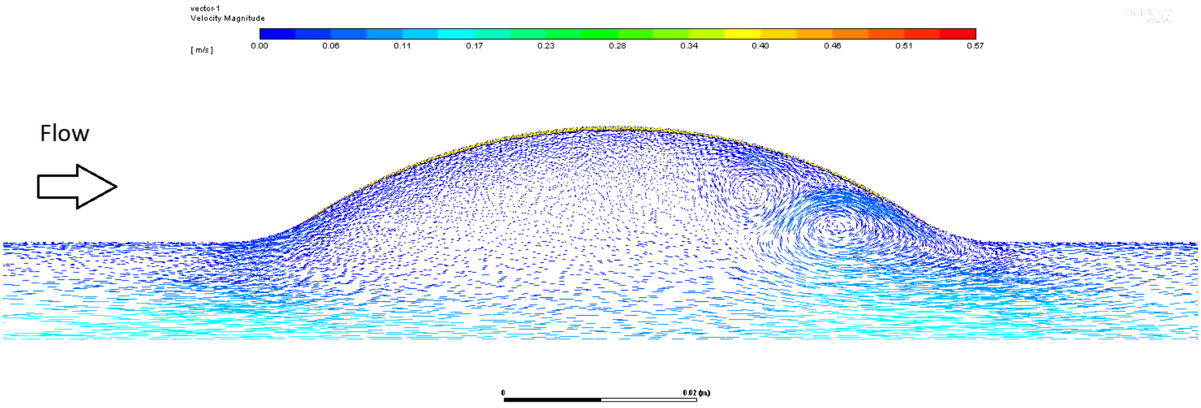

Figure 47 - Final ILT and velocity vectors for strategy A with TG curve boundary condition

Thrombus growth rate was found at each time step by calculating change in ILT volume over time step size. This data was smoothed using the 10 point moving average method. The growth rate is plotted against average inlet flow velocity in Figure 48 below in order to investigate the impact of mechanical lysis due to shear.

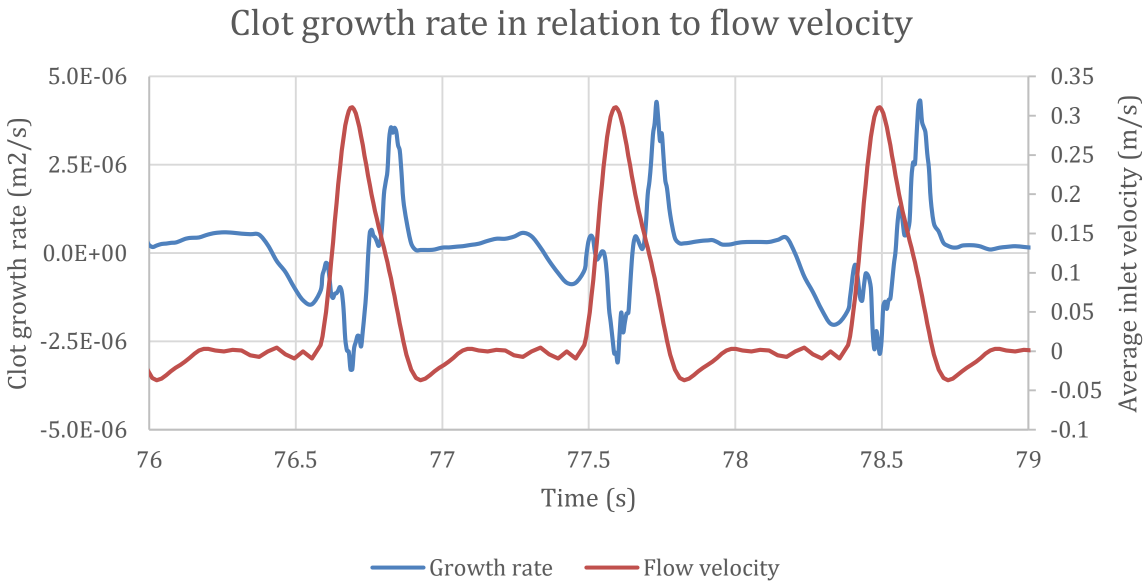

Figure 48 - Growth rate and flow velocity for strategy A with TG boundary

From Figure 48 it is clear that growth rate is negative before and during early systole, then briefly positive during late systole. For the rest of the waveform growth rate is slightly positive. This graph is limited to the period from 76 to 79 seconds for clarity, but the pattern is consistent for most of the flow duration, with the ratio of negative growth to positive becoming greater later on. The mechanism responsible for this negative growth is lysis due to shear stress at the fluid/thrombus interface. Clearly the velocity at peak systole is high enough to cause lysis, but the lysis before systole is surprising and unexplained. What is clear is that the positive and negative growth peaks are remarkably similar in magnitude and duration, so a small change to either could alter the overall trend of thrombus growth. After roughly 5 minutes, the positive and negative growth are in perfect balance and the thrombus remains a constant size.

While these results have shown some interesting features of the model, strategy A is not a suitable approach for simulating growth of ILTs. It is insensitive to thrombin concentration, the self-limiting of size is too extreme and the structure of the thrombus does not match physiological observations.

3.2 Strategy B

For the first attempt using strategy B, the BFC was set at 3000 nM/L. The growth of the thrombus was more rapid than with strategy A, and showed a continuously increasing growth rate leading to full occlusion of the aneurysm sac within 30 seconds. BFC was then reduced to 1500 nM/L and finally 601 nM/L essentially removing the thickness of the shell layer. Occlusion times and growth rate were almost identical for all three, so 1500 nM/L was used for all subsequent simulations. Thrombus size and thrombin concentration are shown on Figure 49 below.

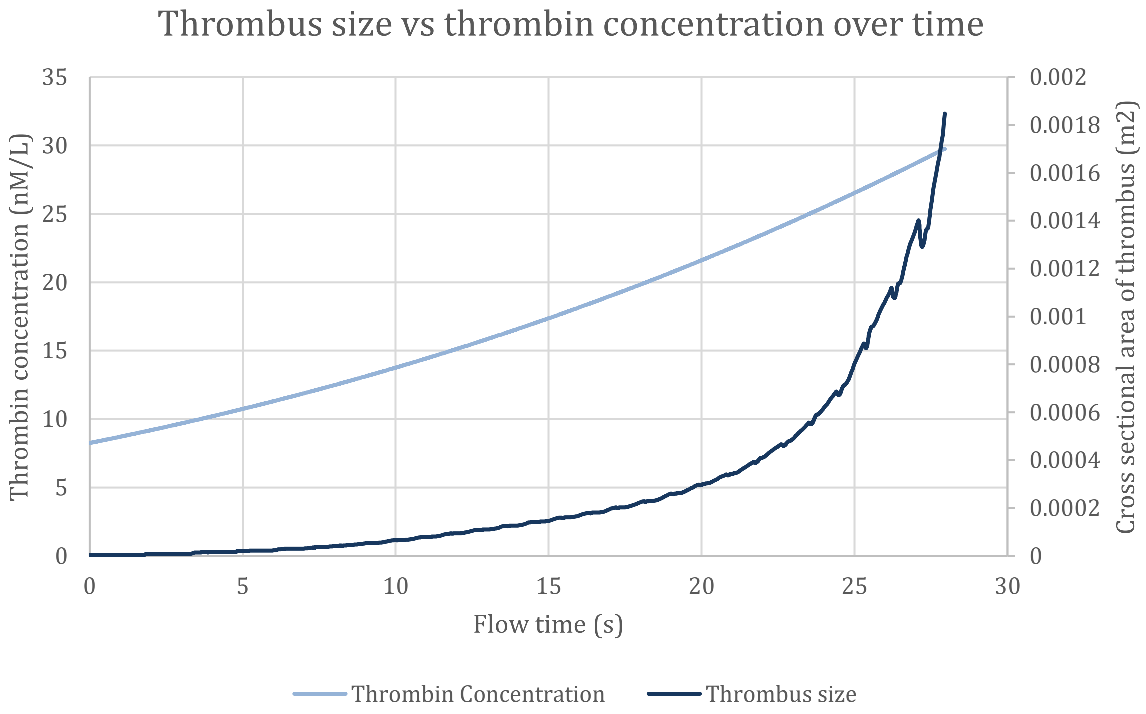

Figure 49 - ILT size and TG curve for strategy B

A detailed view of thrombus growth rate in Figure 50 below shows that the magnitude of growth and lysis become more extreme over time. Between 20 and 28 seconds the thrombus had grown to fill the aneurysm sac and was beginning to encroach on the luminal region of the aorta. This constriction of the free-flowing area, known as stenosis, causes the velocity of the blood to increase in this region. Higher velocity leads to higher shear stress on the surface of the thrombus and hence more severe lysis, however, it is not obvious why the trend of growth rate clearly increases over this period. Either the increasing growth rate is linked to the increasing thrombin concentration, or there is some self-accelerating mechanism in the model which causes growth rate to increase over time regardless of changing thrombin concentration.

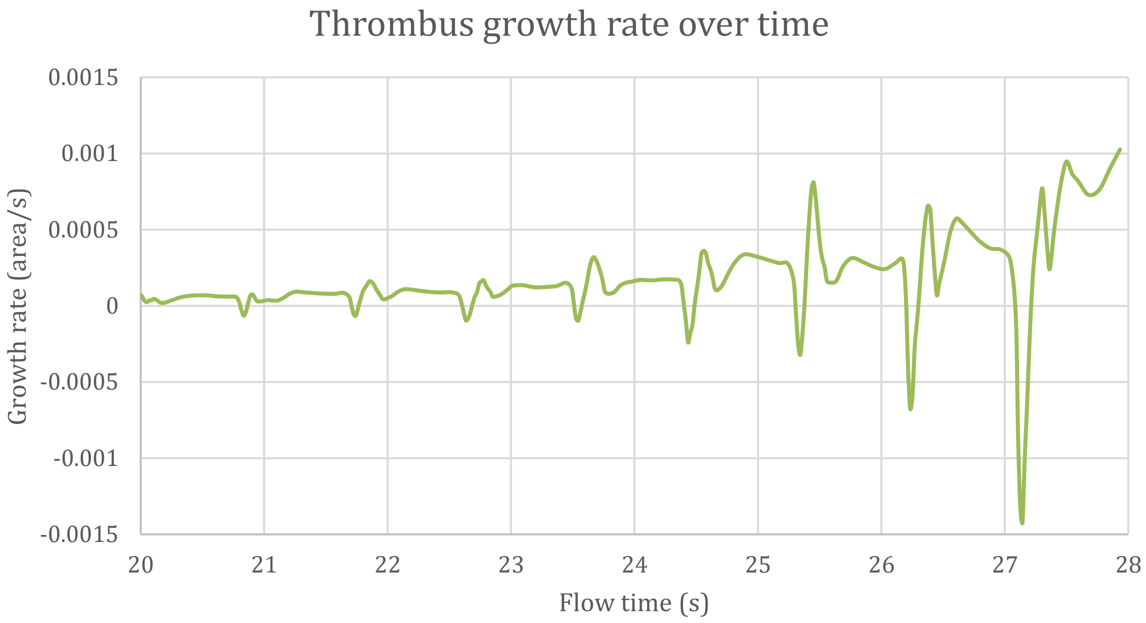

Figure 50 - ILT growth rate for strategy B

To better understand the mechanisms driving thrombus growth, the period of observation was moved back to 20 seconds. At this point the thrombus had occluded roughly half of the aneurysm sac and was not experiencing the extreme lysis that accompanies full occlusion or stenosis. Figure 51 below shows that lysis does occur during early and late systole, most likely due to the rapidly changing velocity during these periods. During the diastolic period the thrombus grows rapidly, which contrasts with the negligible growth rate during diastole seen in the previous simulation. Another difference is that peak growth in the previous model was during late systole, whereas in this case growth rate is slightly negative during this period. These observations show that changing the location of thrombin generation leads to a fundamentally different relationship between the haemodynamic environment and the growth and lysis mechanisms.

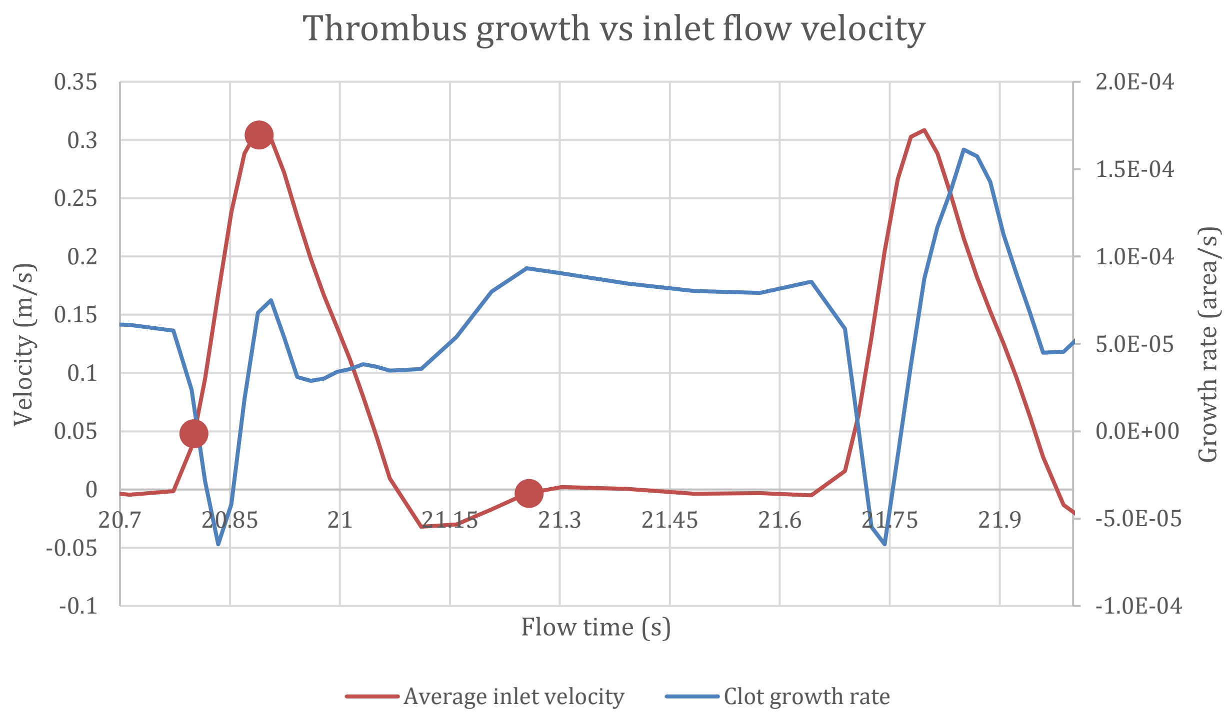

Figure 51 - Growth rate and velocity for strategy B between 20.7 and 22 seconds

Visualisation of the flow velocity and shear stress was carried out at three points during a single heartbeat in order to clarify where lysis and growth are occurring.

3.2.1 Point 1: Flow time = 20.8 seconds

The first point is at 20.8 seconds, representing early systole and the moment when growth rate is close to zero. The flow field at this time is uni-directional and smooth, and the velocity around most of the ILT is low. The exception is the proximal edge of the thrombus, which is adjacent to a region of high velocity. In most of the following images black represents the bound platelet layer, dark grey or pink is the thrombus shell and yellow is the thrombus core.

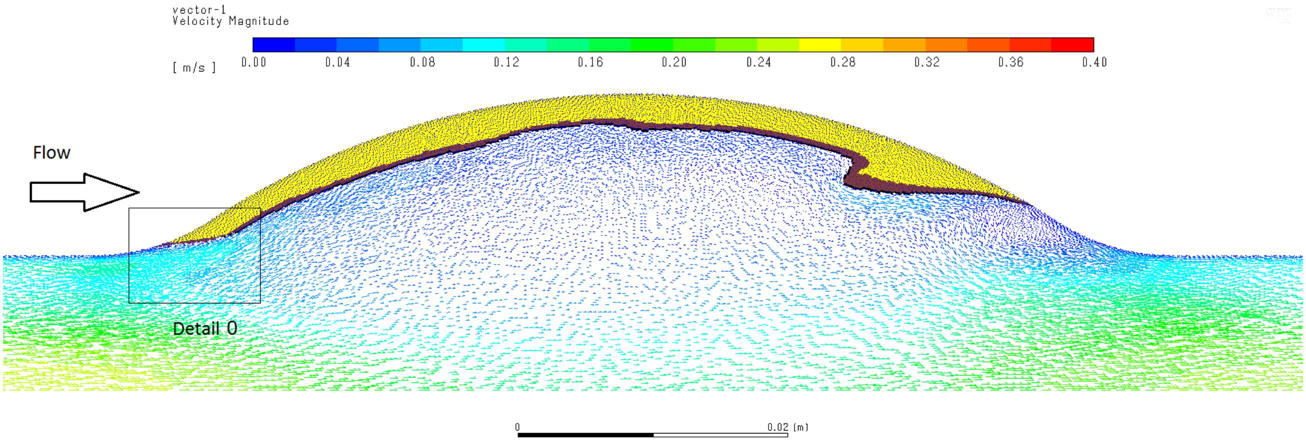

Figure 52 - ILT region and velocity vectors for strategy B at 20.8 sec

Closer investigation of the area marked ‘Detail 0’ in Figure 52 shows that the shear stress exceeds 211 Pa at the surface of the thrombus. This means that lysis is occurring at this part of the thrombus boundary. In Figure 53 the thrombus colours have been converted to greyscale to emphasise the colour contours of shear stress magnitude.

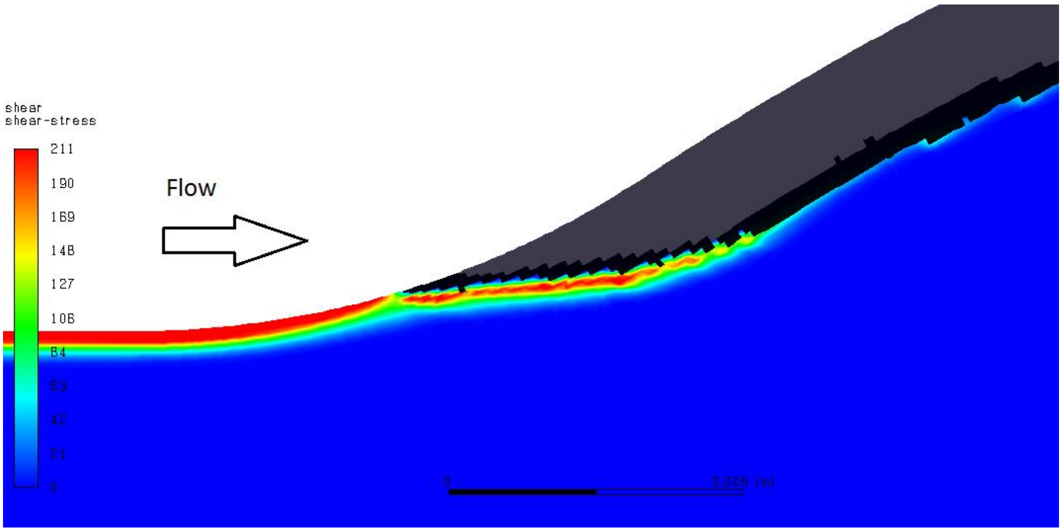

Figure 53 - Shear stress at ILT boundary in ‘Detail 0’ area at 20.8 seconds

3.2.2 Point 2: Flow time = 20.9 seconds

The second moment of interest is at 20.9 seconds. This moment coincides with peak systole and a small spike in growth rate as evident in Figure 51. The flow field and thrombus region are shown in Figure 54 below.

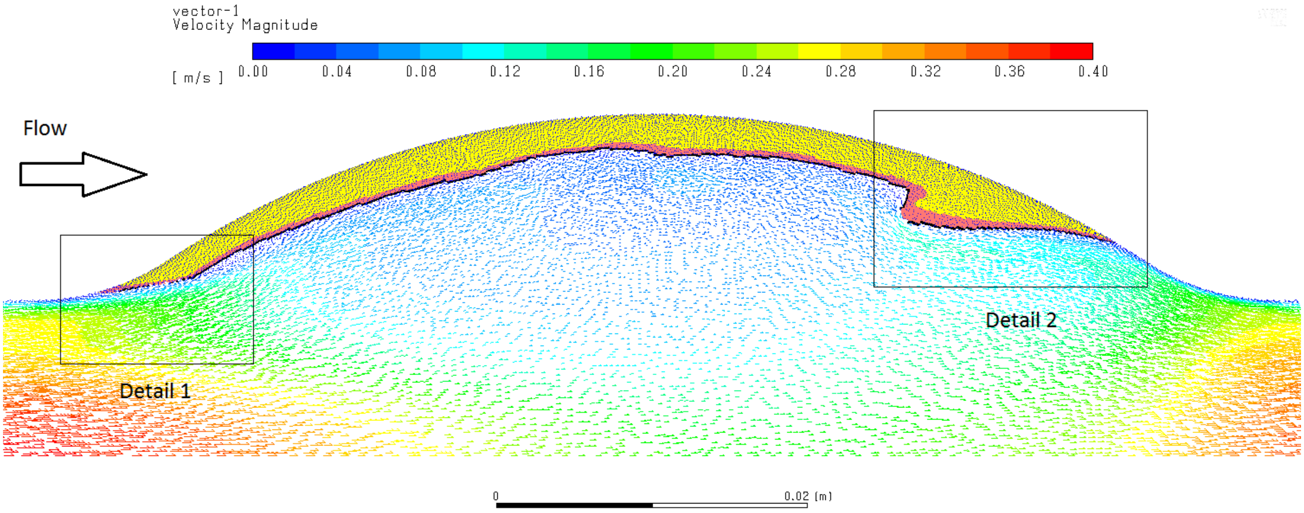

Figure 54 - ILT region and velocity vectors for strategy B at 20.9 sec

Naturally the luminal velocities are higher at peak systole as evidenced by the red velocity vectors, however the velocity over most of the ILT boundary is still low. The regions with high velocity have been analysed in more detail. In the region marked ‘Detail 1’ we can see that the region of high shear stress at the neck of the aneurysm has moved from the previous time point, leading to a reduction in lysis at the proximal edge of the ILT.

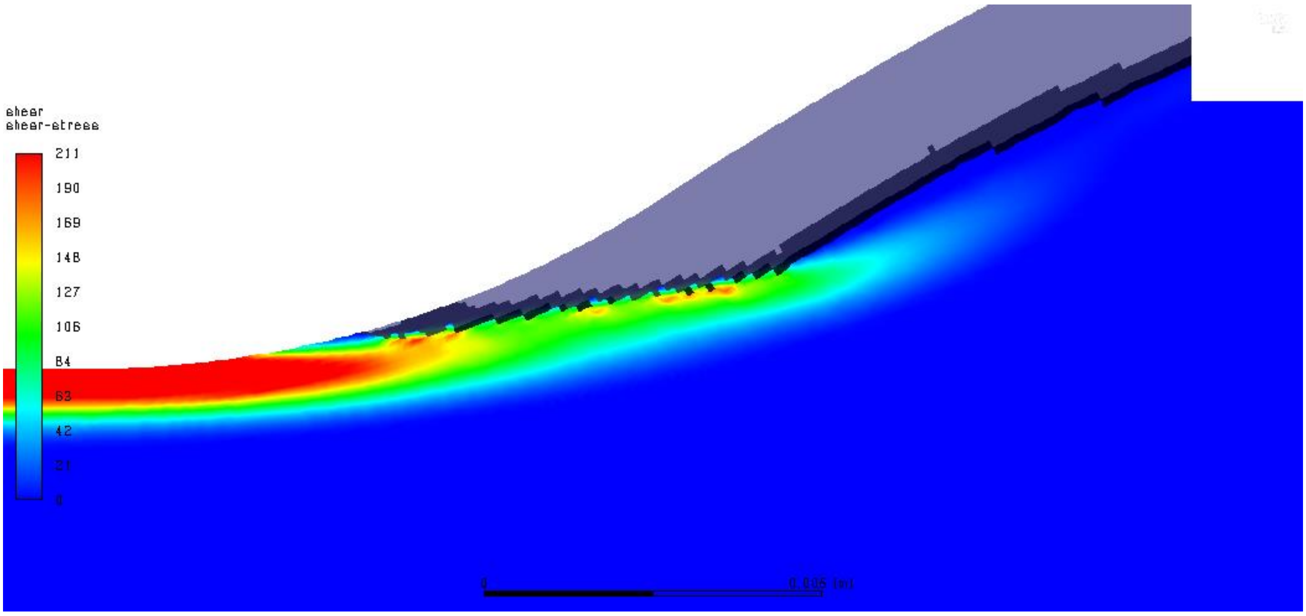

Figure 55 - Shear stress at ILT boundary in 'Detail 1' area at 20.9 seconds

In the area marked 'Detail 2', lysis is occuring over a small region of a protrusion of the thrombus. Note in Figure 56 the high shear stress at the distal boundary of the aneurysm sac which has prevented any thrombus growth in this region.

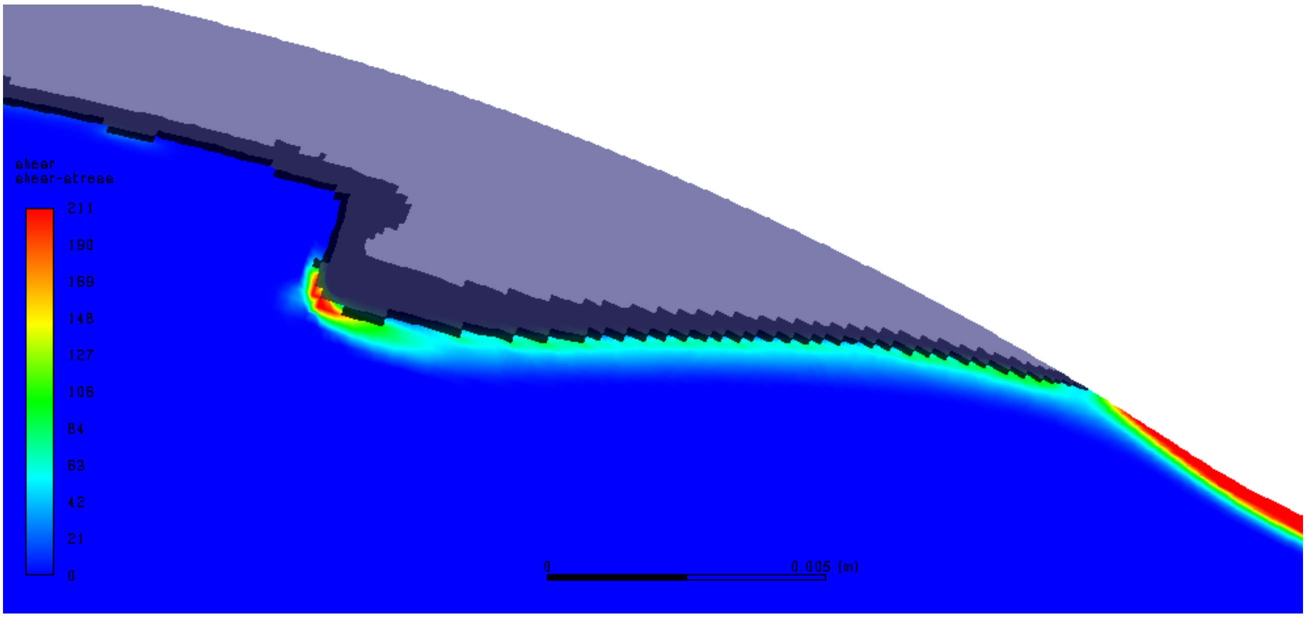

Figure 56 - Shear stress at ILT boundary in 'Detail 2' area at 20.9 seconds

These figures show that lysis decreases in one location and increases in another, so this does not yet explain the increase in growth rate at peak systole. A possible explanation is that higher velocities cause fibrin to exprerience greater convection from the thrombus shell out into to bound platelet layer. A faster supply of fibrin in the bound platelet layer will lead to rapidly incresing fibrin concentration and ultimately shell formation. Figure 57 below shows an overlay of velocity vectors and fibrin concentration represented by colour.

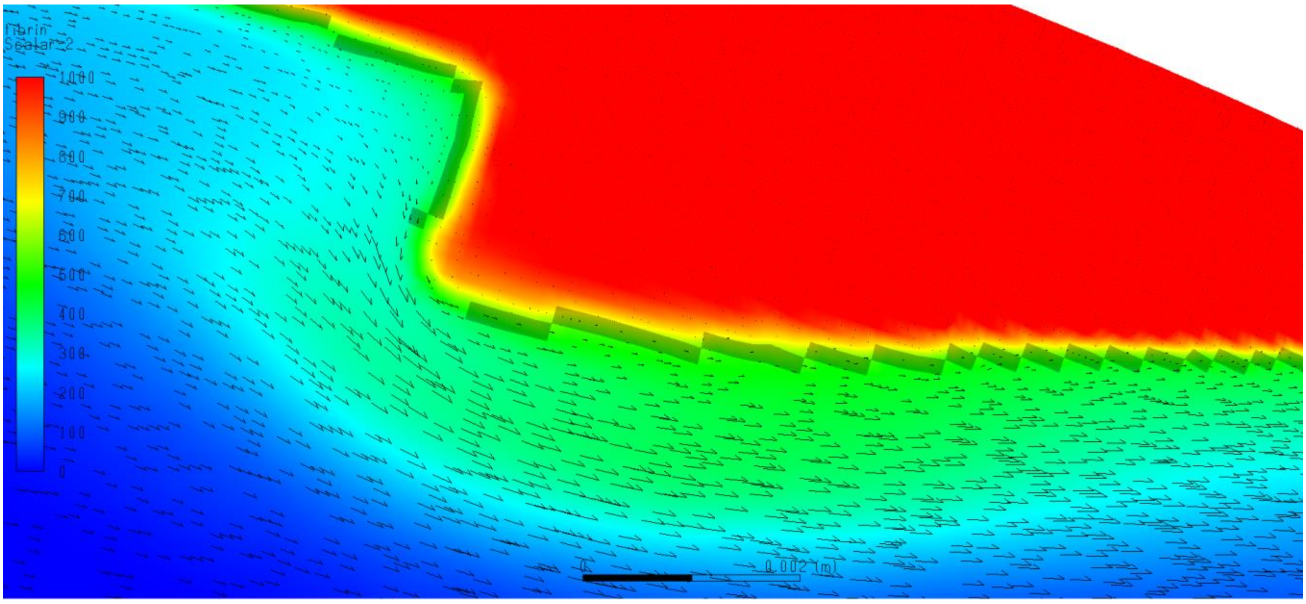

Figure 57 - Fibrin concentration and velocity vectors in 'Detail 2' region at 20.9 seconds

Figure 57 shows that fibrin is widely distributed outside the thrombus at concentrations approaching the 600 nM/L necessary for shell formation. A high velocity flow path appears to pick up fibrin as it passes the protrusion of the thrombus, this fibrin travels to the right and enriches a zone of high concentration (green). The region of slow velocity in the top left has much lower concentration of fibrin, which imples that the high velocity flow stream is directly responsible for a region of high fibrin concentration adjacent to the ILT boundary. The connection between this convection of fibrin and thrombus growth is demonstrated in Figure 58 below.

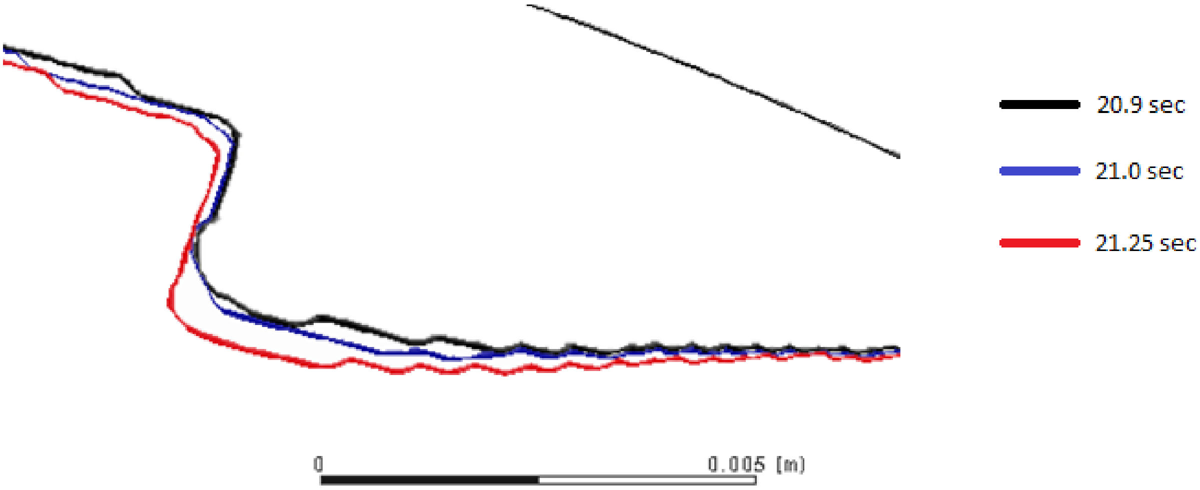

Figure 58 - Moving boundary of ILT in 'Detail2' region

The black line represents the thrombus boundary at 20.9 seconds (peak systole) as seen in the previous image. The blue line shows the thrombus boundary at 21.0 seconds (end of systole). This profile indicates that the thrombus has grown most notably in the region of high fibrin concentration brought about by convection past the thrombus protrusion. This provides clarification on the increased growth rate during peak systole – essentially high velocity can promote rapid thrombus growth provided shear stress is below lysis levels and provided the boundary of the thrombus has some irregular geometry.

The red line shows the boundary of the clot at 21,25 seconds. This coincides with early diastole and the maximum growth rate for this heartbeat cycle.

3.2.3 Point 3: Flow time = 21.25 seconds

The boundary has expanded in all directions, but the largest growth is at the sharp end of the protrusion. In the following figure we see that the same mechanism as before is at play. Convection of fibrin with the flow promotes faster clot growth in some regions than others, and these fast growth regions are generated by irregular geometry of the thrombus.

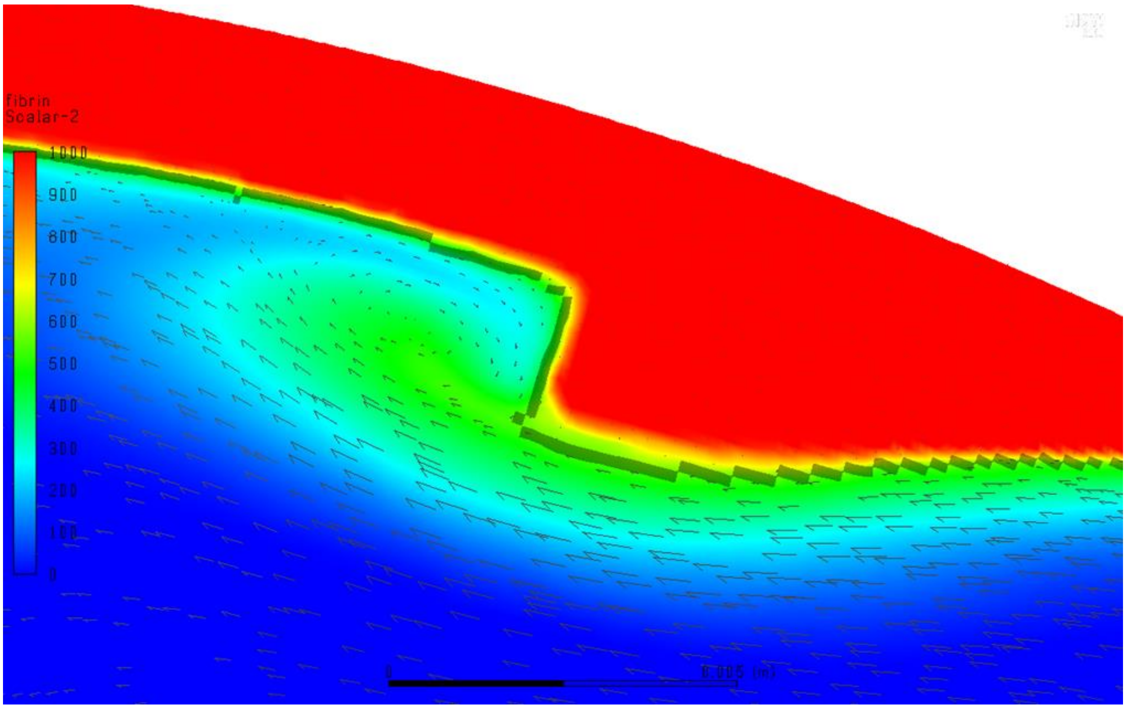

Figure 59 - Fibrin concentration and velocity vectors in 'Detail 2' region at 21.25 seconds

A wider view shows why the fluid is moving to the left in the image above. During diastole an anti-clockwise rotation emerges in the aneurysm sac. The curving reverse flow in the distal part of the aneurysm sac appears to be responsible for the growth of the protrusion seen above. The reverse flow over the thrombus surface carries thrombin and fibrin towards the aneurysm neck. This leads to the rapid growth of a structure indicated with an oval in Figure 60. However, we have seen that the aneurysm neck is a site of high shear stress during systole, so this structure is completely removed by lysis during the following heartbeat.

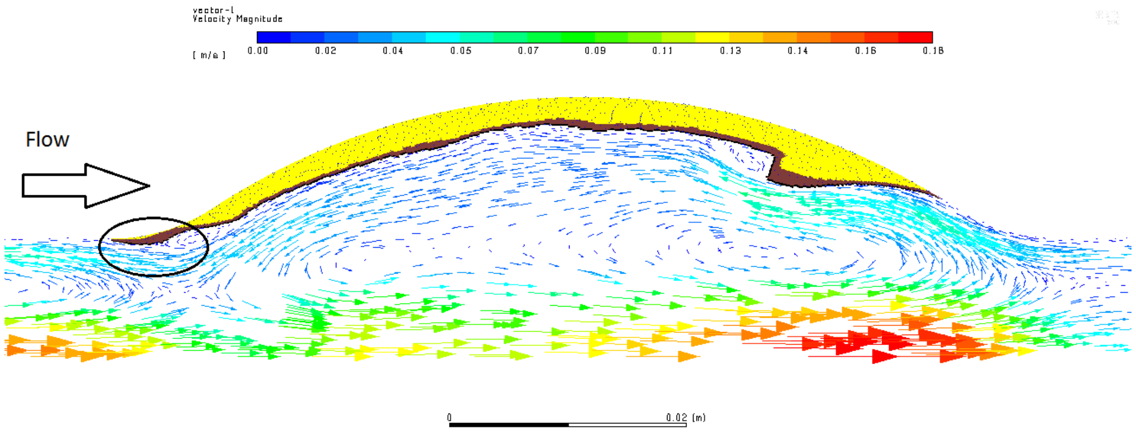

Figure 60 - ILT region and velocity vectors at 21.25 seconds. Region of rapid proximal growth indicated.

3.3 Vortical Structures and Thrombin Distribution

Vortical structures due to transient flow within the aneurysm are a source of great interest in Biasetti [75]. Their simulation shows an anti-clockwise vortex forming at the aneurysm neck during systole, then travelling downstream during diastole until it ultimately breaks apart on the distal wall of the aneurysm sac. The vortical structures were not as clearly defined in the present model, most likely due to differences in the transient flow waveform, however the phenomenon described above does clearly occur. An added feature of the present model is the opportunity to see how these vortical structures influence the shape of the thrombus, both by creating the conditions for lysis and by affecting protein transport. In order to demonstrate this graphically, three consecutive time points are analysed in detail. The time points are 25.5, 25.64 and 26.11 seconds. These points are shown on the graph of flow rate and thrombus growth in Figure 61 below.

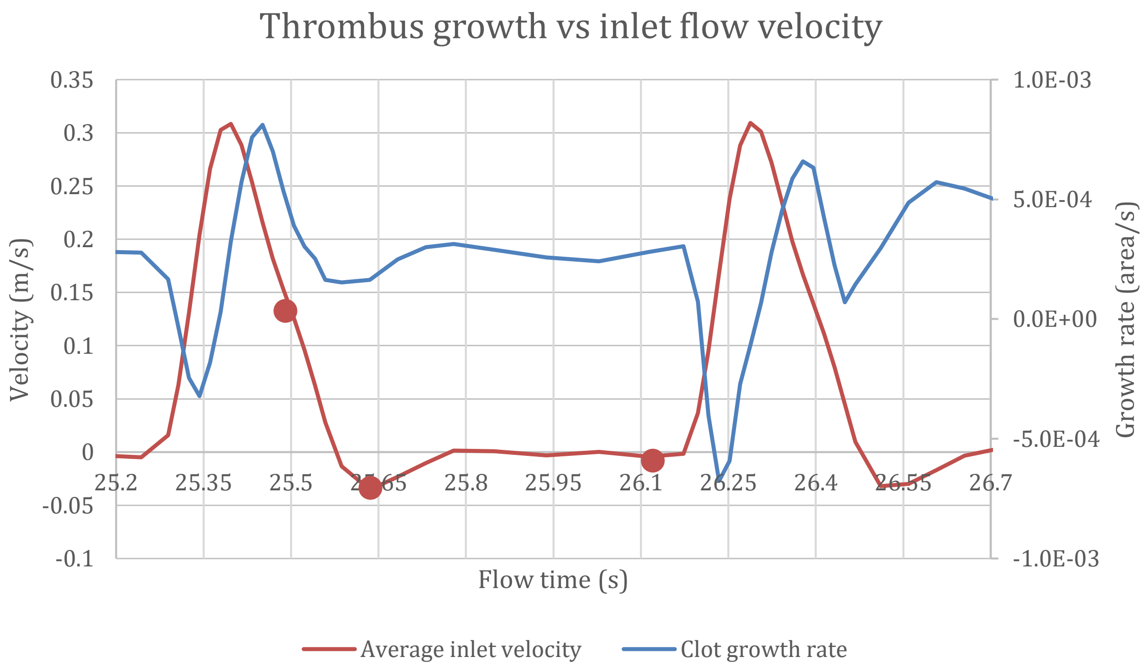

Figure 61 - Growth rate and velocity for strategy B between 25.2 and 26.7 seconds

3.3.1 Point 4: Flow time = 25.5 s

Flow separation at the aneurysm neck during peak systole gives way to a vortex in the same location as flow begins to slow. This anti-clockwise vortex is marked with an “x” in Figure 62. The vorticity magnitude at the same moment is shown in Figure 63.

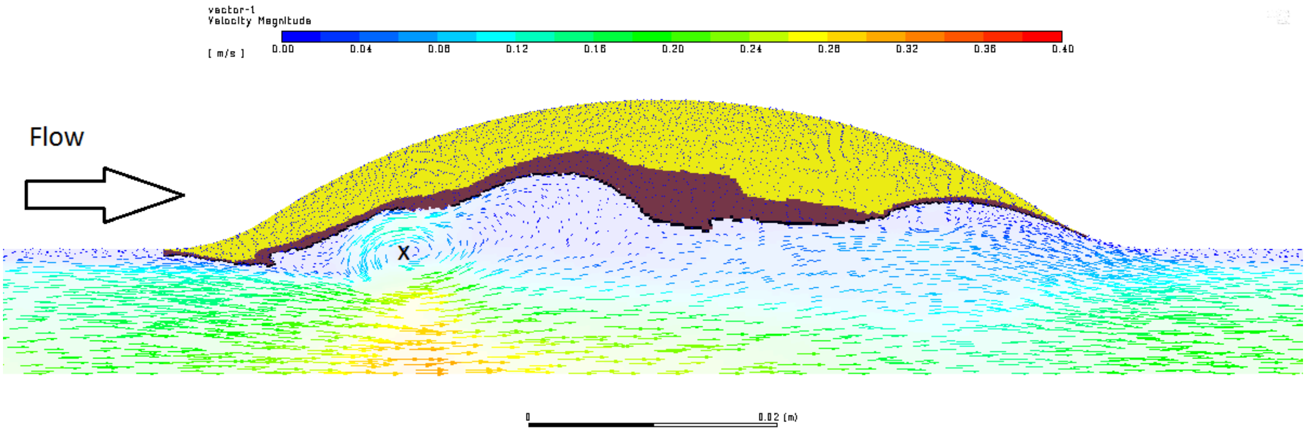

Figure 62 - ILT region and velocity vectors for strategy B at 25.5 sec

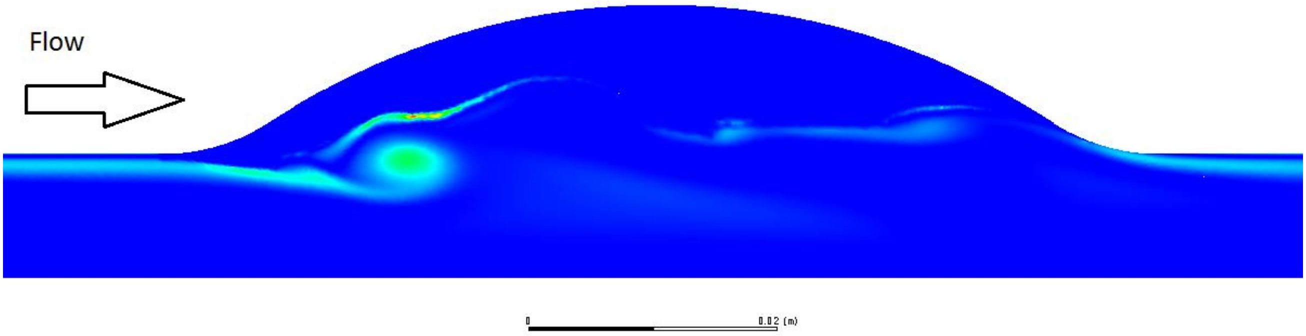

Figure 63 - Vorticity magnitude for strategy B at 25.5 sec

In Figure 62 above a concave depression is evident in the thrombus boundary which corresponds with the position and curvature of vortex. Is the vortex responsible for the shape of the boundary, or does the curvature of the boundary promote the formation of the vortex? Given that Biasetti [75] demonstrated the formation of a vortex in this position without a thrombus, it is more likely that the vortex is influencing the shape of the thrombus. Figure 63 shows a contour plot of vorticity magnitude to show the position of the vortex marked ‘x’ more clearly.

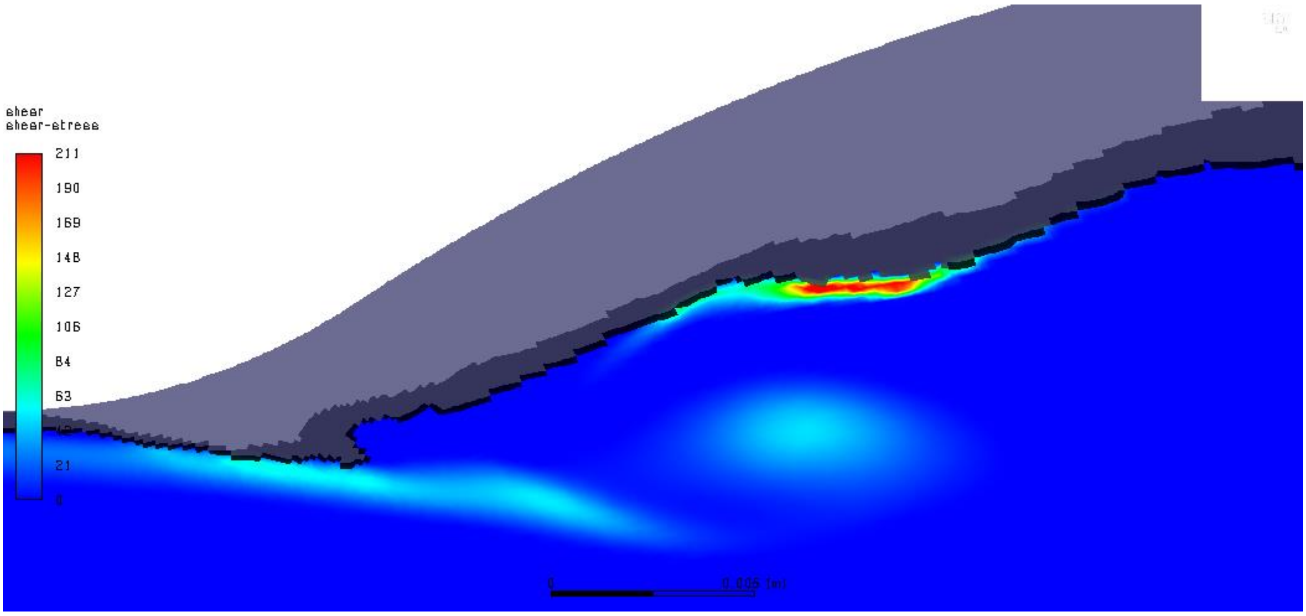

Figure 64 – High shear stress caused by vortex ‘x’ leading to localised lysis

Figure 64 shows a close-up view of region of high shear stress on the thrombus surface corresponding to the position of the upper edge of vortex ‘x’. The shear stress is sufficient to cause lysis in this area, as indicated by the red colour and the absence of bound platelets at the surface of the ILT. The lower values of shear stress over the rest of the thrombus indicate that lysis is not occurring anywhere else. This indicates that a vortex can cause local lysis even when overall flow is too low to cause widespread lysis. It also demonstrates a clear link between the haemodynamic environment and dynamic re-modelling the thrombus boundary.

But what about the influence of haemodynamics, and specifically vortices, on the biochemical environment? The following Figure 65 shows thrombin concentration at 25.5 seconds. The vortex marked “x” in Figure 62 is having a clear influence on the distribution of thrombin outside the ILT. The rotational flow drags the thrombin away from the region of generation and creating a region of high concentration at the centre of the vortex. Note the similarity to Figure 20 from Biasetti’s [75] simulation of thrombin movement in identical geometry.

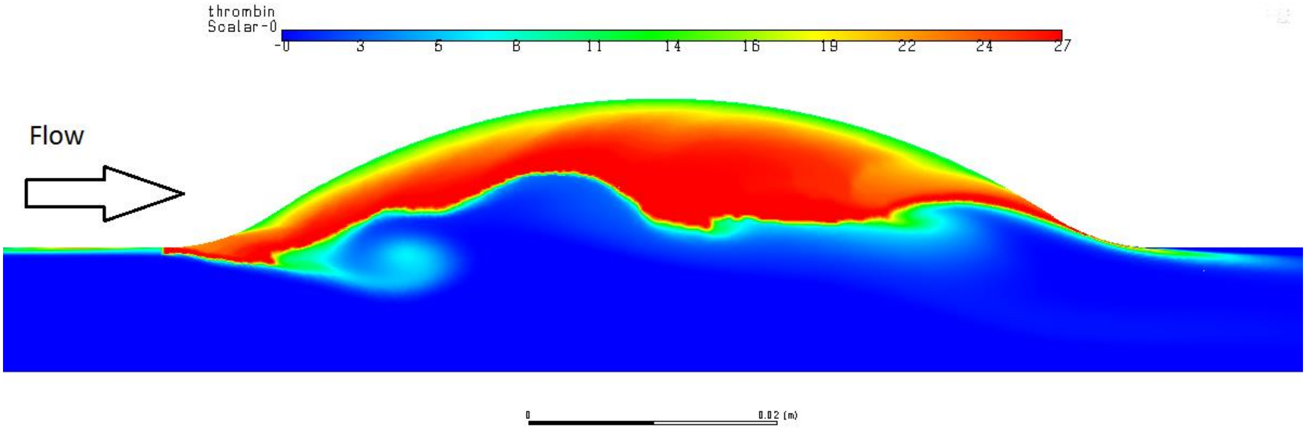

Figure 65 - Contours of thrombin concentration at 25.5 seconds

A similar effect is shown for the distribution of fibrin in Figure 66. A region of high fibrin concentration to the left of the vortex is leading to the growth of a small protrusion. If the vortex was stationary, this local growth would likely cause the ILT to form a concave boundary concentric with the vortex and tangential to the rotational flow. As we shall see at the next time step, the rapid distal movement of the vortex puts an end to the noticeable growth of this protrusion.

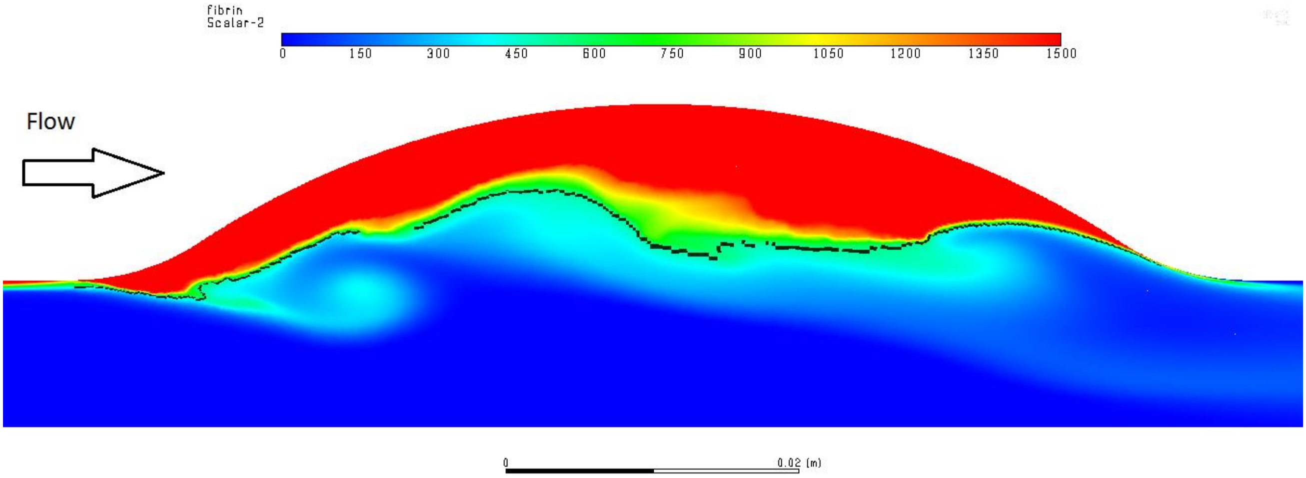

Figure 66 - Contours of fibrin concentration at 25.5 seconds

3.3.2 Point 5: Flow time = 25.64 s

During the brief period of reverse flow at the end of systole, the aorta and aneurysm show interesting flow patterns. Regions of recirculation emerge at multiple locations, most notably within the aneurysm sac where the vortex “x” expands to form a large rotating flow structure.

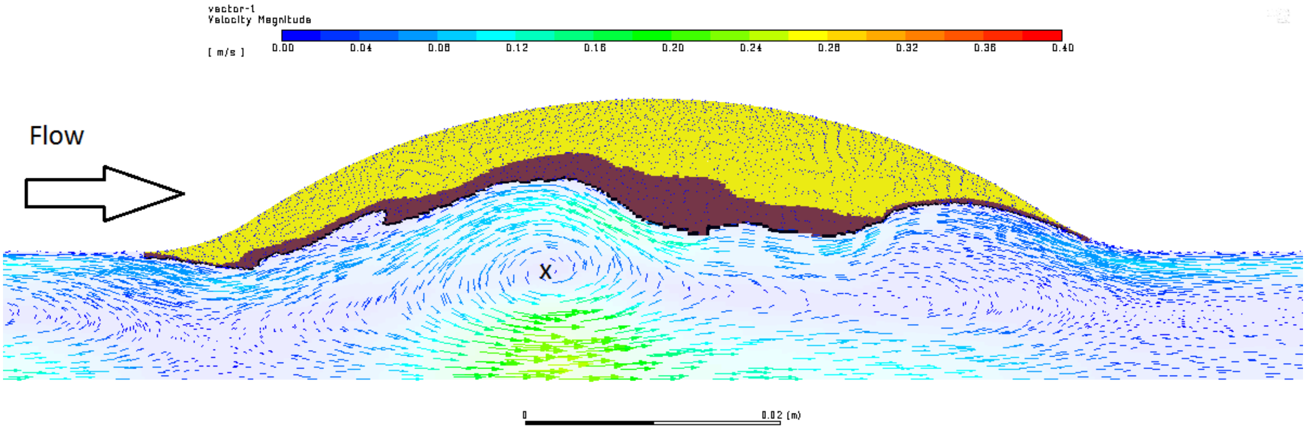

Figure 67 - ILT region and velocity vectors for strategy B at 25.64 seconds

A plot of vorticity shows the new location of vortex “x” close to the centre of the image. It should be noted that due to the axisymmetric assumption within the fluid model, this 2D Figure 68 represents a slice through one side of a toroidal vortex.

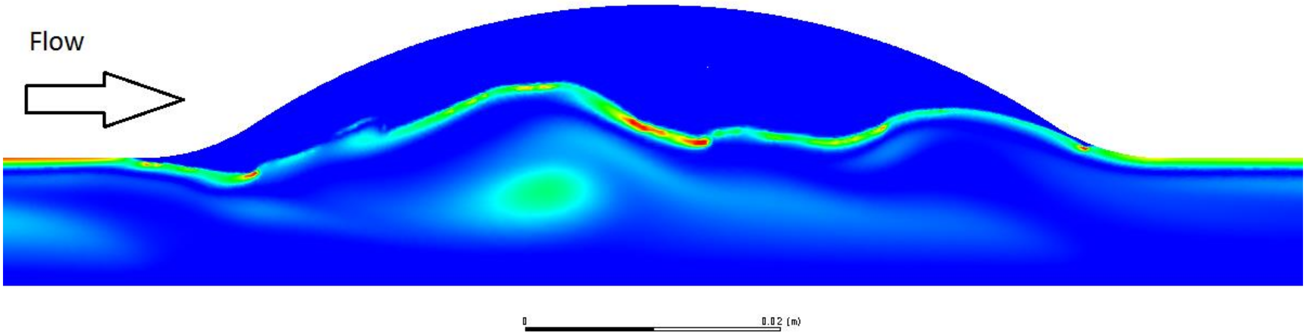

Figure 68 - Vorticity magnitude for strategy B at 25.64 seconds

The region of high thrombin concentration has moved with the vortex away from the ILT boundary as shown in Figure 69.

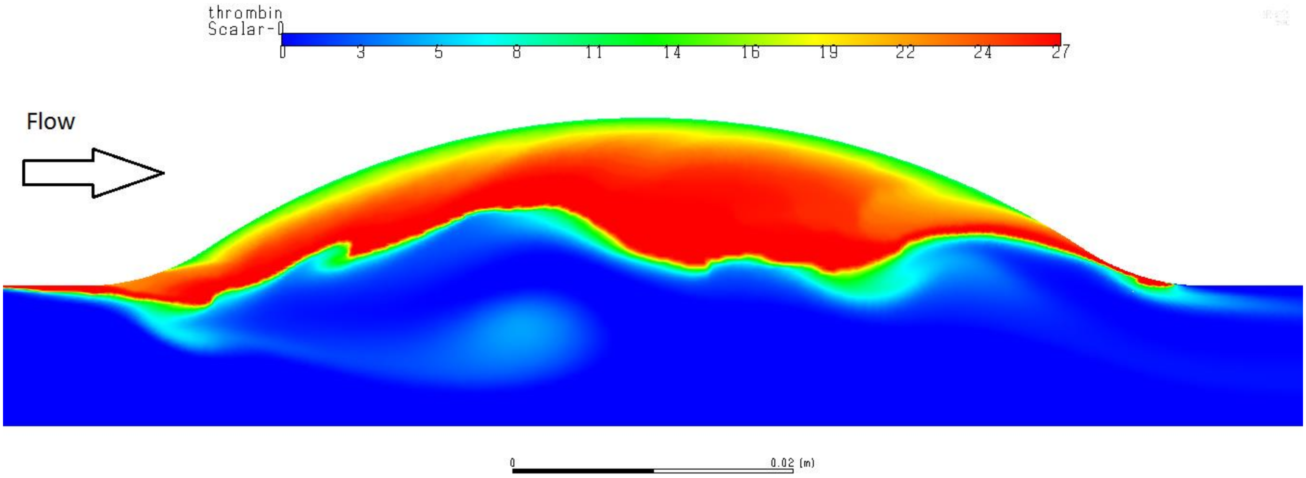

Figure 69 - Contours of thrombin concentration at 25.64 seconds

Fibrin distribution is shown in Figure 70 below. The vortex “x” has carried a pocket of high concentration towards the central axis, however, smaller vortexes and flow paths are creating zones of fibrin concentration close to the ILT boundary. These regions of high concentration will translate to regions of rapid clot growth during the diastolic period. This effect will become evident by comparison of the thrombus boundary at this time step and the next.

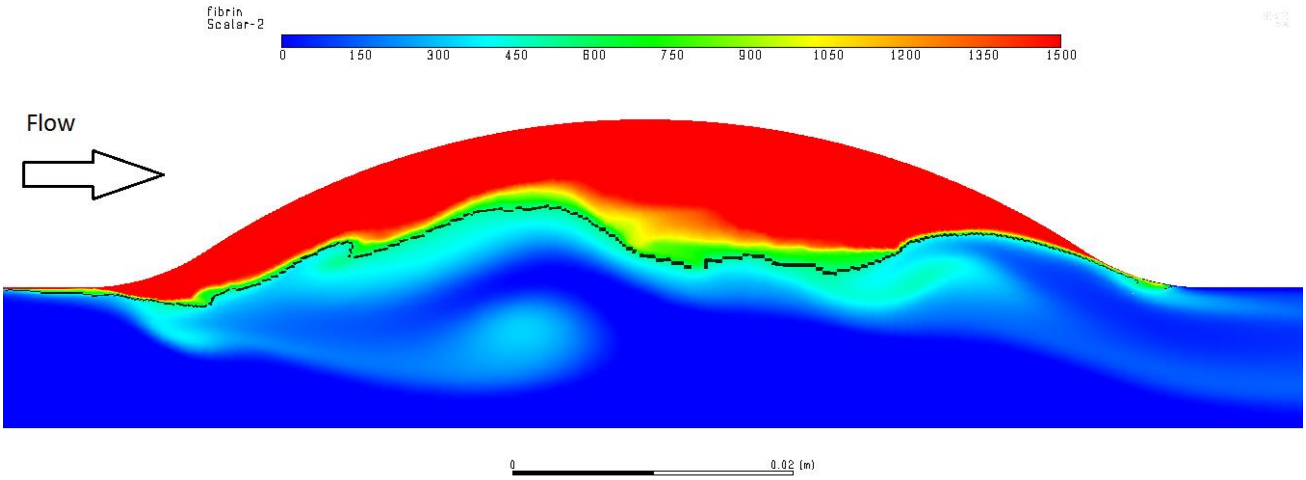

Figure 70 - Contours of fibrin concentration at 25.64 seconds

No lysis was occurring at this moment due to low shear at the ILT boundary, therefore a shear stress plot has been omitted.

3.3.3 Point 6: Flow time = 26.11s

The following images show conditions at late diastole, a time when bulk flow velocity is close to zero and thrombus growth rate is high. Regions of most notable growth are indicated by black circles in Figure 71 below. These regions correspond to zones of high fibrin concentration near the boundary of the ILT which are visible in Figure 70.

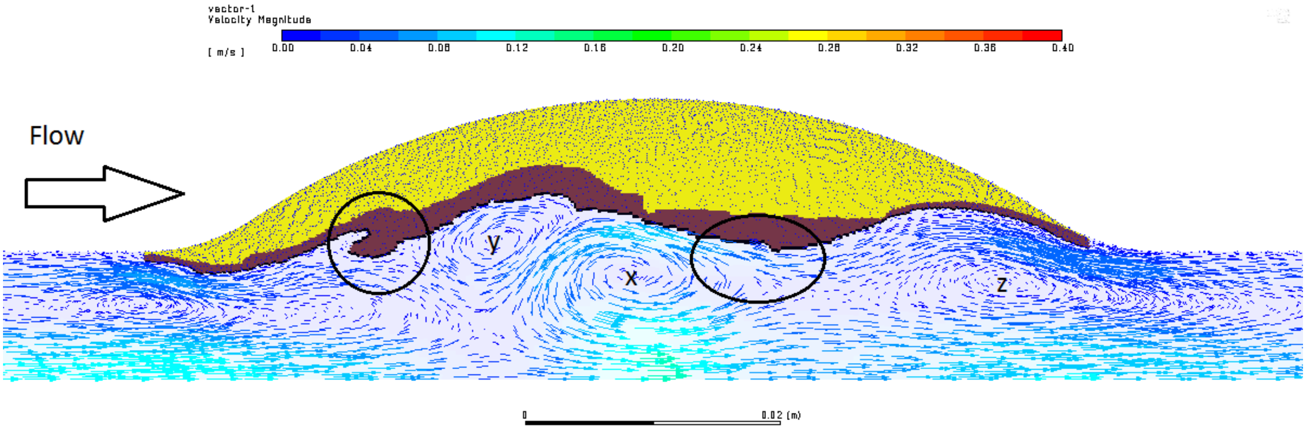

Figure 71 - ILT region and velocity vectors for strategy B at 26.11 seconds

The vortex "x" is still visible, however, the magnitude of the vorticity has reduced and various secondary vortexes "y" and "z" have emerged within the aneurysm. Note that vortex "x" has moved slightly downstream from its previous position. Within 0.1 seconds the acceleration from the systolic pulse will lead to smooth flow lines, and all these vortices will vanish. This indicates that the transport and lysis effects of the primary vortex "x" are limited to the distal half of the aneurysm sac in this simulation. If the period between one systole and the next was altered, the magnitude and positions of all three vortices at the end of diastole would be different, with consequent effects on thrombus growth rate and shape.

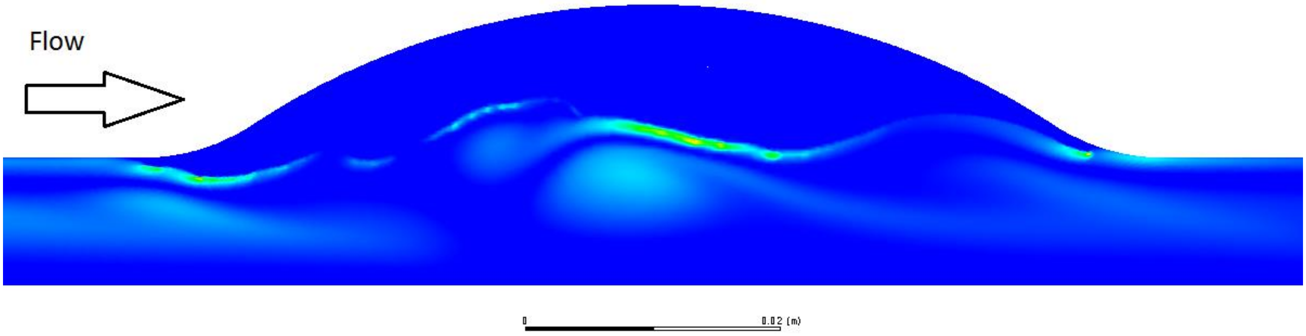

Figure 72 - Vorticity magnitude for strategy B at 26.11 seconds

The following figure shows the distribution of thrombin concentration. The combined effect of vortices “x” and “y” are generating noticeable flow of thrombin into the blood stream in the mid-distal region of the aneurysm sac. Convection of thrombin with flow was minimal with strategy A, however it is clearly evident with strategy B. This is desirable from the point of view of connecting haemodynamics to the biochemical clotting model. The following figure does, however, demonstrate a weakness in the implementation of this strategy in the current model. The region indicated with a black oval has emerged as a thrombus shell region during the last diastole, a period of roughly half a second. This protrusion will likely be removed by thrombolysis during the next systole, however this rapid local growth represents an anomaly which is not likely to occur in the human body.

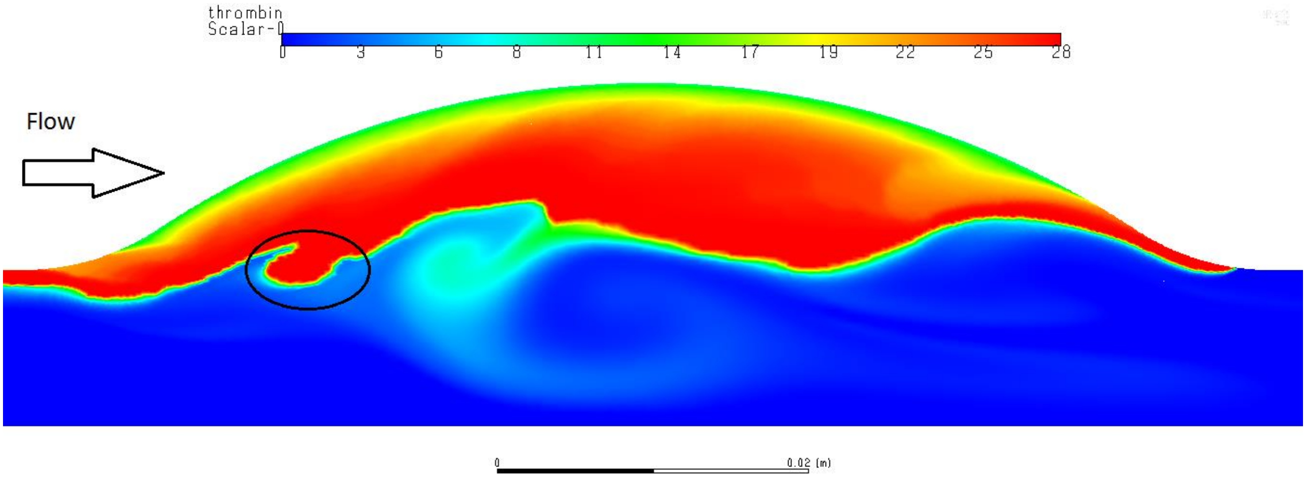

Figure 73 - Contours of thrombin concentration at 26.11 seconds

The following figure shows that the protrusion in question has emerged because a large region of fluid has reached the sufficient fibrin concentration of 600nM/L almost simultaneously. This begins to explain the self-accelerating mechanism that has led to this unusual local growth. A detailed description follows in the next paragraph.

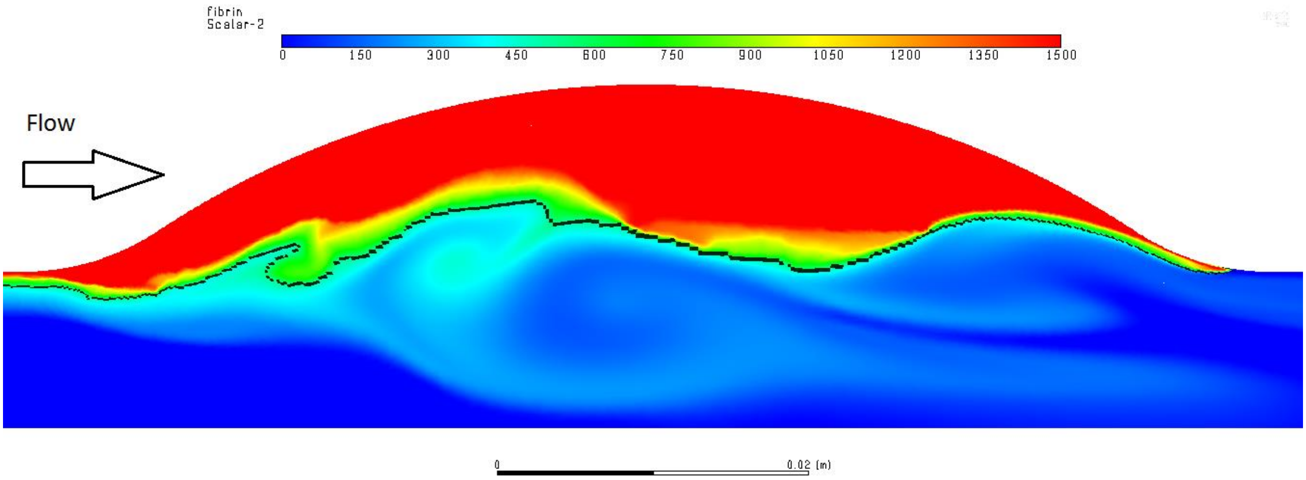

Figure 74 - Contours of fibrin concentration at 26.11 seconds

It has been shown in previous figures that irregular boundary geometry and/or flow vortices can create regions of high fibrin concentration outside the thrombus boundary. In reality this would lead to thrombus growth as the fibrin monomers join into fibrils and then create a mesh structure within or over the bound platelet layer. This process would proceed at some rate limited by the number of available platelets, level of platelet activation, and fibrin polymerisation time. The present model does not include the effect of these physiological constraints, instead growth rate is limited by a crude estimation inherent within the computational model. After each time step, the thrombus boundary can only expand into the bound platelet layer, shown in black above. This layer is never more than one computational cell thick, therefore growth rate is limited to the thickness of said cell per time step. A typical cell in this region shown above is 0.2mm, and during early diastole the time step size is 0.08 seconds. If shear-based thrombolysis and availability of fibrin are not limiting factors, this leads to a hypothetical growth rate of 2.5 mm/s.

This explains the potential for rapid growth, however the application of the thrombin generation model makes this occurrence more likely and leads to the accelerated growth of protrusions like that seen above. The aim of strategy B was to represent a band of thrombin generation limited by the overlap of prothrombin and prothrombinase as described by Leiderman and Fogelson [60]. If the thrombus boundary grew rapidly, the zone of overlap should narrow or cease to exist, and thrombin will no longer be generated. The strategy B model has the opposite response. As the thrombus grows, the generation region grows with it, leading to a greater quantity of thrombin in the region and high concentrations at the growing boundary. This high concentration catalyses the generation of fibrin which in turn causes the thrombus to grow more - and so the cycle continues. This self-accelerating feedback loop is the cause of local growth rates rising rapidly to their maximum possible value.

3.3.4 Point 7: Flow time = 30.0 seconds

Ultimately the ILT grows to fill the aneurysm sac and then continues to grow into the vessel lumen. This causes a stenosis of the vessel which reduces the effective area in which fluid blood can flow. This restriction leads to higher velocities adjacent to the aneurysm boundary and consequently higher shear stress. At this point the growth patterns of the thrombus change. Previously rotating vortices generated concave surfaces and protrusions, but now the flow is non-rotational and the boundary of the thrombus is smooth and parallel to the flow.

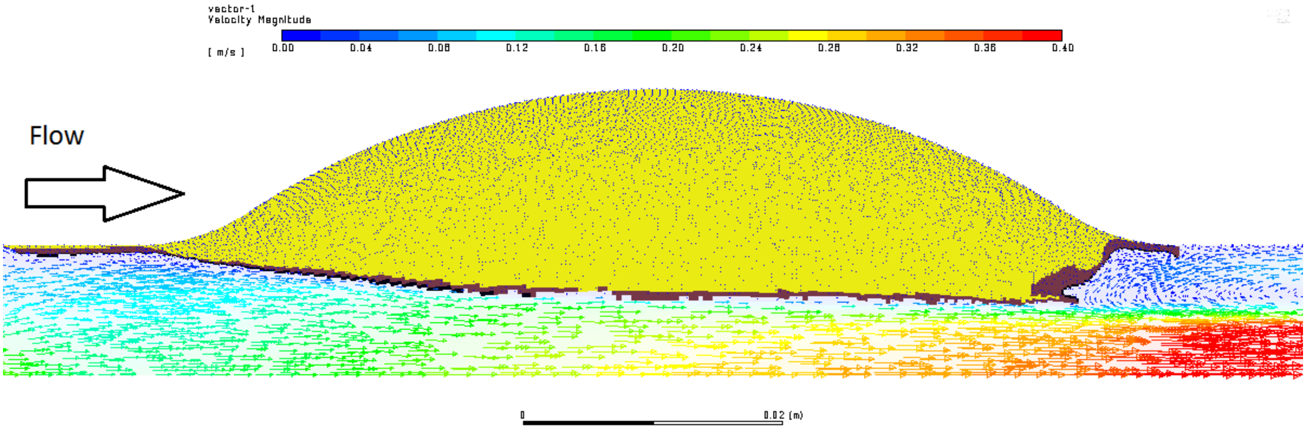

Figure 75 - ILT region and velocity vectors for strategy B at 30 seconds

The high shear stress due to stenosis leads to widespread thrombolysis over most of the aneurysm boundary, especially where protrusions were evident. This leads to the smoothing of the aneurysm surface and also the effective cessation of growth. The thrombus shell expands and contracts slightly during diastole and systole, but the competing effects of growth and lysis are balanced over the course of a heartbeat. A final point to note is the core dominates the volume of the thrombus, and the shell has become a thin layer of 1 or 2 cells. A plot of shear stress is shown in Figure 76 below.

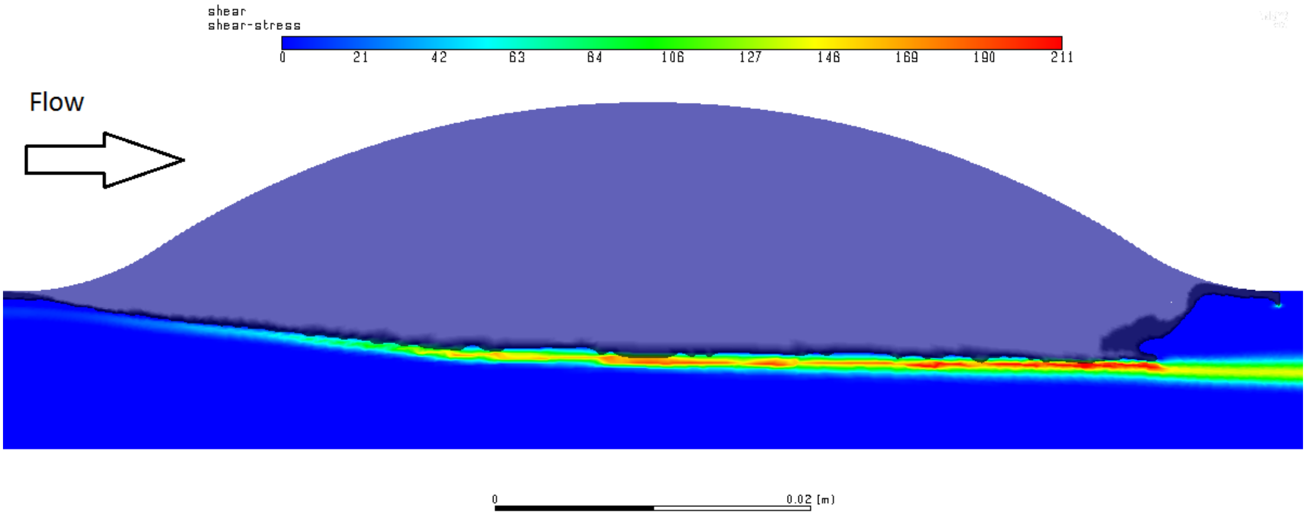

Figure 76 - Shear stress at ILT boundary causing widespread lysis at 30 seconds

4 Discussion

In this paper, a computational model has been introduced for simulating the growth of an ILT within an aortic aneurysm. The model combines the kinetics of the fibrinogen to fibrin reaction with a continuum model describing the fluid dynamics of the blood. Special attention has been given to fluid and chemical boundary conditions in order to enhance accuracy and create opportunities to include patient specific data. The ILT was treated as a porous zone in which intra-thrombus flow was hindered by variations in permeability. The commercial fluid dynamics solver ANSYS Fluent has been used for all simulation and visualisation. Mesh independence was confirmed with regard to the transient fluid flow, but not for the thrombus growth model. The solver was optimised for speed by testing for the optimum pressure-velocity coupling and pressure interpolation schemes. Overall simulation time was minimised by using a custom adaptive time stepping scheme and high-performance computing.

Two strategies for applying a source of thrombin were tested, and the results showed that the thrombus boundary is far more effective as a zone for thrombin generation than the aneurysm wall. By using this strategy, an ILT exhibiting various spatio-temporal features consistent with human physiology was generated. Firstly, the thrombus grew until complete occlusion of the aneurysm sac, but not occlusion of the aorta itself. The maximum size caused slight stenosis of the vessel which is observed in some cases. Secondly, the thrombus exhibited core and shell morphology during growth which was similar to diagrams provided in other papers and similar to the results of other simulations [71], [77], [89]. The shell layer was removed by thrombolysis once the ILT encroached on the vessel lumen, leaving a dense core region as described by Tosenberger [43]. Thirdly, the boundary of the ILT during growth showed a dynamic response to the haemodynamic environment. Transport of chemicals by convection and thrombolysis by high shear stress played a significant role in shaping and re-shaping the ILT over time. Flow vortices within the aneurysm sac proved to have a significant effect on these processes, and they appear to be the key influencers of thrombus shape prior to full occlusion. The timing, size and position of these vortices showed close similarity to those generated by Biasetti [75] in identical geometry as demonstrated by the similarity between Figure 20 and Figure 65. Finally, the simulated thrombus showed a trend of larger ILT thickness in the distal compared to the proximal region. This effect was noticeable both before and after aneurysm occlusion, and confirms findings by Biasetti [75].

This simulation can be used in its current form, or with some modification, to answer questions of interest to clinicians, engineers and biologists. One example would be to identify the regions of high risk for thrombosis growth around a medical device or surgical implant such as an artificial heart valve or endovascular graft. Another example would be to investigate the impact of variables such as heart rate or Endogenous thrombin potential (ETP) on the thrombus growth rate, morphology and size. However, before the model is put to use, certain limitations need to be understood or overcome – these limitations are discussed in the next paragraphs.

The major flaw with the model is the surprisingly high growth rates which emerged under certain conditions. This effect occurred only in certain locations and at certain times, however it has the potential to undermine the accuracy of simulated thrombus size and growth rate. A modification to limit this self-accelerating growth mechanism is recommended before final validation and use of the model.

One means to achieve this would be to slow growth everywhere by incorporating a simple time delay in the conversion from fluid to thrombus. Another addition which would slow growth indirectly, and conform the model closer to actual physiology, is to switch off thrombin generation for a period after the thrombus boundary has advanced. This would approximate the time for prothrombinase to diffuse from within the clot to the new boundary position. Finally, platelets could be included as an explicit substance within the flow. A minimum concentration of bound platelets could be included as a necessary requirement in the current thrombus growth model without much difficulty. By limiting the rate of platelet activation and binding, the overall thrombus growth rate would be limited based on sound physiological phenomena.

A more general concern is the unclear connection between the changing thrombin concentration and the thrombus growth rate. With strategy A, growth rate slowed even as thrombin concentration increased, a counterintuitive response which implies a lack of coupling between the two. With strategy B growth rate did increase with thrombin concentration, though it is not clear whether this was due to coupling or the anomalous growth mechanism described above. Given that the ILT had ceased growing and was already high in fibrin concentration before the peak of the TG curve, it is reasonable to assume that subsequent increase or decrease of thrombin levels would have no effect on the thrombus shape or size.

This implies that a close analysis of the fibrin reaction kinetics is recommended. With strategy B, fibrin generation was sufficient to grow the thrombus even when thrombin concentration was a tenth of its peak value. This could indicate that the Michaelis-Menten reaction was too sensitive to thrombin, or that the variables defining the TG curve were poorly scaled. Given the variability between results of CAT tests, calibration of the fibrin generation model based on TG results from a specific clinical context is recommended before use in said context.

The major findings to come out of the creation of the model presented here are as follows. Firstly it is possible to generate ILTs with reasonably accurate overall shape and morphology without explicitly modelling the entire coagulation cascade. A thrombin to Fibrin model was shown to be sufficient for this purpose, however the selection of a suitable range for thrombin concentration is vital to generate accurate growth rates. Secondly, it was shown that the aneurysm wall is not as effective as the thrombus boundary as a site for thrombin generation. Even without hindered diffusion, the slow transport of thrombin led to a decrease in growth rate as thrombus thickness increased. This led to early cessation and insensitivity to the flow environment. Thrombin generation at the boundary, by contrast, led to rapid and continual growth and a dynamic response to the flow environment.

In conclusion, the model presented here shows promise for the modelling of ILT in AAAs. Given the observed growth rates, the model at present is best suited to the types of ILT which grow within hours after surgery or injury, however, with modifications to the time advancing and thrombin release strategies, it could be used to model medium term growth over multiple days or weeks. It is suggested that the addition of a platelet activation and adhesion model would improve the accuracy of the model and correct the flaw in the thrombosis model which led to some regions of self-accelerating growth. It is hoped that the findings from this model will contribute to the understanding of this pathology and be of use to other researchers in the field.

5 References

[1] U. K. A. Sampson *et al.*, “Estimation of global and regional incidence and prevalence of abdominal aortic aneurysms 1990 to 2010,” *Global Heart*. 2014, doi: 10.1016/j.gheart.2013.12.009.

[2] A. Arzani, G. Y. Suh, R. L. Dalman, and S. C. Shadden, “A longitudinal comparison of hemodynamics and intraluminal thrombus deposition in abdominal aortic aneurysms,” *Am. J. Physiol. - Hear. Circ. Physiol.*, 2014, doi: 10.1152/ajpheart.00461.2014.

[3] J. C. Lasheras, “The Biomechanics of Arterial Aneurysms,” *Annu. Rev. Fluid Mech.*, 2007, doi: 10.1146/annurev.fluid.39.050905.110128.

[4] P. Di Achille, G. Tellides, C. A. Figueroa, and J. D. Humphrey, “A haemodynamic predictor of intraluminal thrombus formation in abdominal aortic aneurysms,” *Proc. R. Soc. A Math. Phys. Eng. Sci.*, 2014, doi: 10.1098/rspa.2014.0163.

[5] L. Virag, J. S. Wilson, J. D. Humphrey, and I. Karšaj, “A Computational Model of Biochemomechanical Effects of Intraluminal Thrombus on the Enlargement of Abdominal Aortic Aneurysms,” *Ann. Biomed. Eng.*, 2015, doi: 10.1007/s10439-015-1354-z.

[6] F. Joly, G. Soulez, D. Garcia, S. Lessard, and C. Kauffmann, “Flow stagnation volume and abdominal aortic aneurysm growth: Insights from patient-specific computational flow dynamics of Lagrangian-coherent structures,” *Comput. Biol. Med.*, 2018, doi: 10.1016/j.compbiomed.2017.10.033.

[7] K. C. Kent *et al.*, “Analysis of risk factors for abdominal aortic aneurysm in a cohort of more than 3 million individuals,” *J. Vasc. Surg.*, 2010, doi: 10.1016/j.jvs.2010.05.090.

[8] N. Sakalihasan, R. Limet, and O. D. Defawe, “Abdominal aortic aneurysm,” *Lancet*. 2005, doi: 10.1016/S0140-6736(05)66459-8.

[9] D. A. Vorp, “Biomechanics of abdominal aortic aneurysm,” *Journal of Biomechanics*. 2007, doi: 10.1016/j.jbiomech.2006.09.003.

[10] P. M. Brown, D. T. Zelt, B. Sobolev, J. W. Hallett, and Y. Sternbach, “The risk of rupture in untreated aneurysms: The impact of size, gender, and expansion rate,” *J. Vasc. Surg.*, 2003, doi: 10.1067/mva.2003.119.

[11] M. F. Fillinger, S. P. Marra, M. L. Raghavan, and F. E. Kennedy, “Prediction of rupture risk in abdominal aortic aneurysm during observation: Wall stress versus diameter,” *J. Vasc. Surg.*, 2003, doi: 10.1067/mva.2003.213.

[12] J. Lindholt, S. Vammen, H. Fasting, E. Henneberg, and L. Heickendorff, “The plasma level of matrix metalloproteinase 9 may predict the natural history of small abdominal aortic aneurysms. A preliminary study,” *Eur. J. Vasc. Endovasc. Surg.*, 2000, doi: 10.1053/ejvs.2000.1151.

[13] W. D. McMillan *et al.*, “Increased plasma levels of metalloproteinase-9 are associated with abdominal aortic aneurysms,” *J. Vasc. Surg.*, 1999, doi: 10.1016/S0741-5214(99)70363-0.

[14] L. Karlsson, D. Bergqvist, J. Lindbäck, and H. Pärsson, “Expansion of Small-diameter

Abdominal Aortic Aneurysms is Not Reflected by the Release of Inflammatory Mediators IL-6, MMP-9 and CRP in Plasma," *Eur. J. Vasc. Endovasc. Surg.*, 2009, doi: 10.1016/j.ejvs.2008.11.027.

[15] S. R. Vallabhaneni, G. L. Gilling-Smith, T. V. How, S. D. Carter, J. A. Brennan, and P. L. Harris, "Heterogeneity of tensile strength and matrix metalloproteinase activity in the wall of abdominal aortic aneurysms," *J. Endovasc. Ther.*, 2004, doi: 10.1583/04-1239.1.

[16] J. S. Wilson, L. Virag, P. Di Achille, I. Karšaj, and J. D. Humphrey, "Biochemomechanics of intraluminal thrombus in abdominal aortic aneurysms," *Journal of Biomechanical Engineering*. 2013, doi: 10.1115/1.4023437.

[17] A. K. Venkatasubramaniam *et al.*, "A comparative study of aortic wall stress using finite element analysis for ruptured and non-ruptured abdominal aortic aneurysms," *Eur. J. Vasc. Endovasc. Surg.*, 2004, doi: 10.1016/j.ejvs.2004.03.029.

[18] G. Mhlanga, "A retrospective audit into the morbidity and mortality of open abdominal aortic aneurysm repair at Groote Schuur Hospital, Cape Town," University of Cape Town, 2017.

[19] R. M. Greenhalgh, "Comparison of endovascular aneurysm repair with open repair in patients with abdominal aortic aneurysm (EVAR trial 1), 30-day operative mortality results: Randomised controlled trial," *Lancet*, 2004, doi: 10.1016/S0140-6736(04)16979-1.

[20] Stanford health care, "Abdominal Aortic Aneurysm Open Repair." [Online]. Available: https://stanfordhealthcare.org/medical-conditions/blood-heart-circulation/abdominal-aortic-aneurysm/treatments/abdominal-aortic-aneurysm-open-repair.html. [Accessed: 01-Feb-2020].

[21] C. A. Taylor and M. T. Draney, "EXPERIMENTAL AND COMPUTATIONAL METHODS IN CARDIOVASCULAR FLUID MECHANICS," *Annu. Rev. Fluid Mech.*, 2004, doi: 10.1146/annurev.fluid.36.050802.121944.

[22] S. Roccabianca, C. A. Figueroa, G. Tellides, and J. D. Humphrey, "Quantification of regional differences in aortic stiffness in the aging human," *J. Mech. Behav. Biomed. Mater.*, 2014, doi: 10.1016/j.jmbbm.2013.01.026.

[23] Blausen.com staff, "Medical gallery of Blausen Medical 2014." [Online]. Available: https://en.wikiversity.org/wiki/WikiJournal_of_Medicine/Medical_gallery_of_Blausen_Medical_2014. [Accessed: 01-Feb-2020].

[24] J. P. Vande Geest, M. S. Sacks, and D. A. Vorp, "The effects of aneurysm on the biaxial mechanical behavior of human abdominal aorta," *J. Biomech.*, 2006, doi: 10.1016/j.jbiomech.2005.03.003.

[25] A. Wills, M. M. Thompson, M. Crowther, R. D. Sayers, and P. R. F. Bell, "Pathogenesis of abdominal aortic aneurysms - Cellular and biochemical mechanisms," *European Journal of Vascular and Endovascular Surgery*. 1996, doi: 10.1016/S1078-5884(96)80002-5.

[26] D. A. Vorp *et al.*, "Association of intraluminal thrombus in abdominal aortic aneurysm with local hypoxia and wall weakening," *J. Vasc. Surg.*, 2001, doi: 10.1067/mva.2001.114813.

[27] D. H. J. Wang, M. S. Makaroun, M. W. Webster, and D. A. Vorp, "Effect of intraluminal thrombus on wall stress in patient-specific models of abdominal aortic aneurysm," *J.*

Vasc. Surg., 2002, doi: 10.1067/mva.2002.126087.

[28] S. Sorrentino, “Radiopedia,” 2011. [Online]. Available: https://radiopaedia.org/cases/abdominal-aortic-aneurysm-35?lang=us. [Accessed: 01-Feb-2020].

[29] J. Clauser *et al.*, “A Novel Plasma-Based Fluid for Particle Image Velocimetry (PIV): In-Vitro Feasibility Study of Flow Diverter Effects in Aneurysm Model,” *Ann. Biomed. Eng.*, 2018, doi: 10.1007/s10439-018-2002-1.

[30] D. M. Sforza, C. M. Putman, and J. R. Cebral, “Hemodynamics of Cerebral Aneurysms,” *Annu. Rev. Fluid Mech.*, 2009, doi: 10.1146/annurev.fluid.40.111406.102126.

[31] F. Swieringa *et al.*, “Platelet Control of Fibrin Distribution and Microelasticity in Thrombus Formation under Flow,” *Arterioscler. Thromb. Vasc. Biol.*, 2016, doi: 10.1161/ATVBAHA.115.306537.

[32] N. M. Dashkevich *et al.*, “Thrombin activity propagates in space during blood coagulation as an excitation wave,” *Biophys. J.*, 2012, doi: 10.1016/j.bpj.2012.10.011.

[33] D. A. Andrews and P. S. Low, “Role of red blood cells in thrombosis,” *Current Opinion in Hematology*. 1999, doi: 10.1097/00062752-199903000-00004.

[34] S. Kattula, J. R. Byrnes, and A. S. Wolberg, “Fibrinogen and Fibrin in Hemostasis and Thrombosis,” *Arteriosclerosis, Thrombosis, and Vascular Biology*. 2017, doi: 10.1161/ATVBAHA.117.308564.

[35] F. Storti, T. H. S. van Kempen, and F. N. van de Vosse, “A continuum model for platelet plug formation and growth,” *Int. j. numer. method. biomed. eng.*, 2014, doi: 10.1002/cnm.2623.

[36] M. Bryckaert, J. P. Rosa, C. V. Denis, and P. J. Lenting, “Of von Willebrand factor and platelets,” *Cellular and Molecular Life Sciences*. 2015, doi: 10.1007/s00018-014-1743-8.

[37] M. Anand, K. Rajagopal, and K. R. Rajagopal, “A model for the formation and lysis of blood clots,” *Pathophysiol. Haemost. Thromb.*, 2006, doi: 10.1159/000089931.

[38] T. Bodnár and A. Sequeira, “Numerical simulation of the coagulation dynamics of blood,” *Comput. Math. Methods Med.*, 2008, doi: 10.1080/17486700701852784.

[39] M. N. Ngoepe, A. F. Frangi, J. V. Byrne, and Y. Ventikos, “Thrombosis in cerebral aneurysms and the computational modeling thereof: A review,” *Frontiers in Physiology*. 2018, doi: 10.3389/fphys.2018.00306.

[40] N. Mackman, R. E. Tilley, and N. S. Key, “Role of the extrinsic pathway of blood coagulation in hemostasis and thrombosis,” *Arteriosclerosis, Thrombosis, and Vascular Biology*. 2007, doi: 10.1161/ATVBAHA.107.141911.

[41] K. B. Neeves, D. A. R. Illing, and S. L. Diamond, “Thrombin flux and wall shear rate regulate fibrin fiber deposition state during polymerization under flow,” *Biophys. J.*, 2010, doi: 10.1016/j.bpj.2009.12.4275.

[42] Z. M. Ruggeri, “Mechanisms of shear-induced platelet adhesion and aggregation,” *Thrombosis and Haemostasis*. 1993, doi: 10.1055/s-0038-1646171.

[43] A. Tosenberger, F. Ataullakhanov, N. Bessonov, M. Panteleev, A. Tokarev, and V.

Volpert, “Modelling of platelet–fibrin clot formation in flow with a DPD–PDE method,” *J. Math. Biol.*, vol. 72, no. 3, pp. 649–681, Feb. 2016, doi: 10.1007/s00285-015-0891-2.

[44] A. N. Sveshnikova, A. V. Belyaev, M. A. Panteleev, and D. Y. Nechipurenko, “The Role of Transmembrane Glycoproteins, Integrins and Serpentines in Platelet Adhesion and Activation,” *Biochemistry (Moscow) Supplement Series A: Membrane and Cell Biology*. 2018, doi: 10.1134/S1990747818050070.

[45] T. Lisman, C. Weeterings, and P. G. De Groot, “Platelet aggregation: Involvement of thrombin and fibrin(ogen),” *Front. Biosci.*, 2005, doi: 10.2741/1715.

[46] K. Ouriel *et al.*, “The hemodynamics of thrombus formation in arteries,” *J. Vasc. Surg.*, 1991, doi: 10.1067/mva.1991.33157.

[47] M. J. O’Rourke, J. P. McCullough, and S. Kelly, “An investigation of the relationship between hemodynamics and thrombus deposition within patient-specific models of abdominal aortic aneurysm,” *Proc. Inst. Mech. Eng. Part H J. Eng. Med.*, 2012, doi: 10.1177/0954411912444080.

[48] V. L. Rayz *et al.*, “Numerical modeling of the flow in intracranial aneurysms: Prediction of regions prone to thrombus formation,” *Ann. Biomed. Eng.*, 2008, doi: 10.1007/s10439-008-9561-5.

[49] B. A. Zambrano *et al.*, “Association of Intraluminal Thrombus, Hemodynamic Forces, and Abdominal Aortic Aneurysm Expansion Using Longitudinal CT Images,” *Ann. Biomed. Eng.*, 2016, doi: 10.1007/s10439-015-1461-x.

[50] A. A. Onasoga-Jarvis, T. J. Puls, S. K. O’Brien, L. Kuang, H. J. Liang, and K. B. Neeves, “Thrombin generation and fibrin formation under flow on biomimetic tissue factor-rich surfaces,” *J. Thromb. Haemost.*, 2014, doi: 10.1111/jth.12491.

[51] B. Savage, M. Cattaneo, and Z. M. Ruggeri, “Mechanisms of platelet aggregation,” *Current Opinion in Hematology*. 2001, doi: 10.1097/00062752-200109000-00002.

[52] M. J. Slepian *et al.*, “Shear-mediated platelet activation in the free flow: Perspectives on the emerging spectrum of cell mechanobiological mechanisms mediating cardiovascular implant thrombosis,” *J. Biomech.*, 2017, doi: 10.1016/j.jbiomech.2016.11.016.

[53] L. F. Brass, “Thrombin and platelet activation,” *Chest*, 2003, doi: 10.1378/chest.124.3_suppl.18S.

[54] G. E. Jarvis, “Platelet Aggregation in Whole Blood,” in *Platelets and Megakaryocytes: Volume 1: Functional Assays*, J. M. Gibbins and M. P. Mahaut-Smith, Eds. Totowa, NJ: Humana Press, 2004, pp. 77–87.

[55] Wikimedia Commons, “Coagulation with arrows for negative and positive feedback.,” 2007. [Online]. Available: https://en.wikipedia.org/wiki/Coagulation#/media/File:Coagulation_full.svg. [Accessed: 02-Feb-2020].

[56] H. H. Versteeg, J. W. M. Heemskerk, M. Levi, and P. H. Reitsma, “New Fundamentals in hemostasis,” *Physiological Reviews*. 2013, doi: 10.1152/physrev.00016.2011.

[57] M. Hoffman, “A cell-based model of coagulation and the role of factor VIIa,” in *Blood Reviews*, 2003, doi: 10.1016/S0268-960X(03)90000-2.

[58] T. Orfeo, S. Butenas, K. E. Brummel-Ziedins, and K. G. Mann, “The tissue factor requirement in blood coagulation,” *J. Biol. Chem.*, 2005, doi: 10.1074/jbc.M505506200.

[59] I. F. Obraztsov, Y. A. Barynin, and M. A. Khanin, “A mechanism for restriction of the activation-zone propagation for a hemostasis system (a mathematical model),” *Dokl. Phys.*, 2000, doi: 10.1134/1.1342454.

[60] K. Leiderman and A. L. Fogelson, “The Influence of Hindered Transport on the Development of Platelet Thrombi Under Flow,” *Bull. Math. Biol.*, 2013, doi: 10.1007/s11538-012-9784-3.

[61] M. Ninivaggi, R. Apitz-Castro, Y. Dargaud, B. De Laat, H. C. Hemker, and T. Lindhout, “Whole-blood thrombin generation monitored with a calibrated automated thrombogram-based assay,” *Clin. Chem.*, 2012, doi: 10.1373/clinchem.2012.184077.

[62] H. C. Hemker *et al.*, “The Calibrated Automated Thrombogram (CAT): A universal routine test for hyper- and hypocoagulability,” in *Pathophysiology of Haemostasis and Thrombosis*, 2002, doi: 10.1159/000073575.

[63] R. S. Voronov, T. J. Stalker, L. F. Brass, and S. L. Diamond, “Simulation of intrathrombus fluid and solute transport using in vivo clot structures with single platelet resolution,” *Ann. Biomed. Eng.*, 2013, doi: 10.1007/s10439-013-0764-z.

[64] A. V. Belyaev, J. L. Dunster, J. M. Gibbins, M. A. Panteleev, and V. Volpert, “Modeling thrombosis in silico: Frontiers, challenges, unresolved problems and milestones,” *Physics of Life Reviews*. 2018, doi: 10.1016/j.plrev.2018.02.005.

[65] A. S. Wolberg, “Thrombin generation and fibrin clot structure,” *Blood Rev.*, 2007, doi: 10.1016/j.blre.2006.11.001.

[66] B. Dahlbäck, “Blood coagulation,” *Lancet*. 2000, doi: 10.1016/S0140-6736(00)02225-X.

[67] Y. Chugh, B. Lau, and C. C. Taub, “Early post-operative coronary thrombosis following repair of a proximal coronary artery fistula,” *J. Clin. Diagnostic Res.*, 2016, doi: 10.7860/JCDR/2016/22368.9106.

[68] A. K. Ascoop and W. Budts, “Percutaneous closure of a congenital coronary artery fistula complicated by an acute myocardial infarction,” *Acta Cardiol.*, 2004, doi: 10.2143/AC.59.1.2005161.

[69] K. Tzirakis, Y. Kamarianakis, E. Metaxa, N. Kontopodis, C. V. Ioannou, and Y. Papaharilaou, “A robust approach for exploring hemodynamics and thrombus growth associations in abdominal aortic aneurysms,” *Med. Biol. Eng. Comput.*, 2017, doi: 10.1007/s11517-016-1610-x.

[70] W. T. Wu, M. A. Jamiolkowski, W. R. Wagner, N. Aubry, M. Massoudi, and J. F. Antaki, “Multi-Constituent Simulation of Thrombus Deposition,” *Sci. Rep.*, 2017, doi: 10.1038/srep42720.

[71] O. V. Kim, Z. Xu, E. D. Rosen, and M. S. Alber, “Fibrin Networks Regulate Protein Transport during Thrombus Development,” *PLoS Comput. Biol.*, 2013, doi: 10.1371/journal.pcbi.1003095.

[72] M. Sadowski, M. Zabczyk, and A. Undas, “Coronary thrombus composition: Links with inflammation, platelet and endothelial markers,” *Atherosclerosis*, 2014, doi: 10.1016/j.atherosclerosis.2014.10.020.

[73] J. Silvain *et al.*, “Composition of coronary thrombus in acute myocardial infarction,” *J. Am. Coll. Cardiol.*, 2011, doi: 10.1016/j.jacc.2010.09.077.

[74] M. N. Ngoepe and Y. Ventikos, “Computational modelling of clot development in patient-specific cerebral aneurysm cases,” *J. Thromb. Haemost.*, 2016, doi: 10.1111/jth.13220.

[75] J. Biasetti, P. G. Spazzini, J. Swedenborg, and T. Christian Gasser, “An integrated fluid-chemical model toward modeling the formation of intra-luminal thrombus in abdominal aortic aneurysms,” *Front. Physiol.*, 2012, doi: 10.3389/fphys.2012.00266.

[76] E. A. Finol and C. H. Amon, “Flow dynamics in anatomical models of abdominal aortic aneurysms: Computational analysis of pulsatile flow,” *Acta Cient. Venez.*, 2003.

[77] L. F. Brass and S. L. Diamond, “Transport physics and biorheology in the setting of hemostasis and thrombosis,” *Journal of Thrombosis and Haemostasis*. 2016, doi: 10.1111/jth.13280.

[78] K. Leiderman and A. L. Fogelson, “Grow with the flow: A spatial-temporal model of platelet deposition and blood coagulation under flow,” *Math. Med. Biol.*, 2011, doi: 10.1093/imammb/dqq005.

[79] Wikimedia Commons, “Michaelis-Menten kinetics.” [Online]. Available: https://en.wikipedia.org/wiki/Michaelis–Menten_kinetics. [Accessed: 02-Feb-2020].

[80] R. C. F. Duarte, C. N. Ferreira, D. R. A. Rios, H. J. dos Reis, and M. das G. Carvalho, “Thrombin generation assays for global evaluation of the hemostatic system: perspectives and limitations,” *Revista Brasileira de Hematologia e Hemoterapia*. 2017, doi: 10.1016/j.bjhh.2017.03.009.

[81] R. Loeffen *et al.*, “Associations between thrombin generation and the risk of cardiovascular disease in elderly patients: Results from the PROSPER Study,” *Journals Gerontol. - Ser. A Biol. Sci. Med. Sci.*, 2015, doi: 10.1093/gerona/glu228.

[82] M. Smid *et al.*, “Thrombin Generation in the Glasgow Myocardial Infarction Study,” *PLoS One*, 2013, doi: 10.1371/journal.pone.0066977.

[83] K. E. Brummel-Ziedins and A. S. Wolberg, “Global assays of hemostasis,” *Curr. Opin. Hematol.*, 2014, doi: 10.1097/MOH.0000000000000074.

[84] M. Tomaiuolo, T. J. Stalker, J. D. Welsh, S. L. Diamond, T. Sinno, and L. F. Brass, “A systems approach to hemostasis: 2. Computational analysis of molecular transport in the thrombus microenvironment.,” *Blood*, 2014, doi: 10.1182/blood-2014-01-550343.

[85] Z. Xu, N. Chen, M. M. Kamocka, E. D. Rosen, and M. Alber, “A multiscale model of thrombus development,” *J. R. Soc. Interface*, 2008, doi: 10.1098/rsif.2007.1202.

[86] V. Govindarajan, V. Rakesh, J. Reifman, and A. Y. Mitrophanov, “Computational Study of Thrombus Formation and Clotting Factor Effects under Venous Flow Conditions,” *Biophys. J.*, vol. 110, no. 8, pp. 1869–1885, Apr. 2016, doi: 10.1016/j.bpj.2016.03.010.

[87] D. E. Lacroix, “A reduced equation mathematical model for blood coagulation and lysis in quiescent plasma.,” *Int. J. Struct. Chang. solids - Mech. Appl.*, 2012.

[88] ANSYS Inc., “ANSYS FLUENT 12.0 User’s Guide - 7.2.3 Porous Media Conditions,” 2009. [Online]. Available: https://www.afs.enea.it/project/neptunius/docs/fluent/html/ug/node233.htm.

[Accessed: 24-Jan-2020].

[89] O. E. Kadri, V. D. Chandran, M. Surblyte, and R. S. Voronov, “In vivo measurement of blood clot mechanics from computational fluid dynamics based on intravital microscopy images,” *Comput. Biol. Med.*, 2019, doi: 10.1016/j.compbiomed.2019.01.001.

[90] A. R. Wufsus, N. E. MacEra, and K. B. Neeves, “The hydraulic permeability of blood clots as a function of fibrin and platelet density,” *Biophys. J.*, 2013, doi: 10.1016/j.bpj.2013.02.055.

[91] R. W. Muthard and S. L. Diamond, “Blood clots are rapidly assembled hemodynamic sensors: Flow arrest triggers intraluminal thrombus contraction,” *Arterioscler. Thromb. Vasc. Biol.*, 2012, doi: 10.1161/ATVBAHA.112.300312.

[92] P. Riha, X. Wang, R. Liao, and J. R. Stoltz, “Elasticity and fracture strain of whole blood clots,” *Clin. Hemorheol. Microcirc.*, 1999.

[93] T. V. Colace, R. W. Muthard, and S. L. Diamond, “Thrombus growth and embolism on tissue factor-bearing collagen surfaces under flow: Role of thrombin with and without fibrin,” *Arterioscler. Thromb. Vasc. Biol.*, 2012, doi: 10.1161/ATVBAHA.112.249789.

[94] C. J. Mills *et al.*, “Pressure-flow relationships and vascular impedance in man,” *Cardiovasc. Res.*, 1970, doi: 10.1093/cvr/4.4.405.

[95] J. E. Moore and D. N. Ku, “Pulsatile velocity measurements in a model of the human abdominal aorta under resting conditions,” *J. Biomech. Eng.*, 1994, doi: 10.1115/1.2895740.

[96] C. A. Taylor, T. J. R. Hughes, and C. K. Zarins, “Finite element modeling of three-dimensional pulsatile flow in the abdominal aorta: Relevance to atherosclerosis,” *Ann. Biomed. Eng.*, 1998, doi: 10.1114/1.140.

[97] J. R. Womersley, “Method for the calculation of velocity, rate of flow and viscous drag in arteries when the pressure gradient is known,” *J. Physiol.*, 1955, doi: 10.1113/jphysiol.1955.sp005276.

[98] M. K. Banerjee, R. Ganguly, and A. Datta, “Effect of Pulsatile Flow Waveform and Womersley Number on the Flow in Stenosed Arterial Geometry,” *ISRN Biomath.*, 2012, doi: 10.5402/2012/853056.

[99] R. Hellmuth, “Womersley Flow Profile,” 2017. [Online]. Available: https://commons.wikimedia.org/wiki/File:Womersley_Flow_Profile.svg. [Accessed: 03-Feb-2020].

[100] J. Lotz, C. Meier, A. Leppert, and M. Galanski, “Cardiovascular flow measurement with phase-contrast MR imaging: Basic facts and implementation,” *Radiographics*, 2002, doi: 10.1148/radiographics.22.3.g02ma11651.

[101] F. M. Callaghan *et al.*, “Use of multi-velocity encoding 4D flow MRI to improve quantification of flow patterns in the aorta,” *J. Magn. Reson. Imaging*, 2016, doi: 10.1002/jmri.24991.

[102] A. S. Les, J. J. Yeung, G. M. Schultz, R. J. Herfkens, R. L. Dalman, and C. A. Taylor, “Supraceliac and Infrarenal Aortic Flow in Patients with Abdominal Aortic Aneurysms: Mean Flows, Waveforms, and Allometric Scaling Relationships,” *Cardiovasc. Eng. Technol.*, 2010, doi: 10.1007/s13239-010-0004-8.

[103] H. H. Yeh, S. W. Rabkin, and D. Grecov, “Hemodynamic assessments of the ascending thoracic aortic aneurysm using fluid-structure interaction approach,” *Med. Biol. Eng. Comput.*, 2018, doi: 10.1007/s11517-017-1693-z.

[104] I. E. Vignon-Clementel, C. Alberto Figueroa, K. E. Jansen, and C. A. Taylor, “Outflow boundary conditions for three-dimensional finite element modeling of blood flow and pressure in arteries,” *Comput. Methods Appl. Mech. Eng.*, 2006, doi: 10.1016/j.cma.2005.04.014.

[105] ANSYS Inc., “18.1 Overview of Flow Solvers,” *ANSYS FLUENT 12.0 Theory Guide*, 2009. [Online]. Available: https://www.afs.enea.it/project/neptunius/docs/fluent/html/th/node360.htm. [Accessed: 04-Feb-2020].

[106] R. M. W. Kremers, B. de Laat, R. J. Wagenvoord, and H. C. Hemker, “Computational modelling of clot development in patient-specific cerebral aneurysm cases: comment,” *Journal of Thrombosis and Haemostasis*. 2017, doi: 10.1111/jth.13591.

[107] S. Bloemen, H. Kelchtermans, and H. C. Hemker, “Thrombin generation in low plasma volumes,” *Thrombosis Journal*, vol. 16, no. 1. BioMed Central Ltd., 15-May-2018, doi: 10.1186/s12959-018-0164-6.

[108] ANSYS inc., “ANSYS Meshing User’s Guide.” Canonsburg, PA, 2013.

[109] ANSYS Inc., “Chapter 22. Using the Solver,” *ANSYS FLUENT User’s Guide*, 2001. [Online]. Available: https://www.afs.enea.it/project/neptunius/docs/fluent/html/ug/node775.htm. [Accessed: 01-Dec-2019].

[110] S. Prakash and C. R. Ethier, “Requirements for mesh resolution in 3D computational hemodynamics,” *J. Biomech. Eng.*, vol. 123, no. 2, pp. 134–144, 2001, doi: 10.1115/1.1351807.

[111] F. Giraldo, “Time Integrators,” *Lecture notes*. [Online]. Available: http://faculty.nps.edu/fxgirald/projects/nseam/nps/new_section4.pdf. [Accessed: 06-Feb-2020].

[112] M. Fortin, H. Manouzi, and A. Soulaimani, “On finite element approximation and stabilization methods for compressible viscous flow,” *Int. J. Numer. Methods Fluids*, vol. 17, pp. 477–499, 1993, doi: 10.1002/fld.1650170604.

6 Appendix

```
#include "udf.h"
#include "prf.h"

#define bulge_th 9

DEFINE_PROFILE(physio_velocity_profile, t, pvp)
{
  face_t f;
     real height=0.01;
     real x[ND_ND];
     real y, s_max, v_mean_at_t;
  real period = 0.9;
     real actual_time= CURRENT_TIME;
  real beat_number = actual_time/period;
     real time = beat_number-floor(beat_number);
  v_mean_at_t         =         (8.09423*sin(12.90847*time-2.99266)+
7.1611*sin(time*13.75438-0.32451)-6.73674*sin(time*28.53115-
8.16715)-6.50845*sin(time*28.92759-5.26343)-4.56441*time+3.89766)*(-
0.05959*sin(9.1563*time-3.92483)-0.09942*time + 0.03503);

     s_max=1.5*v_mean_at_t;

     begin_f_loop(f,t)
     F_CENTROID(x, f, t);
     y = x[1]/height;
     F_PROFILE(f, t, pvp) = -s_max*(y*y-1.0);
   end_f_loop(f,t)

 }

DEFINE_EXECUTE_AT_END(March_clotable_region)
{
     Domain *domain = Get_Domain(1);
     face_t f;
     Thread *t0, *t1, *tf;
     cell_t c0, c1;
  real lysis = 250.0;
  real u0, u1, dvdx0, dvdx1, dudy0, dudy1, shear0, shear1;
  real visc = 0.0035;
     thread_loop_f(tf, domain)
     {
    begin_f_loop(f, tf)
    {
    if (!BOUNDARY_FACE_THREAD_P(tf))
             {
                        c1=F_C1(f,tf);
                        c0=F_C0(f,tf);
                    t1 = THREAD_T1(tf);
                    t0 = THREAD_T0(tf);
          u1=C_UDMI(c1,t1,0);
          u0=C_UDMI(c0,t0,0);
          if (u1 >0.9 || u0 >0.9)
          {

            dudy0=C_DUDY(c0,t0);
```

```
                      dvdx0=C_DVDX(c0,t0);
            shear0 = visc*(dudy0*dudy0+dvdx0*dvdx0);

            dudy1=C_DUDY(c1,t1);
                      dvdx1=C_DVDX(c1,t1);
            shear1 = visc*(dudy1*dudy1+dvdx1*dvdx1);

            if (shear0 > lysis || shear1 > lysis)
            {
              C_UDMI(c0,t0,0)=0.0;
              C_UDMI(c1,t1,0) = 0.0;
            }
            else
            {
              if (u1 > 1.9 && u0 < 0.1)
                  {C_UDMI(c0,t0,0)=1.0;}
              if (u0 > 1.9 && u1 < 0.1)
                  {C_UDMI(c1,t1,0)=1.0;}
            }
          }
        }
      }
                end_f_loop(f,tf)
   }
}

 DEFINE_EXECUTE_AT_END(Adjust_UDM0_by_fibrin_and_shear)
{
     Domain *domain = Get_Domain(1);
     Thread *t;
     cell_t c;
     real fibrin, clot_val;
     thread_loop_c(t,domain)
      {
           begin_c_loop(c,t)
                fibrin = C_UDSI(c,t,2);
      clot_val = C_UDMI(c,t,0);
                if (clot_val==1.0 && fibrin > 600.0)
                      {C_UDMI(c,t,0)=2.0;}

                if(clot_val==2.0 && fibrin > 5000.0)
                      {C_UDMI(c,t,0)=3.0;}

           end_c_loop(c,t)
      }
}


DEFINE_INIT(Set_UDM,domain)
{
      Thread *t, *tf;
   face_t f;
      cell_t c;
      int thnum, ni;
 thread_loop_c(t,domain)
 {
     begin_c_loop(c,t)
    C_UDMI(c,t,0)=0.0;
```

```
    C_UDMI(c,t,1)=0.0;
           c_face_loop(c,t,ni)
           {
                f = C_FACE(c,t,ni);
                tf = C_FACE_THREAD(c,t,ni);
                thnum = THREAD_ID(tf);
                if(thnum==bulge_th)
                {
                     C_UDMI(c,t,0)=1.0;
                }
           }
    C_UDSI(c,t,0)=0.0;
           C_UDSI(c,t,1)=7000.0;
           C_UDSI(c,t,2)=0.0;
     end_c_loop(c,t)
 }
}

DEFINE_PROFILE(vis_res,t,vr)
{
   real honey, clot_val;
   cell_t c;

   begin_c_loop(c,t)
   {
   clot_val=C_UDMI(c,t,0);
       if (clot_val> 2.9)
           honey=5.0e11;
   else if (clot_val> 1.9)
     honey = 5.0e9;
   else
     honey = 1.0;

       C_PROFILE(c,t,vr) = honey  ;
   }
   end_c_loop(c,t)
}

DEFINE_PROFILE(porosity_profile, t, pp)
{
      real porosity;
      cell_t c;

      begin_c_loop(c,t)
           if(C_UDMI(c,t,0)>2.9)
                porosity=0.35;
           else if (C_UDMI(c,t,0)>1.9)
                porosity=0.7;
           else
                {porosity = 1.0;}
           C_PROFILE(c,t,pp) = porosity;
  end_c_loop(c,t)
}

DEFINE_SOURCE (Source_of_UDS2,c,t,dS,eqn)
{
real source2 = 0.0;
real Thr, Fbng;
```

```
Thr=C_UDSI(c,t,0);
if(Thr>1.0)
  {
  Fbng=C_UDSI(c,t,1);
  if (Fbng>0.0)
        {source2=C_R(c,t)*59.0*Thr*Fbng/(3160.0+Fbng);}
  }
return source2;
 }

DEFINE_SOURCE (Sink_of_UDS1,c,t,dS,eqn)
{
real source1 = 0.0;
real Thr, Fbng;

Thr=C_UDSI(c,t,0);
if(Thr>1.0)
  {
  Fbng=C_UDSI(c,t,1);
  if (Fbng>0.0)
        {source1=-C_R(c,t)*59.0*Thr*Fbng/(3160.0+Fbng);}
  }
return source1;
 }


DEFINE_DELTAT(mydeltat,d)
{
   real time_step;
  real period1 = 0.9;
     real time= CURRENT_TIME;
  real beat_number = time/period1;
     real pstime = beat_number-floor(beat_number);

   if (pstime < 0.09)
      time_step = 0.005;
   else if (pstime < 0.41)
     time_step = 0.003;
   else if (pstime <0.67)
     time_step = 0.008;
   else
     time_step = 0.015;

   return time_step;
}

DEFINE_EXECUTE_AT_END(TG_curve)
{
     Domain *domain = Get_Domain(1);
      Thread *t, *tf;
      cell_t c;
      int thnum, ni;
   real PEAK = 264.0;
   real TTP = 3.0;
   real ETP = 1169.0;
   real e = 2.718282;
   real time2 = CURRENT_TIME/60.0;
```

```
   real  TH  =  PEAK*e*exp(-e*(time2  -  TTP)*(PEAK/ETP))*exp(-exp(-
e*(time2 - TTP)*(PEAK/ETP)));

thread_loop_c(t,domain)
{
     begin_c_loop(c,t)
          c_face_loop(c,t,ni)
          {
               tf = C_FACE_THREAD(c,t,ni);
               thnum = THREAD_ID(tf);
               if(thnum==bulge_th)
               {
                    C_UDSI(c,t,0)=TH;
               }
          }
     end_c_loop(c,t)
}
}
```